University of Bologna “Alma Mater Studiorum”, Naples
“Federico II” and “Roma III”, in convention with the National
Institute of Geophysics and Volcanology

Ph.D. Thesis in Geophysics

XXIII Cycle

GEO/10 - Year 2010-2011

Kinematic description of the rupture from strong motion data: strategies for a robust inversion

Ph. D. Thesis of: *Ernestina Lucca*

Coordinator

Prof. Michele Dragoni

Tutor

Dr. Gaetano Festa

Supervisor

Dr. Antonio Emolo

Page intentionally blank.

Ringraziamenti

Ci siamo … si sta chiudendo un altro importante capitolo della mia vita…. dopo la Laurea, anche il Dottorato…

Ho voluto con tutta me stessa raggiungere quest'obiettivo… all'inizio (come sempre!!!) ho avuto dubbi, perplessità (sono abbastanza brava? Non è meglio un'azienda?)…ma poi ho capito che dovevo a me stessa questi tre anni di dottorato…come dico sempre "mi sono regalata tre anni di vita", e con essi anche tante borse, vestiti, viaggi…. ☺ (ho praticamente esaurito i soldi dell'intera borsa di studio!!).

Dedico, quindi, a ME stessa questa tesi!! A me che ho speso ore e ore avanti al mio portatile (per gli amici: Pupetta!!) a scrivere e validare codici; a me che mi sono divertita ancora una volta a "giocare" con la matematica e con il Fortran, a me che sono sempre rimasta me stessa nonostante abbiano provato a farmi cambiare!! Dedico a me queste pagine e questi anni: Grazie Tina!

Questo lavoro non è tutto merito mio (non sono mica uno scienziato!!!). Ho avuto la fortuna di avere come tutor Gaetano Festa. Grazie Relatore! Grazie perché mi hai permesso di entrare nel dettaglio di ogni singolo problema non facendomi fermare alla superficie, grazie perché hai messo a mia disposizione il tuo cervello (che come tutti sanno è una fonte inesauribile di conoscenza), grazie perché mi hai lasciato lo spazio necessario per crescere nelle mie conoscenze mettendomi dei freni al momento giusto, grazie perché hai compreso che in alcuni momenti non avevo la testa per studiare, grazie perché hai creduto in me, grazie perché hai costruito questo dottorato praticamente su mia misura, grazie perché al momento giusto hai fatto le giuste cazziate…insomma Grazie di cuore dalla tua Studentessa!

Un grazie va ai miei compagni della stanza dei Dottorandi!! Mauela per la sua allegrie e la sua perenne disponibilità! Eugenio per farmi rivivere l'approccio alla sorgente sismica! A Simona, che oltre ad essere in gambe e dolcissima, ha corretto i mega errori grammaticali di inglese di questa tesi: Grazie Simo!!! Un bacio anche ad Antonella "O.": nell'interprestazione dei dati sei il top! Naturalmente un Grazie va a Mauro: mio amico-consigliere-consulente pc (Auguri per il tuo matrimonio!!). Grazie anche a Claudio per i passaggi in macchina e per la battuta sempre pronta!

Naturalmente un grazie doveroso va ai Prof!! Tutti tutti! Antonio Emolo (tranquillo Antonio, ho seguito ogni singolo tuo suggerimento per questa tesi!! E si si, sono una studentessa che studia!!Uff!!), Raffaella De Matteis (grazie per una chiacchierata che ci siamo fatte….sei una donna che stimo molto!), Aldo Zollo, Paolo Gasparini! Tra i prof (ma a dire il vero ormai è una mia cara amica) ringrazio anche la mia preferita: Grazie Giberti! I tre giorni trascorsi con me a Praga li porterò per sempre nel mio cuore….

Grazie di cuore anche a tutti i membri del RISSC-Lab!

Passo ora alla sfera personale! Un Grazie di cuore va alla mia Famiglia!! A Mamma Giovanna perché è la "mamma migliore del mondo" (sono una "bimba" stra-viziata!!), a mio Padre Vladimiro (il mio "papino") che ha sempre creduto in me e che mi vuole tanto bene (grazie per prestarmi sempre la stilo e per venirmi a prendere quando è necessario!!), a mia Sorella Tecla e suo marito Antonio: con voi a Roma c'è un pezzo del mio cuore (Sosy , lo sai, per te spaccherei una montagna…).

Colgo l'occasione per ricordare a due persone quanto sono speciali per me….quanto sono importanti..e che sono due punti di riferimento nella mia vita: Federica e Raffaele (Madrì e Padrì) Grazieeeeeee! Grazie alla mia cuginetta acquisita preferita Marylù: le nostre chiacchierate in macchina le adoro!! Grazie alla mia Dott.ssa Annamaria: quando finisco di parlare con te il mio animo è sempre sereno! Grazie per la frase che mi ripeti sempre : gli uomini sono perfettamente imperfetti!! Ed io sono l'essere più imperfetto che io conosca…ma mi adoro così come sono! Grazie al mio Vichingo preferito (Matteo!), ci siamo conosciuti tre anni fa ormai..non dimenticherò mai le nostre chiacchierate (mezze discussioni!) sull'approccio geologico e fisico allo studio delle Terra (io dicevo: "che me frega, la faglia è un rettangolo per me!!" e tu li a spiegarmi tutta la geologia e a convincermi che appezzottavo alla grande la realtà!!). Grazie alla mia compagna di viaggi: Cosmiana!! Grazie per avermi ospitato a casa tua, grazie per le ore ore passate a chattare!!!

Un grazie speciale va alla mia Puntarella (cos'è? La mia macchina!).

Grazie a te Peppe (o come dice mia Nonna Ernestina: "lo devi chiamare Giuseppe!!!"). Grazie per essere come sei, grazie per la tua montagna di difetti, grazie per la tua semplicità, dolcezza e comprensione. Grazie di avermi permesso di entrare nella tua vita e nel tuo cuore …. te ne sono infinitamente grata.

Grazie Amore mio!

Grazie a tutti i miei amici (passati e presenti!) e conoscenti che non cito perché altrimenti i ringraziamenti diventano più lunghi della tesi (e non mi sembra il caso!).

Un bacio grande va ai miei Nonni Luigi, Ernestina, Tecla…..vi voglio bene!

Infine, ricordo con immutato affetto mio Nonno Antonio e mio Zio Gianni….so che vegliate sempre su di me! Mio Nonno mi diceva sempre di non fare Fisica, ma di fare o l'Ing. o l'avvocato….diceva che facendo fisica ci si moriva di fame….bhè misà misà che aveva ragione...ma tornando indietro io mi iscriverei di nuovo a fisica e rifarei questo esatto dottorato…so che il futuro non è roseo…ma almeno fino ad oggi ho fatto quello che mi piaceva fare…e domani??? Chi vivrà vedrà!

Ed ora……. sfogliate la tesi e ditemi che è bella, interessante etc etc!!!!!!

Tina

"life is what happens to you while you are busy making other plans"

(John Lennon)

Page intentionally blank.

Contents

Contents 9
Introduction 12
Chapter 1 The seismic source: theoretical background 19
1.1. Introduction 19
1.2. Elastodynamics 20
1.3. The representation theorem 22
1.4. Green's function 25
1.5. Slip representation in frequency domain 27
1.6. Our formulation for the representation integral 31
Chapter 2 Numerical modeling of seismic wave propagation 32
2.1. Introduction 32
2.2. Seismic waveforms modeling 32
2.2.1. Mesh design 33
2.2.2. Numerical integration 37
2.3. Implementation of algorithm: STuDenT 41
2.4. Validation 46
2.4.1. Case: Strike-slip fault 48
2.4.2. Case: Dip-slip fault 58
2.4.3. Conclusion 70
Chapter 3 Slip parameterization 72
3.1. Introduction 72
3.2. Overlapping 2D Gaussian functions 73
3.2.1. The overlapping parameter 76

3.3. Relationship between the Gaussian width and the minimum resolvable wavelength 82
3.3.1. The projection of slip map onto Gaussian representation: the method 82
3.3.2. The projection of slip map onto Gaussian configuration: an example 85
Chapter 4 Inversion Strategy: two steps procedure 92
4.1. Introduction 92
4.2. The misfit function 93
4.3. The two-steps procedure 95
4.3.1. Non negative least square solution 97
4.3.2. The Neighbourhood algorithm 98
Chapter 5 Application of inverse technique to the Iwate-Miyagi-Nairiku earthquake 101
5.1. Case study 101
5.2. The synthetic test: Gaussian amplitude inversion 104
5.2.1. Case A: one circular anomaly 105
5.2.2. Case B: three circular anomaly 113
5.3. The synthetic test: two steps procedure. 120
5.4. The synthetic test: Conclusion 124
5.5. Real data inversion 124
5.5.1. Source and fault parameterization 125
5.5.2. The results of inversion: slip map and rupture time map 126
5.6. The results of inversion: synthetic and real data comparison 130
Chapter 6 Quality of solution: Analysis of Error and Resolution 134
6.1. Introduction 134

6.2. Data covariance matrix 134
6.2.1. Real data covariance matrix 136
6.2.2. Synthetic data covariance matrix 137
6.3. Errors analysis 138
6.3.1. Linear problem 138
6.3.2. Non linear problem 139
6.4. Results 140
Conclusion 143
Appendix A: Time-Frequency misfit criteria 147
Bibliography 150
Index 157
Index of figures 160
Index of the tables 168
Symbols 169

Introduction

The history of our seismological knowledge probably starts in 1760 when J. Michell (1724-1793) first associated earthquakes with waves that travel through the Earth's crust with a speed of at least 20 miles per minute (*Michell, 1760*). His observation that waves propagate through the Earth was explained after with the theory of elasticity, developed in the 18th and 19th centuries. A. L. Cauchy (1789-1857), S. D. Poisson (1781-1840), G. G. Stokes (1819-1903) and many others studied the elastic wave equation: P waves and S waves travelling with different velocities were identified as possible solutions. H. F. Reid (1859-1944) concluded, from his studies, that the earthquake source can be modelled by a shear rupture propagation on the earth crust and is an effect of a local and continuously tectonic deformation process. When the maximum tectonic stress is reached, the stored elastic energy is rapidly released causing a relative displacement of two adjacent volumes, and generating, in this way, a discontinuity surface between two blocs (fault plane). The rupture initiates quasi-statically on a small nucleation zone and then, when the friction at the rupture front drops from the static to the dynamic level, it develops into an unstable phase over the fault surface. In the framework of elastodynamics, the ground motion resulting from an earthquake source is expressed numerically using a representation theorem, which relates the observable motion with the dislocation occurring along the fault plane, through a surface integral involving both the dislocation and the wave propagation in the Earth. In a mathematical approach the fault is only a “plane”, but geologically it is a complex structure with a finite thickness and different types of rocks, so that geologists usually speak about “fault zone”. Generally, the frequencies of seismological interest in the strong motion data, correspond to wavelengths larger than the typical thickness of a fault (around 100 m). We can therefore consider the fault as a plane imbedded in a volume with constant elastic properties. Direct observations are very rare, since most of the ruptures take place at depth. For this reason, most of the available information about the seismic source rupture process come from the inversion of ground motion data.

Seismometry has seen huge advances in the past 30 years. The dynamic range of typical seismometers has increased from less than 5 orders of magnitude to more than 7. Moreover, the past 30 years have also seen the big development of digital data communication, processing and storage, which has promoted the installation of a large number of seismic networks, very close to the principal fault system, since the earthquake source, generally, is on pre-existing or newly created faults. A seismic network can be national or regional. The most important nationwide strong-motion network in Italy is the RAN (Rete Accelerometrica Nazionale) managed by Civil Protection, while in Japan we can find the K- and Kik- networks (*Kinoshita, 1998*; *Aoi et al., 2004*). As an example of regional network, we recall the Southern Italy network ISNet (Irpinia Seismic Network) equipped with accelerometers and short-period/broadband seismic sensors, operating around the fault that generated the 1980 earthquake. A dense distribution of data around the source is necessary to have a considerable number of constraints for the inverse solution (*Olson et al., 1988*).

Dynamic modeling of earthquake source provides a description of the slip (dislocation on fault plane) evolution related to constitutive properties and requires the definition of the initial values and boundary conditions for the stress necessary for the nucleation and the propagation of the earthquake rupture. In contrast, kinematic models of seismic source (e.g. *Haskell, 1969*) describe the resulting motion (slip history) without investigating the causes of the rupture process. This means that if the displacement discontinuity across a fault is known as a time-dependent function of position on the fault, then motions that radiate from the source region, are completely determined (*Aki and Richards, 1980*).

Kinematic rupture models are used to invert ground motion waveforms, recorded at the seismic network, which provide a detailed image of the slip history during the rupture process. Historically, the first work that used the representation theorem for the inversion of the slip on fault was made by Trifunac (1974), who applied his method to five strong motion records of the 1971 San Fernando, California, earthquake. The author used a full-space geometry and a simple trial and error approach to fit data. Efforts to reveal the details of rupture processes started in the early 1980s. Olson and Apsel (1982) provided the first study in which the problem of the slip inversion was considered on a formal basis of the linear inversion theory. Then, Hartzell and Heaton (1983) parameterized the Imperial fault, California, by small subfaults to infer the kinematic history of a magnitude 6 event, in 1979. Their approach or variants of it were used in many subsequent studies (*Fukuyama and Irikura, 1986*; *Takeo, 1987*; *Beroza and Spudich, 1988*; *Yoshida and Koketsu, 1990*; *Wald and Heaton, 1994*; *Cotton and Campillo, 1995*; *Yagi and Kikuchi, 2000*; *Bouchon et al., 2000*; and many others).

The rupture history is the solution of an inverse geophysical problem, which is inherently non unique. This means that many models may explain the data equally well (*Monelli and Mai, 2008*) also if input seismograms are noise-free synthetics (Blind Test; Mai et al. 2005, website: http://www.spice-rtn.org/members/mai/BlindTest/index.html). Another cause of complexity is that the real data include noise which affects the information contained on the model.

Earthquake kinematic models are used as input data to seismological applications aimed at understanding the dynamic properties of the seismic source and they are used to estimate the seismically radiated energy and to predict the ground motion shaking scenarios for engineering design purposes. Consequently, a robust kinematic inversion is important for the reliability of such studies. The non-uniqueness of kinematic source inversion seems to be the principal limiting factor and many authors have addressed this topic and formulated some partial answers.

The present work aims at contributing to this discussion, with the main. Our objective is to investigate the robustness of the solutions, by studying in detail a particular slip parameterization. We parameterized the slip distribution with 2D overlapping Gaussian functions and we given the quantitative rules to correlate the characteristic of the new parameterization to the data frequency.

In this thesis, we formulated a non linear technique to invert strong motion records, with the aim of obtaining the final slip and the rupture velocity distributions on the fault plane. We used a two-step procedure in order to separate the computation of the rupture velocity (non-linear problem) from the evaluation of the slip distribution (linear problem). Moreover, we discussed the of uncertainties on estimated parameters.

In the first chapter we will give a brief review of the seismic source theory, starting from the elastodynamics and arriving to the representation integral. Here, the forward problem, i.e. the ground motion simulation, is solved evaluating the representation integral in the frequency domain, as proposed by Burridge and Knopoff in 1964.

In second chapter we will focus our attention to the numerical computation of the representation integral. The representation integral was computed through a finite elements technique based on a Delaunay triangulation of the fault plane. The Green's tractions on the fault are computed using the discrete wave-number integration technique (*Bouchon, 1981; Coutant, 1989*), that provides the full wave-field for a 1D layered propagation medium. The rupture velocity is defined on a coarser regular grid and rupture times are computed by integration of the eikonal equation. This methodology was implemented in a Fortran90 code, called "STuDenT" (*Simulation daTa with Delaunay Triangulation*).

In the third chapter we will show a new parameterization for the slip based on 2D overlapping Gaussian functions defined on regular grid on the fault. The Gaussian functions are characterized by an amplitude and a width. The width is related to the minimum resolvable wavelength on the fault plane and, through is, to the maximum analyzed frequency in the data.

In the fourth chapter we will present the inverse technique. The inverse problem is solved by a two-steps procedure aimed at separating the computation of the rupture velocity from the evaluation of the slip distribution, the latter being a linear problem, when the rupture velocity is fixed. The non-linear step is solved by optimizing the L_2 misfit function between synthetic and real seismograms, and the solution is searched using the Neighbourhood Algorithm. The non-negative least square solution, instead, is used to solve the linear step.

In the fifth chapter we will apply the methodology to the Mw 6.9, Iwate Nairiku Miyagi, Japan, earthquake that was recorded by the K-net and Kik-net accelerometric networks. From the inversion of strong motion data, we obtained the inverted slip map and the rupture times. The estimated magnitude seismic moment is 2.63^{26} dyne·cm that corresponds to a moment magnitude M_W 6.9 while the mean the rupture velocity is 2.0 km/s. A large slip patch (maximum slip of 6.35 m) extends from the hypocenter to the southern shallow part of the fault plane. A second relatively large slip patch (maximum slip of 1.51 m) is found in the northern shallow part.

Finally in the sixth chapter we will afford the problem of uncertainties on the estimated parameters. The uncertainties on the parameters can be described by a multidimensional Gaussian probability density. In our methodology we splitted the problem in a linear and a non linear part; so we can use the classic theory for the linear problems while we correlate the variance of the non-linear solution with the curvature of the misfit function at its minimum.

Chapter 1
The seismic source: theoretical background

1.1. Introduction

The study of seismic source is of great importance in seismology, allowing us to understand the dynamics of earthquakes. The parameters that characterize the seismic source are based on the ground motion recorded by the seismic stations, using the tools of inverse theory. The kernel of inverse theory is the computation of the displacement on the Earth's surface due to an earthquake, called the direct problem. In such a problem, the displacement is calculated by solving of the representation integral, the governing equation that relates ground motion displacement at the station to the motion on an extended fault.

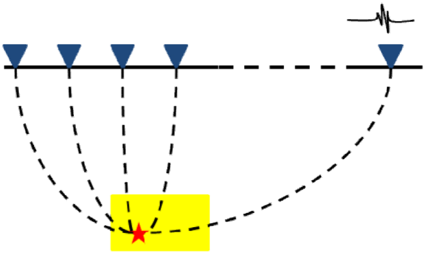

Figure 1-1: Scheme of the seismic wave propagation and record at the seismometers. The triangles represent seismic stations, which record the ground motion generated by an extended fault (yellow rectangle).

1.2. Elastodynamics

The description of fault mechanics is based on the solution of the fundamental elastodynamic equation, derived from the classical Newtonian representation. This fundamental equation relates the forces in the medium to the measurable displacement. It is inferred from the second law of dynamics for continuous media:

$$\rho \ddot{u}_i = f_i + \sigma_{ij,j} \qquad (1.1)$$

where (1.1) ρ is the density of the solid body, $\ddot{u}_i$ is the time second derivative of the displacement, that is related to the deformation of the body, f_i is the i-th component of the applied external body force density acting per volume unit, and finally σ_{ij} the the ij-component of the stress tensor. By definition, a material is elastic if it returns to its original condition after removing the applied load. Experimentally Hooke observed that the extension of a spring increases linearly with the applied load. This is the simplest representation of an elastic constitutive law, which for a continuous system corresponds to a linear relation between stress and strain:

$$\sigma_{ij} = c_{ijkl}\varepsilon_{kl} \qquad (1.2)$$

ε_{ij} being the component of the strain tensor. The strain tensor is the measure of the length deformation for the infinitesimal deformations. The diagonal components of the tensor are the deformations along the axes of reference frame (normal strain), while the off diagonal components are related to the angles that the normals to the faces of the deformed volume element form with the original ones (shear strain). The strain tensor is symmetric by definition. The fourth-order tensor **c** is called the "elastic coefficient tensor", since it is independent on the strain. **c** is symmetric by all indices exchange, as it can be shown by invoking the symmetry of the stress and strain tensors, so only 21 of its 81 components are really independent. For an isotropic medium, i.e., if the elastic properties are independent of the orientation, the number of independent components is reduced to 2 (*Jeffreys and Jeffreys, 1972*)

$$c_{ij\,kl} = \lambda\delta_{ij}\delta_{kl} + \mu\left(\delta_{ik}\delta_{jl} + \delta_{il}\delta_{jk}\right) \tag{1.3}$$

In equation (1.3) λ and μ are the Lamé constants and δ_{ij} is the dimensionless Kronecker delta function[1].

Using the expression (1.3) and (1.2), we obtained:

$$\sigma_{ij} = \lambda e_{kk}\delta_{ij} + 2\mu e_{ij} \tag{1.4}$$

---

[1] **Kronecker delta function**: It is a function of two indices. It is 1 if the indices are equal and 0 otherwise: $\delta_{ij} = \begin{cases} 1 & if\, i = j \\ 0 & f\, i \neq j \end{cases}$

It is the stress-strain relation for isotropic media.

1.3. The representation theorem

The representation theorem is a formula for the ground displacement, at general point in space and time, in terms of the quantities that originated the motion: these are body forces and/or applied tractions over surface of the elastic body. Betti's reciprocity theorem relates a pair of forces applied in a certain volume with their corresponding displacements. This theorem is then used in order to have the displacement at the Earth's surface caused by an earthquake. The starting point of Betti's theorem is to assume two body forces in an elastic medium of volume V with the corresponding displacements (solution of equations 1.1 and 1.2). Replacing one of the forces by a unit impulse force in space and time, which is represented mathematically by a Dirac delta function, its corresponding displacement is then called a Green's function and it represents the effect of the propagation of elastic waves in the medium. Thus, after some mathematical manipulation it is possible to write the follow expression for an elastic displacement in a volume V produced by a system of body forces, in the following form:

$$
\begin{aligned}
u_n = &\int_{-\infty}^{+\infty} dt \iiint_V f_i(\mathbf{x},t) G_{in}(\mathbf{x},\tau - t;\vec{\xi},0) dV \\
&+ \int_{-\infty}^{+\infty} dt \iint_S \{ \ G_{in}(\mathbf{x},\tau - t;\vec{\xi},0) T_i(u(\mathbf{x},t),\mathbf{n}) \\
&- u_i(\mathbf{x},t) c_{ijkl} n_j G_{kn.l}(\mathbf{x},\tau - t;\vec{\xi},0) \ \} dS
\end{aligned}
\qquad (1.5)
$$

where f_i is the body force, u_i is the displacement in the volume V, T_i is the i-th component of the traction[2], c_{ijkl} is a tensor of a constant elastic, G_{in} are the Green's functions, t is the time. The vector n_j is the normal vector to the surface S, $\vec{\xi}$ is a local coordinate system on a fault and **x** is the receiver position.

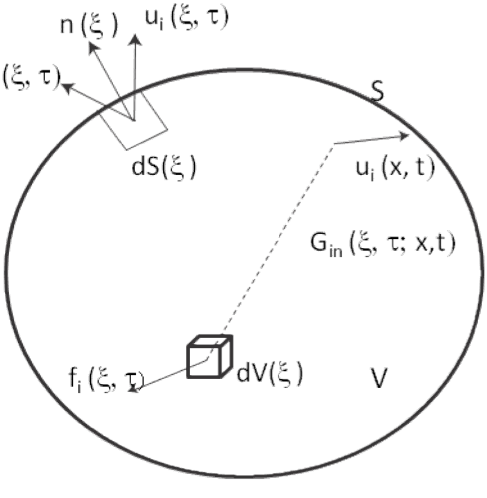

Figure 1-2: Sketch of the elastic displacement corresponding to a body force f, and traction T in a medium with Green's function G.

---

[2] **Traction**: Traction is a vector, being the force acting per unit area across an internal surface within continuum, and quantifies the contact force (per unit area) with which particles on one side of the surface act upon particles on the another surface (*Aki and Richards, 2002*).

Let us now consider zero body forces in the interest region. The integral over V is equal to zero, reducing equation (1.5) to:

$$\begin{aligned} u_n = \int_{-\infty}^{+\infty} dt \iint_S \{ \; & G_{in}\left(\mathbf{x},\tau - t;\vec{\xi},0\right) T_i\left(u(\mathbf{x},t),\mathbf{n}\right) \\ & - u_i(\mathbf{x},t) c_{ijkl} n_j G_{kn.l}\left(\mathbf{x},\tau - t;\vec{\xi},0\right) \; \} dS \end{aligned} \quad (1.6)$$

During an earthquake there is a rupture on the fault plane, so the focal region, delimited by a surface Σ (fault), can be represented by a fracture or a dislocation in an elastic medium. This dislocation is usually defined by the slip vector Δu that is the difference of the displacement between the two sides of a fault: Σ+ and Σ-.

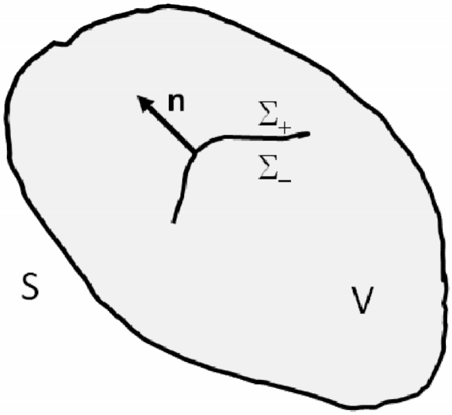

Figure 1-3: An elastic body with volume V and external surface S. The fault plane has two side, labeled with Σ+ and Σ-, and **n** is the normal to the fault from Σ+ to Σ-.

The boundary conditions across the fault are the continuity of the stress (their integral is null) and the discontinuity of the displacement. Moreover, the Green's functions are continuous through the surface Σ. Plugging these conditions into equation (1.6) yields at an equation for a kinematic model of the source:

$$u_n = \int_{-\infty}^{+\infty} d\tau \iint_{\Sigma} \left\{ \Delta u_i \left(\vec{\xi}, \tau\right) c_{ijkl} n_j G_{kn.l} \left(\mathbf{x}, \tau - t; \vec{\xi}, 0\right) \right\} dS \qquad (1.7)$$

The most widely used models to represent the seismic source are those in which the earthquake results from of a displacement discontinuity along a fault plane. This representation defines a kinematic source model, in which the dislocations on the Earth surface are derived from a given/known/assumed slip vector that represents the inelastic displacement discontinuity with respect to the two sides of a fault.

The kinematic approach is very useful to estimate the "source parameters" and to interpret the observations. The parameters generally used to describe the seismic source are: the seismic moment, the fault dimension and orientation, the slip, the rise time[3] and the rupture velocity distribution on the fault plane.

1.4. Green's function

The computation and the knowledge of the Green's functions is not an easy problem since these are dependent on

---

[3] **Rise time**: the rise time characterizes the time needed for the slip vector, at a particular point on the fault, to reach its final value.

the specific proprieties of propagation medium. A simple approach is to consider an isotropic, homogeneous, infinite and elastic medium. Under this condition it is possible to have an analytical expression for the Green's functions:

$$\begin{aligned} G_{ip}(\mathbf{x},t;\ \xi,\tau) = & \frac{1}{4\pi\rho}\left(3\gamma_i\gamma_p - \delta_{ip}\right)\frac{1}{r^3}\int_{r/\alpha}^{r/\beta} t'\delta\left(t-\tau-t'\right)dt' + \\ & + \frac{1}{4\pi\rho\alpha^2}\gamma_i\gamma_p\frac{1}{r}\delta\left(t-\tau-\frac{r}{\alpha}\right) \\ & - \frac{1}{4\pi\rho\beta^2}\left(\gamma_i\gamma_p - \delta_{ip}\right)\frac{1}{r}\delta\left(t-\tau-\frac{r}{\beta}\right) \end{aligned} \qquad (1.8)$$

where γ is the unit vector from the source point ξ to the receiver $\mathbf{x}$, and $r=|\mathbf{x}-\xi|$ is the distance between two points, ρ is the density and α and β are P and S wave velocities of respectively.

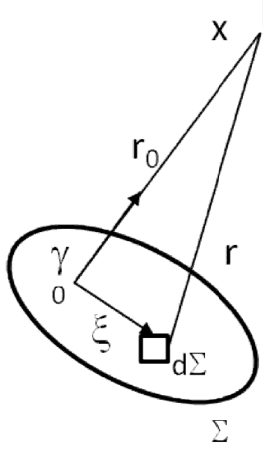

Figure 1-4: System coordinate on fault surface.

Even in a homogeneous medium, the elastodynamic Green's functions include the P and S wave, and the near-field terms. These terms are well-defined in the equation (1.8) but in a more realistic model of the Earth it does not happen, and we also have to consider the terms of direct, reflected, refracted, and surface waves. The accuracy of the reconstructed Green's function depends on the amount of complexity of medium and data, and on the methodology to retrieve the information by data.

In this thesis we used a layered medium model and compute the synthetic Green's function with a wave propagation code, based on Bouchon's theory (1981). Generally, it is also possible use empirical Green's function (EGF) such as aftershock records (*Fukuyama and Irikura, 1986*) or very small records events around the interest area, but there are two important limitations: the small event must be near the mainshock and have a similar centroid depth and focal mechanism, and there is a uniform EGF coverage around the fault plane compared to the minimum wavelength resolvable in the data.

1.5. Slip representation in frequency domain

In this thesis, the ground motion associated with displacement on the fault plane was computed by considering the representation integral in the frequency domain, according to the formulation of *Burridge and Knopoff* (1964):

$$u_n(\mathbf{x},\omega)=\iint_{\Sigma} \Delta u_i(\vec{\xi},\omega)T_{ni}(\mathbf{x},\vec{\xi},\omega)d\vec{\xi} \qquad (1.9)$$

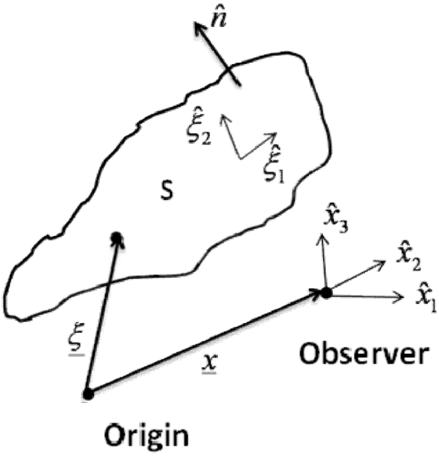

Figure 1-5: Model geometry and parameters.

where u_n is the Fourier transform[4] of the n-th component of the displacement at the position **x** and for the angular frequency ω. The displacement is given by the integral on the fault surface Σ of the product between the Fourier transform of the displacement discontinuity Δu across Σ and the Fourier transform of the Green's tractions T_{ni}. The Green's traction includes the Green's function and the tensor of constant elastic. Finally, $\vec{\xi}$ is the local coordinate system on the fault plane (figure 1-5).

In the time domain we assume that the displacement discontinuity across the fault can be factorized in the product of

---

[4] **Fourier transform:** When we define the Fourier transform of a time dependent function, we assume the sign convention for the exponent as following $f(t) \rightarrow f(\omega) = \int_{-\infty}^{+\infty} f(t)\exp(+i\omega t)\,dt$

according with *Aki and Richards* (2002).

the final slip amplitude A by the slip-velocity source-time function S:

$$\Delta u_i\left(\vec{\xi},t\right)= A\left(\vec{\xi}\right)S\left(\vec{\xi},\, t-R\left(\vec{\xi}\right)\right) \qquad (1.10)$$

in all point of the fault surface.

If we transform the equation 1.10 from the time-domain to the frequency-domain, we get:

$$\Delta u_i\left(\vec{\xi},\omega\right)= A\left(\vec{\xi}\right)\hat{S}\left(\omega,\tau\right)e^{-i\omega R_T\left(\vec{\xi}\right)} \qquad (1.11)$$

The earthquake starts at a point (the hypocenter) and a dislocation front expands outward over the fault. The function $R_T(\vec{\xi})$ is the map of rupture times, i.e, the times at which the dislocation reaches in $\vec{\xi}$ point. Generally, the rupture front velocity ($v_r\vec{\xi}$) is heterogeneous and depends on the proprieties of the propagation medium. From the inversion of seismic data and laboratory experiments, the rupture velocity, generally, is less than the S-velocity and results $v_r \approx (0.7 \div 0.9)\,\beta$ (*Rosakis, 2002*).

The S-function is the slip-velocity source-time function (svSTF), and prescribes the slip velocity evolution during the rupture propagation.

Several authors have proposed different functional forms for the STF (*Kukuyama and Irikura, 1986*; *Fukuyama and Mikumo, 1983*; *Cotton and Campillo, 1995*) and have pointed out the importance of the STF in kinematic source models for strong motion prediction (*Hisada, 2000, 2001; Guatteri et al. 2003*).

In this thesis we worked with two simplest svSTF functions: a rectangle and a triangle. We give the analytical expressions for these sv-STF in the frequency domain:

- Rectangle function: svSTFb

$$\hat{S}(\omega,\tau)=\frac{\sin\left(\omega \tau_r/2\right)}{\omega \tau_r/2}e^{-i\omega\left(\tau_r/2\right)} \qquad (1.12)$$

- Triangle function: svSTFt

$$\hat{S}(\omega,\tau)=\frac{\sin\left(\omega^2 \tau^2_r/4\right)}{\omega^2 \tau^2_r/4}e^{-i\omega\left(\tau_r/4\right)} \qquad (1.13)$$

The two svSTFs are sinc functions[5] with a phase shift that depends on the rise time. Generally, we are interested into the kinematic inversion that works with low frequency data and in this part of the spectra the shape is the same for two cases: a plateau at low frequencies and a decay for frequency larger than cut-off frequency.

---

[5] **Sinc function**: It is defined as: $\frac{\sin(x)}{x}$.
It is a sine wave that decays in amplitude as $1/x$.

1.6. Our formulation for the representation integral

Using the equation (1.11) and a svSTFb (eq. 1.12), the representation integral (eq. 1.9) can be rewritten as:

$$u_n(\mathbf{x},\omega)=\iint_{\Sigma} A(\vec{\xi})\frac{\sin\left(\omega^{\tau_r}\!/_{2}\right)}{\omega^{\tau_r}\!/_{2}}e^{-i\omega\left({}^{\tau_r}\!/_{2}+R_T(\vec{\xi})\right)}\,T_{ni}(\mathbf{x},\vec{\xi};\omega)d\vec{\xi} \qquad (1.14)$$

In this thesis, we will use the previous formula to calculate the synthetic seismograms used as the inversion kernel to retrieve the source characteristics.

Chapter 2
Numerical modeling of seismic wave propagation

2.1. Introduction

One of the main objective of this thesis is the development and validation of numerical code STuDenT (*Simulation of daTa with a Delaunay Triangulation*) for computing the representation integral in the Burridge and Knopoff formulation (equation 1.14), as presented in section 1.6. STuDenT is a numerical code for the simulation of synthetic seismograms, based on the discretization of the fault by a finite element approximation; in particular we have adopted a decomposition of the fault plane into triangular subfaults.

2.2. Seismic waveforms modeling

The essence of finite element method, as implemented in STuDenT, can be synthesized in two steps:

a) *Mesh design*: the computational domain is decomposed into a mesh of elements;

b) *Numerical integration*: definition of a rule to compute the representation integral.

2.2.1. Mesh design

The representation integral is computed numerically by discretizing the fault Σ in N subfaults (Ω_i) having the shape of non-overlapping triangles $\Sigma = \bigcup_{j=1}^{N} \Omega_j$.

Generally, the subfaults have the shape of square, and the size (dξ, along one direction) of a single subfault depends on the ratio between the local wave speed (generally the S-wave velocity) and the maximum frequency we want to be represented in the simulated records:

$$d\xi \approx \frac{\beta_{\min}}{f_{\max}} \tag{2.1}$$

If we use a uniform spacing, the size of the integration grid is then associated with the smallest value of S-wave. In general, the smallest values of the propagation velocity are in the shallow part of the medium; consequently this space scale does not need to be resolved for the deeper, faster regions of the fault plane, where the grid size could be larger (the ratio between the coarse and fine grid sizes can be as large as a factor two). The grid size may vary as a function of frequency and depth, so that fewer sample points are used at depth, because here the traction function is varying more slowly as a function of position on the fault (*Spudich and Archuleta*, *1987*). Since the shear wavelength is inversely proportional to the frequency and proportional to the local shear velocity, the sample spacing can become denser with increasing frequency and generally less dense with increasing depth. Hence, we are able to reduce the computational cost in the evaluation of the representation integral, by coarsening the computational grid as a function of the S-wave velocity. Such approach could bring to negligible improvements in computational time for a single forward modeling computation, because most of the time is spent in the evaluation of the Green tractions, but it really matters when the forward problem is used as a kernel of an inversion problem, where Green tractions are computed only once before running the inversion. As a consequence, we allow the integration grid size to depend on the local S wave speed and we manage the coarsening of the computational grid using a finite element integration on a Delaunay triangulation (figure 2-1).

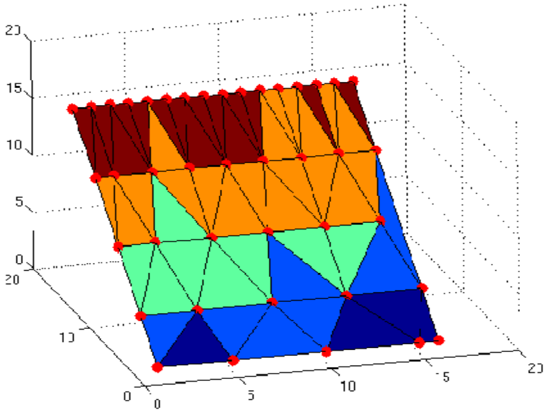

Figure 2-1: Delaunay triangulation of the hypothetical fault plane.

This triangulation was introduced by Boris Delaunay in 1934. In mathematics and computational geometry, a Delaunay triangulation DT(**P**) for a set **P** of points in the plane verifies the condition that no point in **P** is inside the circumcircle of any triangle in DT(**P**). Delaunay triangulations minimizes the maximum angle of all possible triangulations and tend to avoid skinny triangles. As compared to quadrangular finite element solutions, which have also been applied for the evaluation of the representation integral (*Liu and Archuleta, 2004)*, a triangular mesh automatically fits a set of space points well adapting to the coarsening of a numerical grid. On the other side, conforming quadrangulation requires the use of either ad-hoc manual procedures or addition of grid points during the coarsening of the grid (partition of triangles in four quadrangles of smaller size).

Our numerical method describes a phenomena evolving with time, and it can propagate a real signal between each pair of nearby grid points, if the propagation time is greater than the time step Δt. This condition, assuming the causality if the method, can be quantitatively defined through the Courant number:

$$c_0 = \frac{\alpha_{\max} \Delta \mathrm{t}}{\mathrm{d}\xi_{\min}} \qquad (2.2)$$

which is required to be smaller than one. In the expression, $\alpha_{\max}$ is the maximum P wave velocity value in the medium, and $\mathrm{d}\xi_{\min}$ is the minimum distance between the nearest nodes of the mesh.

Numerically it was proved that values of $c_0 \leq 0.5$ warrant a dispersion error lower 5 % (*Komatitsch et al., 1998*).

Another parameter important is the minimum wavelength λ_{min} resolvable on the fault plane. It is related to $\Delta\xi_{min}$ and f_{max}, the "resolving frequency" of the finite element grid. It is the maximum frequency at which we want the calculation to be accurate and it is not the Nyquist frequency f_N. It is related with Δt by:

$$f_N = \frac{1}{2\Delta t} \qquad (2.3)$$

The relationship between these parameters is:

$$\lambda_{\min} = \frac{\beta}{f_{\max}} \qquad (2.4)$$

Usually a minimum of 5 to 10 points per wavelength is necessary to limit the numerical dispersion:

$$\frac{\lambda_{\min}}{5 \div 10} \qquad (2.5)$$

Furthermore, the directivity effect[6] influences the frequency content in the signal (Doppler effect[7]). In particularly, it

---

[6] **Directivity effect:** It is related to the mutual position of fault-.reciver. If a seismic station is located along the direction of rupture propagation (directivity direction), the signal has higher frequency content and larger amplitude, while if the station is located such that the fault is rupturing away from it (anti-directivity direction), the signal has lower amplitude and smaller frequency.

[7] **Doppler effect**: It is the effect of the change in frequency of a wave for an observer moving relatively to the source of the wave. The frequency is higher (as compared to the emitted frequency) when the observer is approaching the

influences the minimum wavelength λ_{min} resolvable on the fault plane. We formalized this influence whit a new parameter α^D :

$$\lambda_{min}' = \lambda_{min}\alpha^D \tag{2.6}$$

where

$$\alpha^D = 1 - \frac{v_r \cos\vartheta}{\beta} \tag{2.7}$$

where ϑ is the angle from the fault and station (*Lay and Wallace, 1995*). If $\vartheta=0$ the station is in directivity position, while for $\vartheta=\pi$ the station is in anti-directivity position.

2.2.2. Numerical integration

Assume we defined a triangulation on the fault plane such as $\Sigma = \bigcup_{j=1}^{N} \Omega_j$. The representation integral can be decomposed onto the sum of the integrals referred to the single triangles Ω_j

$$u_n(\mathbf{x},\omega) = \sum_{j=1}^{N} \int_{\Omega_j} [u_i(\vec{\xi},\omega)] T_{ni}(\vec{\xi},\mathbf{x};\omega) d\vec{\xi} \tag{2.8}$$

---

source, it is identical at the instant of passing, and it is lower during the removal.

In which $\left[u_i\left(\vec{\xi},\omega\right)\right]$ is another equivalent notation of the $\Delta u_i\left(\vec{\xi},\omega\right)$ and **x** and $\vec{\xi}$ are the coordinates of receiver and source, respectively (figure 1-4).

We performed a linear mapping, transforming a physical triangle in a "reference" right-hand triangle having vertices in the points (0,0), (1,0) and (0,1). If $\vec{\eta}=(\eta_1,\eta_2)$ is the variable in the 2D reference domain Ω_{ref}, we can then define the shape functions

$$\begin{aligned} N_1(\vec{\eta}) &= 1-\eta_1-\eta_2 \\ N_2(\vec{\eta}) &= \eta_1 \\ N_3(\vec{\eta}) &= \eta_2 \end{aligned} \qquad (2.9)$$

which allow for linearly mapping the reference domain into the physical domain Ω:

$$\vec{\xi}_j(\vec{\eta}) = \sum_{a=1}^{3} N_a(\vec{\eta})\vec{\xi}_{aj} \qquad (2.10)$$

where $\vec{\xi}_{aj}$ represents the a-th vertices of the j-th triangle in the physical domain Ω (figure 2-2)

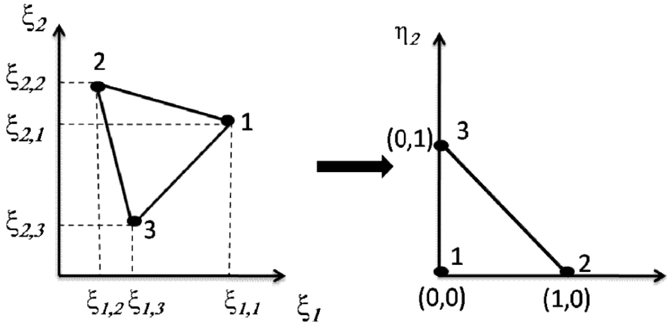

Figure 2-2: .Example of the transformation from the physical domain (left) to the referee (right) domain, in which all triangles are right.

We evaluated the j-th integral onto the "reference" triangle Δ, and we also assume that the restriction of the function is linear in each triangle, as standard for triangular finite element techniques. The representation of the function in the reference domain becomes

$$[u_i(\vec{\xi}(\vec{\eta}),\omega)]T_{in}(\vec{\xi}(\vec{\eta}),\mathbf{x};\omega)\,|_{\Omega_j}=\sum_{a=1}^{3}N_a(\vec{\eta})[u_i(\vec{\xi}_{aj}(\vec{\eta}),\omega)]T_{in}(\vec{\xi}_{aj}(\vec{\eta}),\mathbf{x};\omega) \tag{2.11}$$

Finally, the representation integral is solved in the reference domain as

$$u_n(\mathbf{x},\omega)=\sum_{j=1}^{N}\int_{\Delta}\sum_{a=1}^{3}N_a(\vec{\eta})[u_i(\vec{\xi}_{aj}(\vec{\eta}),\omega)]T_{in}(\vec{\xi}_{aj}(\vec{\eta}),\mathbf{x};\omega)J_j(\vec{\eta})d\vec{\eta} \tag{2.12}$$

where J_j is the jacobian of the mapping referred to the j-th triangle.

The Jacobian J of the mapping

$$J=\frac{\partial(\xi_1,\xi_2)}{\partial(\eta_1,\eta_2)} \tag{2.13}$$

is used to define the relationship between a small surface element $d\xi_1\, d\xi_2$ and a surface $d\eta_1\, d\eta_2$ in the reference triangle:

$$d\xi_1\, d\xi_2 = J\, d\eta_1\, d\eta_2 \qquad (2.14)$$

For linear shape functions the integral can be analytically solved

$$\int_{\Delta} \Phi(\vec{\eta}) J_j(\vec{\eta})\, d\vec{\eta} = \frac{\Phi_1 + \Phi_2 + \Phi_3}{3} \Lambda_j \qquad (2.15)$$

where Φ_1, Φ_2 and Φ_3 are the values of the function Φ at the vertices of the physical domain and Λ_j is the area of j-th triangle.

It is worth to note that such a finite-element solution collapses into the standard summation of subfault contributions if a regular grid is used for the discretization of the subfault. As for standard finite elements, instead of computing the representation integral inside the single triangles and then sum-up all the contributions, we can assemble the contribution of the areas of triangles sharing the same grid points. Then, the result can be achieved as the dot product of the field value at each point times the sum of the areas of the triangles having such a point as a vertex.

If we included the slip amplitude, the svSTFb, and the traction in the m-node (m=1,2,3), we obtained a analytical formula for the Φ_m-function:

$$\Phi_m = A_m \frac{\sin\left(\omega \, {}^{\tau_r}\!/_2\right)}{\omega \, {}^{\tau_r}\!/_2} e^{-i\omega\left({}^{\tau_r}\!/_2 + R_{Tm}\right)} T_m \qquad (2.16)$$

2.3. Implementation of algorithm: STuDenT

This technique was implemented in a Fortran90 code, STuDenT (*Simulation of daTa with Delaunay Triangulation* **).** The sequence of the different applications, is shown in the flowchart of figure 2-3.

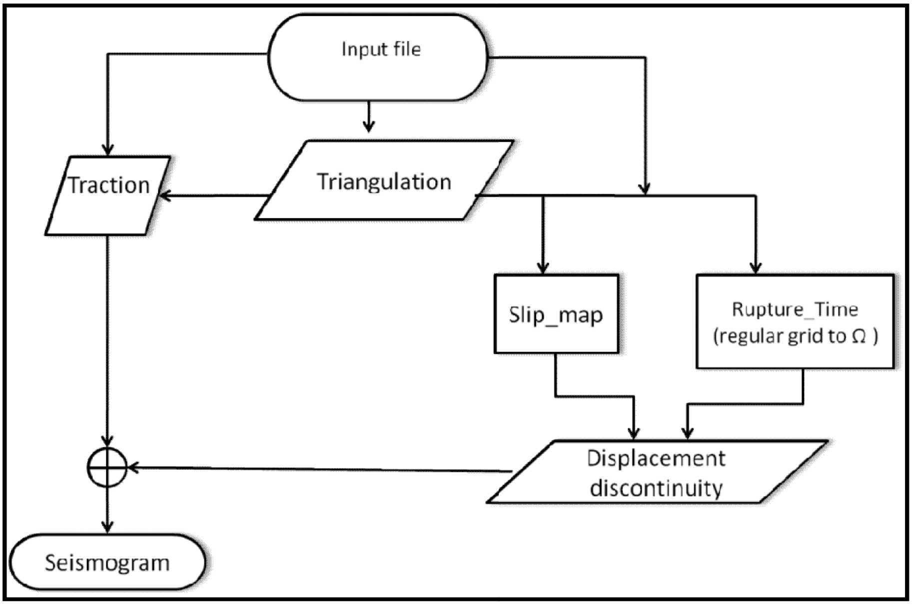

Figure 2-3: Flowchart of STuDenT code.

Let us introduce the standard terminology for describing fault orientation and slip directions (figure 2-4).The fault orientation in geographic coordinates is given by three parameter:

- Strike angle (Φ_s) of a fault: it is the angle between the Northen direction and the trace intersection of the discontinuity plane with a horizontal reference plane: $0 \leq \Phi s \leq 2\pi$.
- Dip angle (δ) of a fault. It is the angle between the steepest declination line discontinuity plane and the horizontal line: $0 \leq \delta \leq \pi/2$.
- The direction of the slip is given by the rake (λ) measured on the fault plane as the angle between the directions of strike and slip.

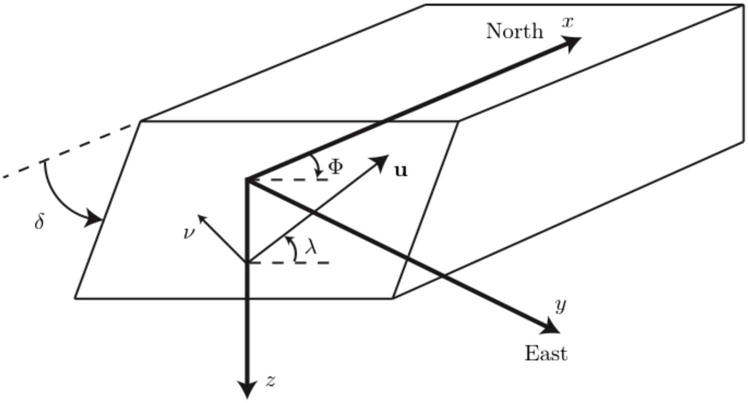

Figure 2-4: Definition of conventional parameters used to indicate fault orientation and slip direction.

In the “Input file”, we defined different parameters related to the earthquake that we want simulate, in particularly we have to define:

- ✓ Hypocenter coordinates (Lat (°). Long (°), Depth (km));
- ✓ Number of stations;
- ✓ Station coordinates (km) in a right-handed coordinate system with positive X pointing North and Y positive pointing East, with the origin corresponding to the epicenter of the earthquake;
- ✓ Length and width of the fault (km);
- ✓ Top of the fault (km);
- ✓ Velocity and density model as a function of the depth (depth(km), P-wave velocity (km/s), S-wave velocity (km/s), density (g/cm^3));
- ✓ Q_P[8] and Q_S[9] factor;
- ✓ Time-duration of the seismograms;
- ✓ Minimum and maximum resolving frequencies;
- ✓ Number of frequencies to be computed;
- ✓ Values of the slip in the grid **Ω**;
- ✓ Values of the rise time in the grid **Ω**;
- ✓ Type of svSTF: boxcar or triangle;
- ✓ Rupture velocity: the rupture velocity is defined on a regular grid and then its values are interpolated on a Ω domain.

---

[8] **Q_P**: P-wave quality (for the attenuation) factor.

[9] **Q_P**: P-wave quality (for the attenuation) factor.

- ✓ Focal mechanism (strike (°), dip (°), rake (°));
- ✓ Number of the sample points in strike and dip directions (Ω-domain);

The code is partitioned into different routines which follow the philosophy of the numerical evaluation of the representation integral.

"Triangulation" reads the fault dimensions and the number of the sample points along strike and dip directions, and generates the computational grid. Then, this routine calculates the Ω, computes the Delaunay triangulation of the fault plane and finally evaluates the area of the triangles.

On Ω-domain "Traction" generates the Green's tractions for each station, and each frequency based on: number of frequencies to be computed, minimum and maximum frequencies, velocity and density models, and the focal mechanism as read in the input file. The Green's tractions are computed by using the discrete wave-number integration technique (*Bouchon, 1981; Coutant, 1989*). This technique assumes that the Earth structure is a 1D layered medium and provides the complete wave field, so that all P and S waves, surface waves, and near-field terms are included in the synthetic seismograms. Moreover, the anelastic attenuation is modeled by this application.

"Slip_map" reads slip and rise time map in the input file, and sets the sv-STF functional form.

"Rupture_time" computes the map of rupture times on a regular grid and interpolate this map on Ω. The rupture map's is related to the rupture velocity distribution on the fault plane and it can be computed by solving the eikonal equation[10]. We used a numerical integration of the eikonal equation by a finite-difference algorithm *(Podvin and Lecomte,1991)* insuring both causality and smoothness.

The "Displacement discontinuity" computes the displacement discontinuity (1.11) in the frequency domain.

"Seismograms" evaluates the integral (eq. 1.9) by using the displacement discontinuity, triangles area, Green's traction for each frequency and each stations. Moreover, "Seismograms" computes the inverse Fast Fourier transform (FFT) to obtain the seismograms in the time domain. The formula for discrete inverse Fourier transform is:

$$h_k = \frac{1}{N \cdot \Delta t} \sum_{n:0}^{N} H_n e^{-2\pi ikn/N} \qquad (2.17)$$

in witch h_k and H_n are the samples in time and frequency domain, respectively, Δt is the time-step, N is the number of samples in the time domain (it has to be a power of two). If we want to have the displacement, we have to compute the integral in the time-domain because in the frequency domain, the integration operation corresponds to a division for 1/iω, and for ω equal zero the signal

---

[10] **Eikonal equation**: $(\nabla T)^2 = \frac{1}{c^2}$ is the relation between the time migration velocity and the seismic velocity c, the local P-wave speed or the local S-wave speed

goes to infinity; thus when the routine performs the FFT, the seismograms are affected by a leveling of the waveform. Finally, the routine writes the time velocity series in a file with three columns: N-S (North-South), E-W (East-West), U-D (Up-Down, positive in upward direction.

2.4. Validation

To validate the numerical code, synthetic seismograms were compared with the ones generated by Compsyn sxv3.11 (*Spudich and Lisheng*, 2002), a code based on a Discrete Wavenumber / Finite Element (DWFE) approach. In this test, we examined the two codes/methods associated with a forward-modelling for extended-fault earthquake rupture models.

We considered two cases of study:

a) a rupture on a vertical strike-slip fault with purely right-lateral motion;
b) a rupture on a dipping fault with purely thrust-faulting motion.

In both cases, we used the same layered isotropic velocity-density structure, simplified from the “generic” California rock-site velocity model (figure 2-5) of *Boore* and *Joyner*, (1997).

The quality factors Q_S and Q_P are assumed infinite everywhere, because the Compsyn code does not account for the anelastic attenuation.

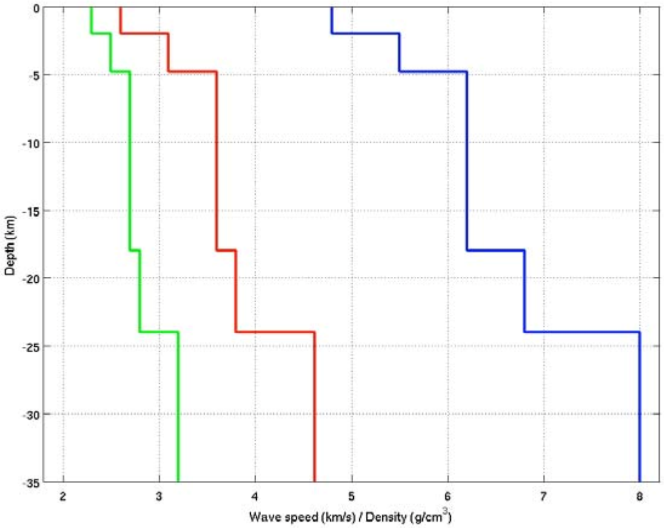

Figure 2-5: Velocity-density model for extended-fault forward-modeling simulation.

Full-wavefield forward simulation of the velocity time-series has been performed from 0.05Hz up to 5.0Hz.

This validation test is based on exercises of the Source-Inversion Validation (SIV, web site: ttp://thesiv.usc.edu/main/Home) a project, initiated and leaded by Martin Mai (KAUST).

2.4.1. Case: Strike-slip fault

In the first case-study, we generated the synthetic seismograms for a strike-slip source having the characteristics listed below:

- Dip $\delta = 90°$, Strike Φ=90°, rake λ=180°;
- Fault dimensions 13 km along-strike, 12 km down-dip;
- Discretization of rupture: node spacing is 0.5 km in each fault-plane direction;
- Seismic moment[11]: $M_0=1.658 \cdot 10^{18}$Nm (Moment magnitude[12] M_w=6.11);
- Hypocenter depth:14 km;
- Rise time variable over the fault;
- Rupture velocity variable over the fault;
- An non uniform slip distribution of slip (as shown in figure 2-6).

---

[11] **Seismic Moment**:The seismic moment M_0 is defined as:

$$M_0=\mu\cdot\text{average slip}\cdot\text{fault area}$$

where μ is shear modulus $\mu = \rho\beta^2$.

[12] **Moment Magnitude**:It is a magnitude scale, introduced by *Hanks* and *Kanamori* (1979) based on the seismic moment of an earthquake (M_w):

$$\log M_0=1.5\ M_w+16.1$$

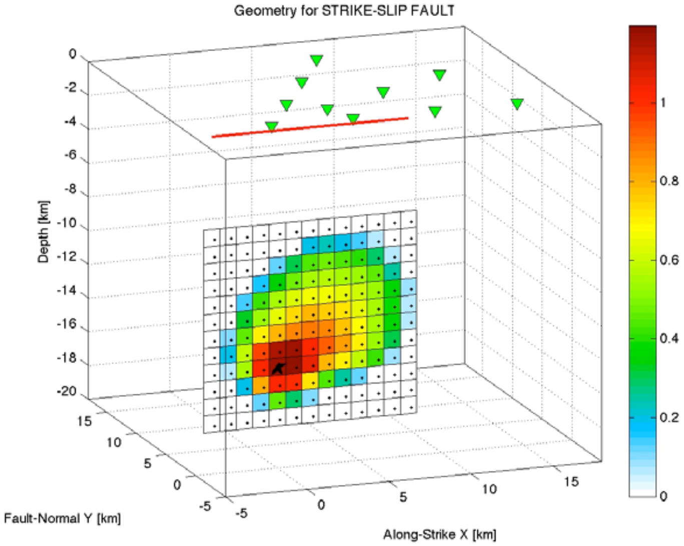

Figure 2-6: 3D-view of the rupture plane with an inhomogeneous slip distribution, colored-coded according to the amount of the slip (in m). The black star denotes the hypocenter**.**

The receivers configuration consists of three linear arrays: one fault-parallel at the surface projection of the fault and two inclined arrays at 30° and 60° from the fault parallel array (figure 2-7).

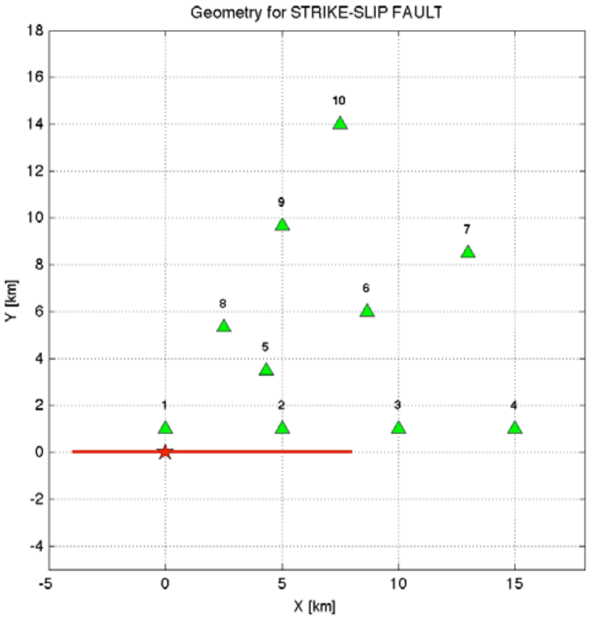

Figure 2-7: Source-receiver geometry for a strike-slip fault case. The red star shows the epicenter at X=0, Y=0 in a right-handed coordinates system with positive X pointing East, positive Y pointing North. The red line indicates the vertical projection of the updip-edge of an extend fault plane at depth.

On the ground of these parameters, we simulated the velocity seismograms with the STuDenT code and with Compsyn.

We show the three components of the time series in figure 2-8, and the spectral amplitudes in figure 2-9. The seismograms generated by STuDenT are in red, while the seismograms generated by Compsyn are in black.

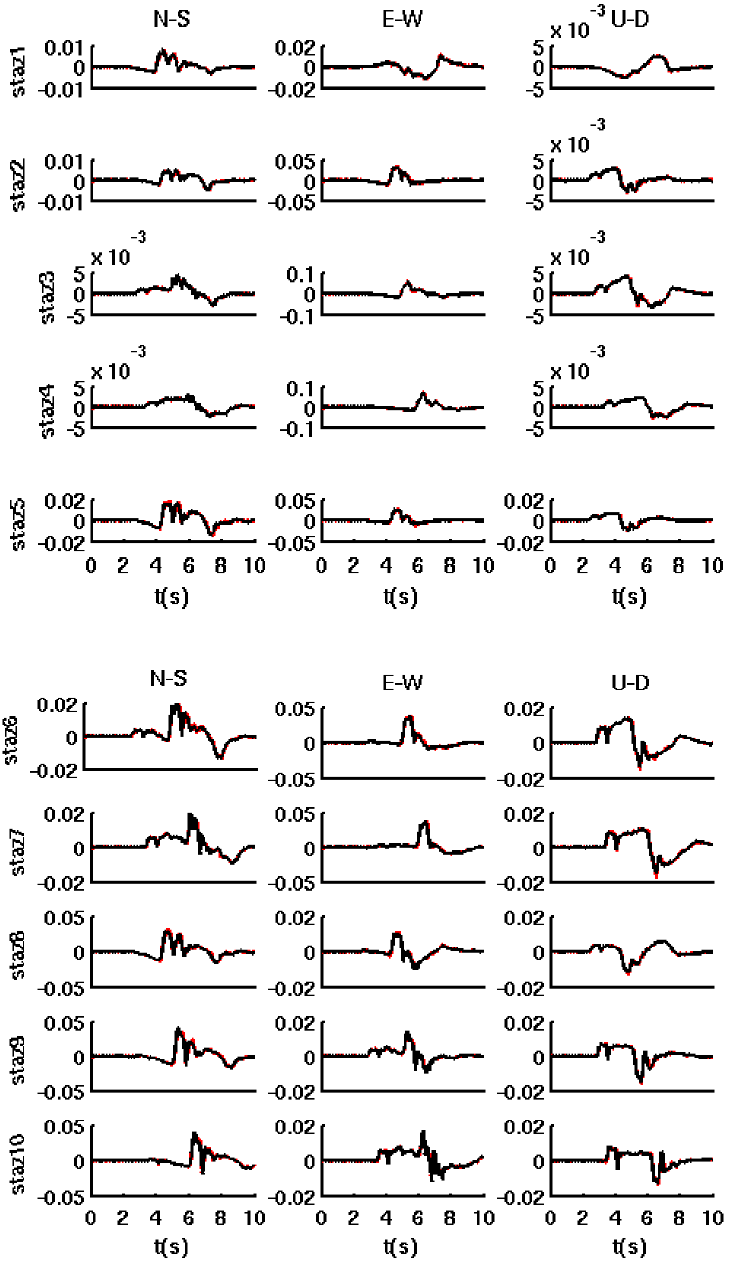

Figure 2-8: Comparison between STuDenT and Compsyn for all ten station, and for the three component (N-S: North-South; E-W: East-West; U-D: Up-Down). The seismograms generated by STuDenT are in red, while the seismograms generated by Compsyn are in black. Each pair of theoretical seismograms is plotted with its amplitude scale (m/s).

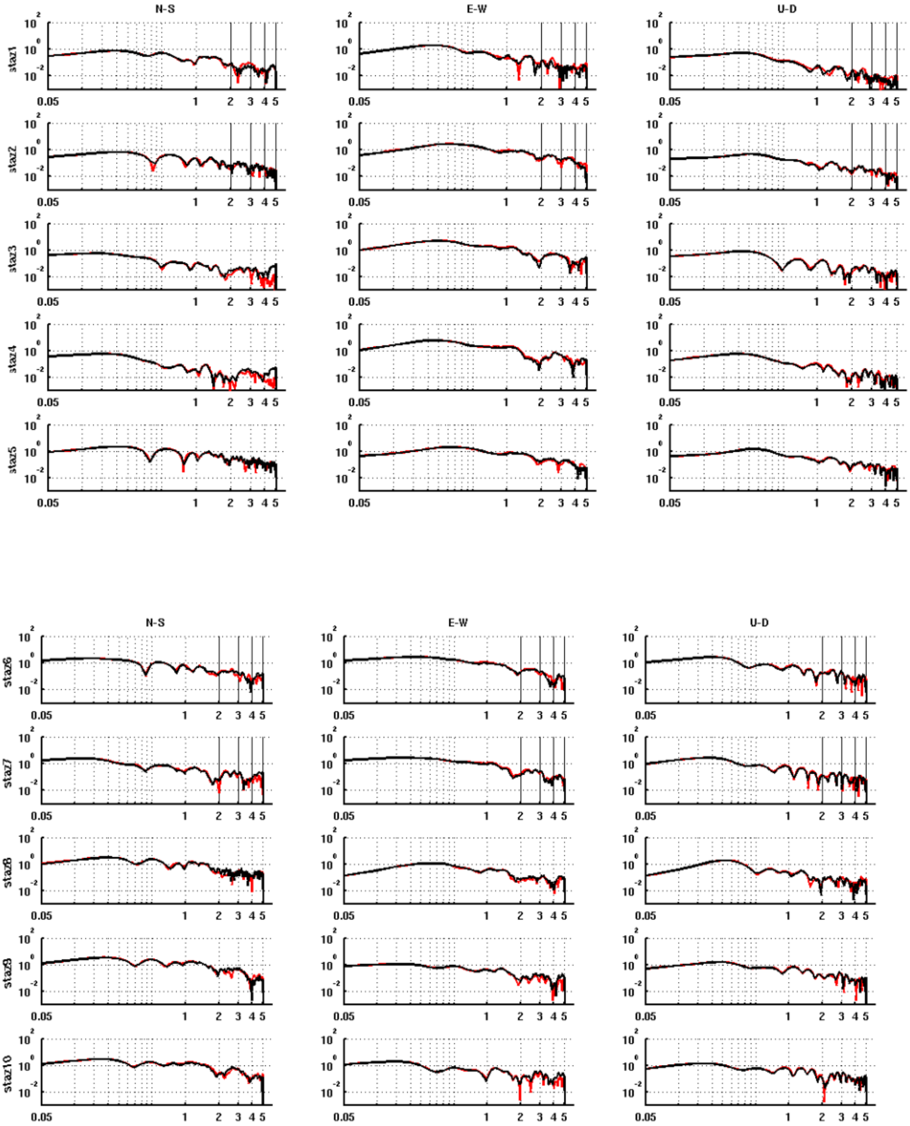

Figure 2-9: Comparison, in frequency domain, between STuDenT (red) and Compsyn (black) for all ten stations, and for the three component (N-S: North-South; E-W: East-West; U-D: Up-Down).

The general match is good, and the small differences between pairs of signals are due to the different interpolation procedure of the slip, the rise-time and the rupture velocity map of the two codes.

For a quantitative comparison between the seismograms, we used a misfit criteria in time and frequency domains developed by *Kristekova et al.* (*2006*), and based on the continuous wavelet transform of the signals. The time frequency envelope misfit (TFEM) and time frequency phase misfit (TFPM) are calculated according to eq. A.5 and A.6 respectively (see Appendix A). TFEM (t, f) characterizes the difference between the envelopes of the signals, as a function of the time and frequency. In the same way, the TFPM (t, f) characterizes the difference between the phases of the signals, as a function of the time and frequency.

We performed this analysis for three stations: stz01, stz04, stz10 (figures 2-10, 2-11, 2-12). Red color in the TFEM and the TFPM images indicates a larger amplitude and a positive phase shift in the STuDenT seismograms with respect to Compsyn seismograms. Blue color represents the opposite case.

In figure 2-10 we show the analysis for the station 01. From 5 to 10 seconds, the STuDenT amplitudes, for each component, are overestimated: the envelope misfit value is 20%. The differences in amplitudes are evident from 0.4 to 5.0 Hz. The phase misfit is close to zero in the rest of the (t, f) diagram.

We are not able to distinguish an evident phase shift in the seismograms of station 04 (figure 2-11). In fact, the phase misfit is close to zero. Generally, the N-S and U-P components are overestimated and the envelope misfit has its maximum value: (about of 20%) in a part of plane (t, f) from (5 s, 0.7 hz) to (8s, 5 hz).

In figure 2-12, we can see that the envelope misfit is about zero all the duration, but the phase misfit is characterized by negative values (around 10%): the STuDenT seismograms have a negative phase shift respect to a Compsyn signals, as evidence in the plots of the seismograms, in the top of the figure.

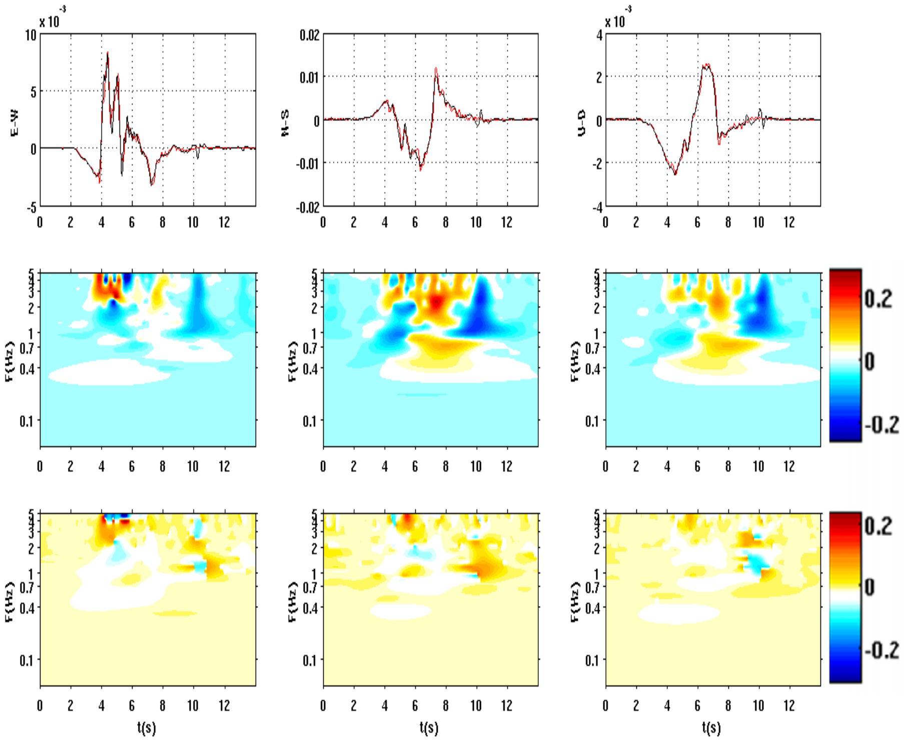

Figure 2-10: Analysis for station 01. (Top) Comparison between STuDenT (red) and Compsyn (black) synthetic seismograms (Middle) Time-frequency envelope misfit TFEM(t, f) and (Bottom) time-frequency phase misfit TFPM(t, f) plots. Columns show E-W (right), N-S (center), U-D components (left), respectively. Red color in the TFEM and the TFPM images indicates a greater amplitude and a positive phase shift in the STuDenT seismograms with respect to Compsyn seismograms. Blue color represents the opposite case.

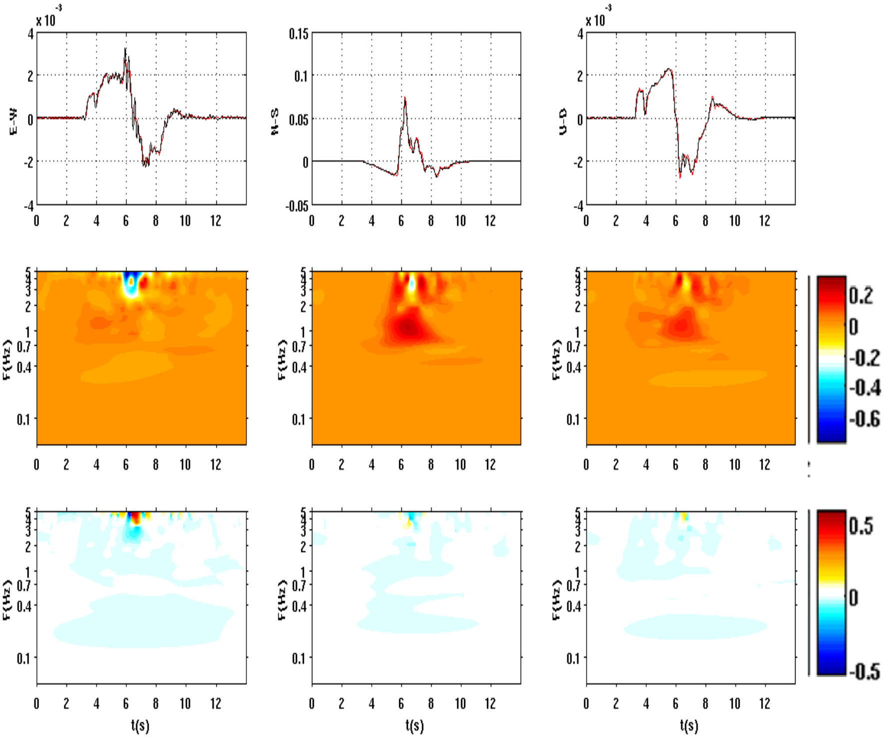

Figure 2-11: Analysis for station 04. (Top) Comparison between STuDenT (red) and Compsyn (black) synthetic seismograms (Middle) Time-frequency envelope misfit TFEM(t, f) and (Bottom) time-frequency phase misfit TFPM(t, f) plots. The color scale have the same interpretation of figure 2-10.

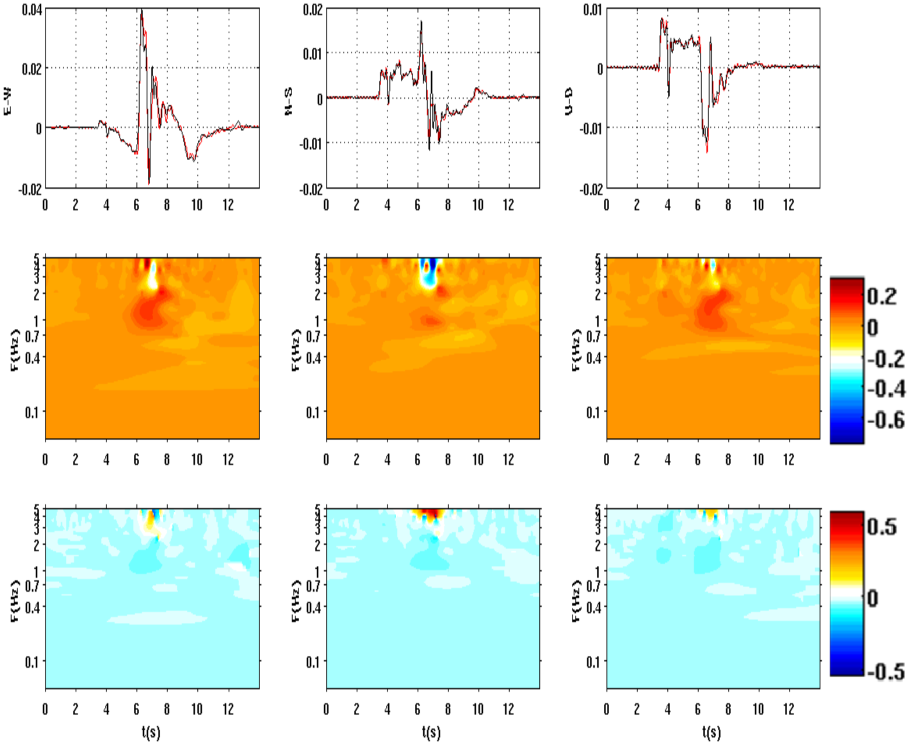

Figure 2-12: Analysis for station 10. (Top) Comparison between STuDenT (red) and Compsyn (black) synthetic seismograms (Middle) Time-frequency envelope misfit TFEM(t, f) and (Bottom) time-frequency phase misfit TFPM(t, f) plots. For the color scale interpretation see the figure 2-10.

2.4.2. Case: Dip-slip fault

In the second case study, we generated the synthetic seismograms for a dip-slip source, with the characteristic listed below:

- $\delta = 40°$, Φ=270°, λ=90°;
- Fault dimensions: 13 km along-strike, 13 km down-dip;
- Discretization of rupture: node spacing is 0.5 km in each fault-plane direction;
- Seismic moment: $M_0=1.824 \cdot 10^{18}$Nm (M_w=6.14);
- Hypocenter depth 9.785 km;
- Rise time and rupture velocities variable over the fault;
- A non uniform slip distribution as shown in figure 2-13.

The receivers configuration consists of three linear arrays: one fault-parallel at 1 km from the surface projection of a vertical fault and two inclined arrays at 30° and 60° from the fault parallel array. These three arrays are then mirrored across the X=0 surface-projection of the fault to capture both hanning-wall and foot-wall sites (figure 2-14).

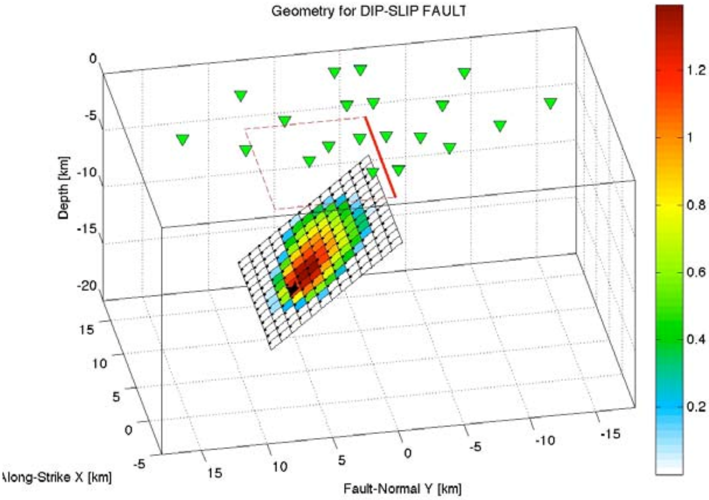

Figure 2-13: 3D-view of the rupture plane with an inhomogeneous slip distribution, colored-coded according to the amount of the slip (in m). The black star denotes the hypocenter.

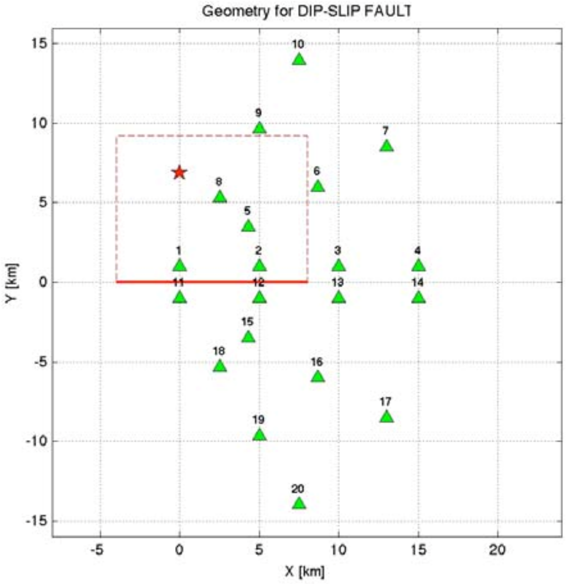

Figure 2-14: Source-receiver geometry. for a dip-slip fault case. The red star shows the epicenter at X=0, Y=0 in a right-handed coordinates system with positive X pointing East, positive Y pointing North. The red line indicates the vertical projection of the updip-edge of an extend fault plane at depth.

On the ground of these parameters, we simulated the velocity seismograms with the STuDenT and Compsyn codes.

Figure 2-15 shows the comparison between the three components of the time series: the STuDenT seismograms are in red while the seismograms generated by Compsyn are in black. Figure 2-16 shows the comparison between spectral amplitudes of the two synthetic seismograms, with the color convention previously used. Finally, we compared the results with the time-frequency misfit criteria (Appendix A), for stations 01, 10, 14, 18.

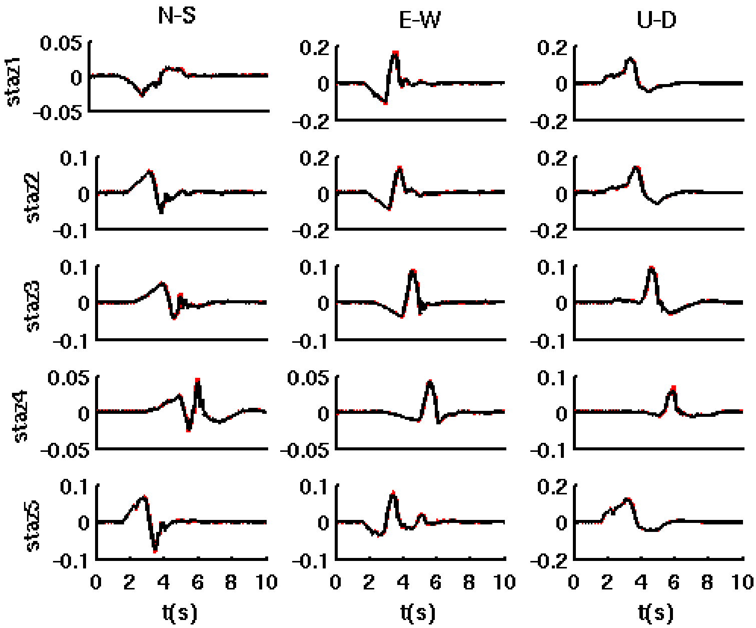
N-S
E-W
U-D
staz1
staz2
staz3
staz4
staz5
0.05
0
-0.05
0.2
0
-0.2
0.1
0
-0.1
0 2 4 6 8 10
t(s)

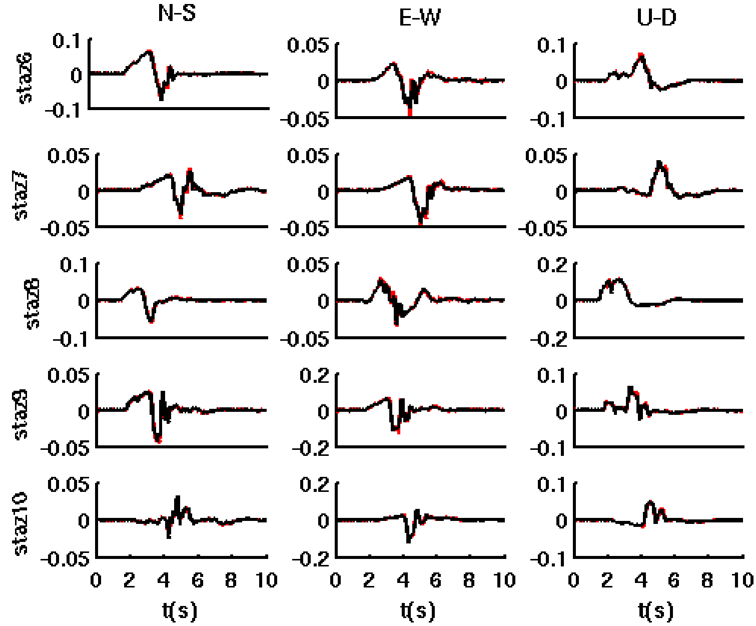
N-S
E-W
U-D
staz6
staz7
staz8
staz9
staz10
0.1
0
-0.1
0.05
0
-0.05
0.2
0
-0.2
0 2 4 6 8 10
t(s)

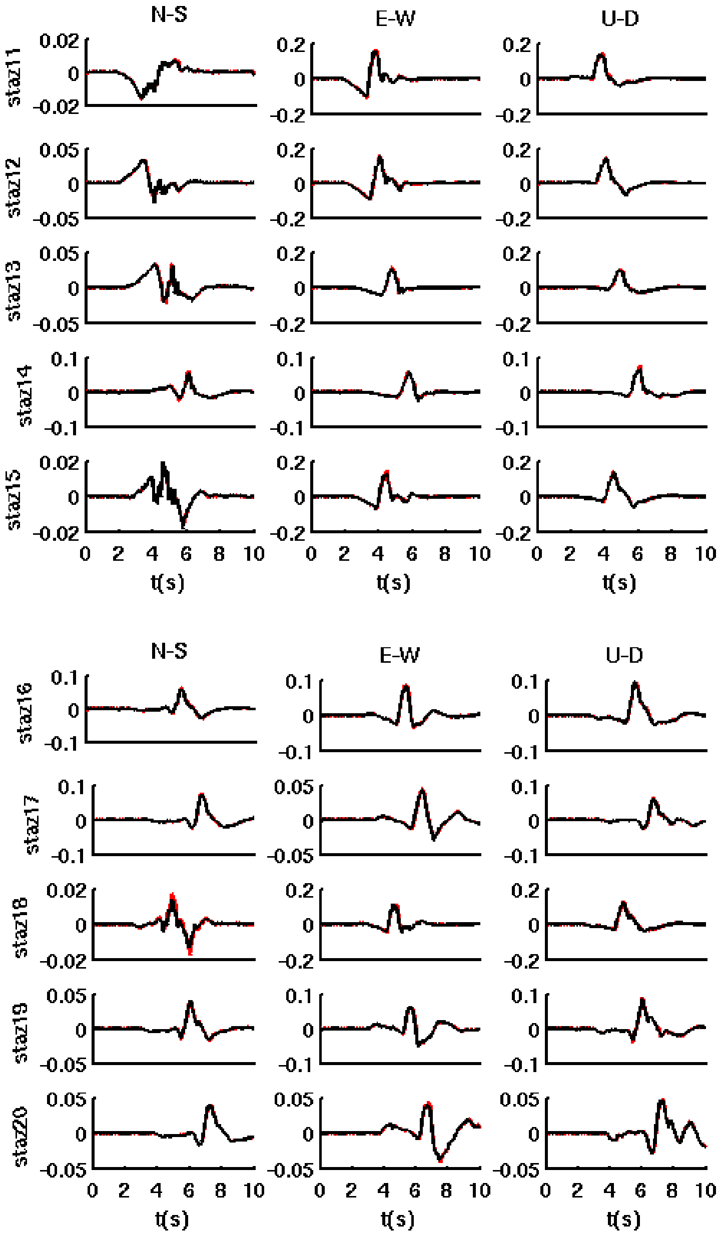

Figure 2-15: Comparison between STuDenT and Compsyn for all 20 stations, and for the three component (N-S: North-South; E-W: East-West; U-D: Up-Down). The seismograms generated by STuDenT are in red, while the seismograms generated by Compsyn are in black. Each pair theoretical seismograms are plotted with its amplitude scale (m/s).

Case: Dip-slip fault

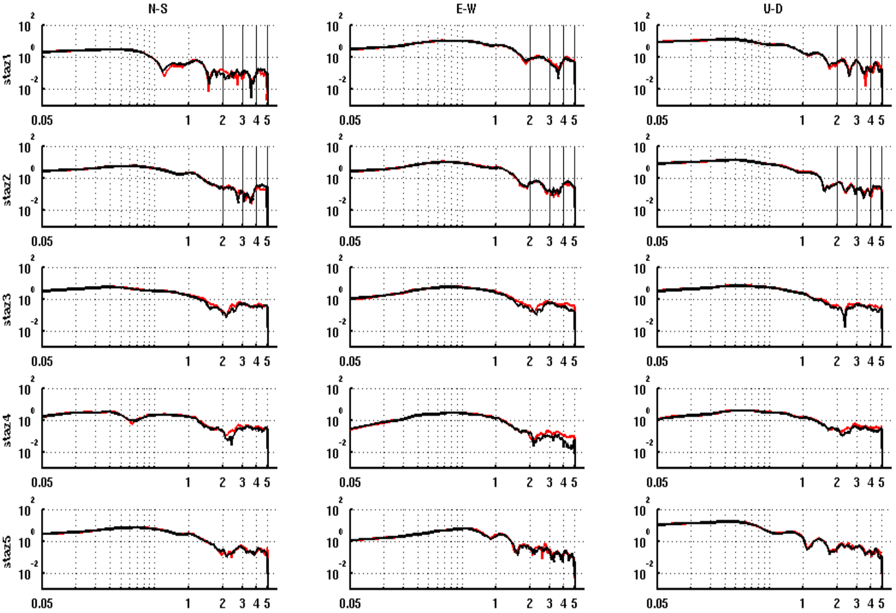

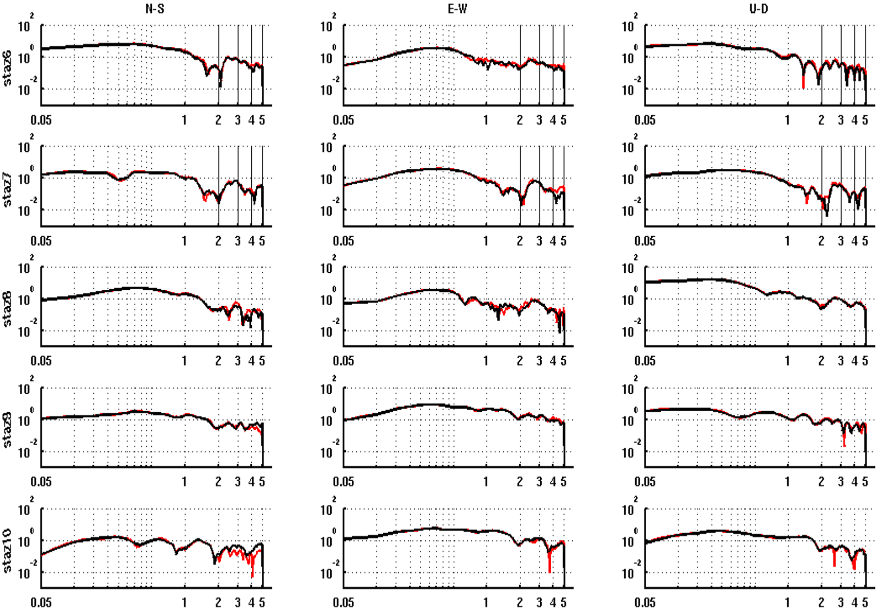

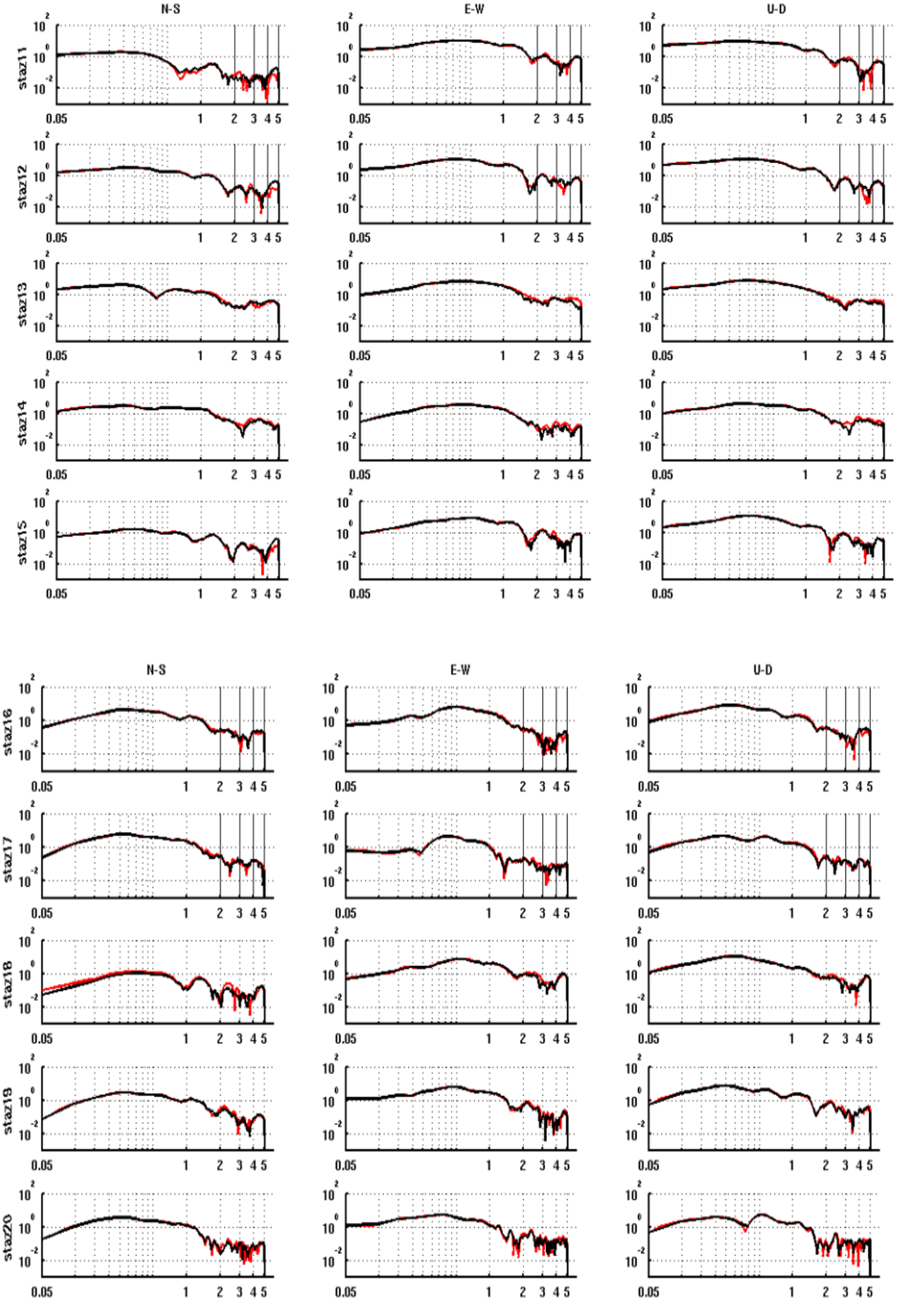

Figure 2-16: Comparison, in frequency domain, between STuDenT (red) and Compsyn (black) for all 20 stations, and for the three component (N-S: North-South; E-W: East-West; U-D: Up-Down).

In figures 2-17 2-18 2-19 2-20, the TFEM and the TFPM misfit for stations 01, 10, 14, 18 are respectively shown.

The E-W component of station 01 (figure 2-17), has large differences between the two seismograms and we can see the maximum envelope misfit, of about 10%, in correspondence of 3s and 5s. For all three components, there is a phase shift, of about 15%, around 1s and 4 s: the STuDenT seismograms are anticipated with respect to the Compsyn seismograms. The maximum differences are in the part of the plane (t, f)=([2, 6]s, [1.5, 5]hz).

For station 10, in figure 2-18, the comparison is good: the envelope and phase misfit is minimum in a large part of the (f, t) plane, with small differences localized around the peak amplitude (from 4s to 5s).

The comparison for station 18, is shown in figure 2-20. The E-W component has the envelope misfit larger (25%) than other components, in a part of (t, f) plane from 0.3-5 Hz and 2-10s. In this range for the time and frequency values, the STuDenT seismograms have negative phase shifts, so the phase misfit is negative (around 5%) in large part of the plane (t, f).

In general, the E-W component of the stations 01 and 18 shows heterogeneous envelope and phase misfit values and the difference in amplitude and phase between the synthetic seismograms computed by two codes increases at higher frequency.

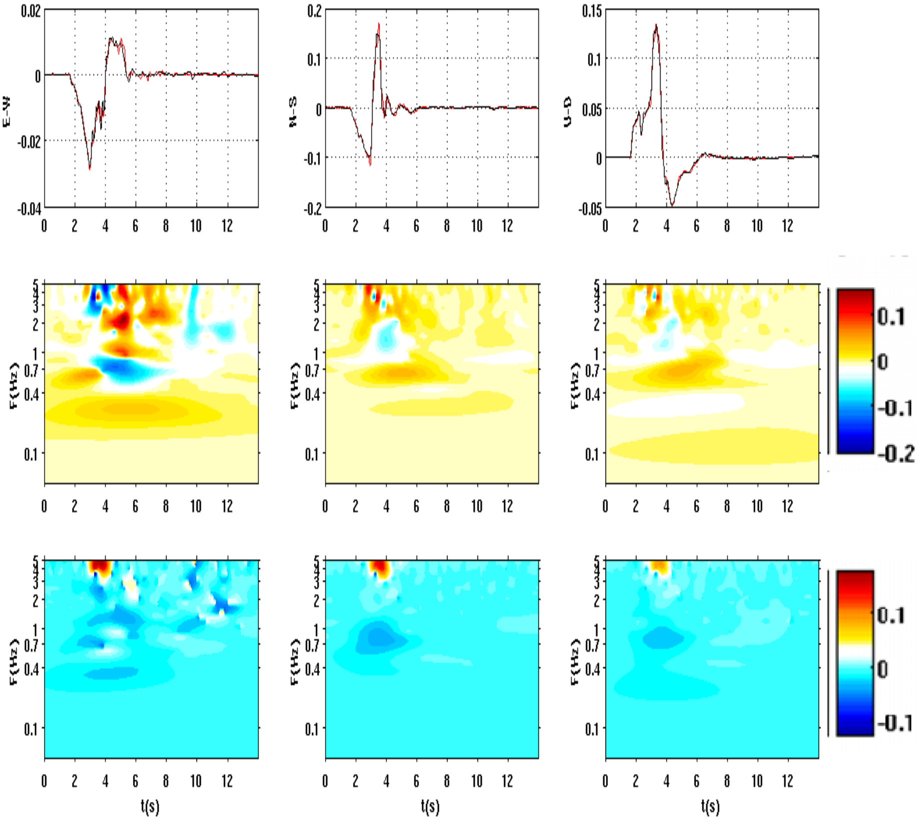

Figure 2-17: Analysis for the station 01. (Top) Comparison between STuDenT (red) and Compsyn (black) synthetic seismograms (Middle) Time-frequency envelope misfit TFEM(t, f) and (Bottom) time-frequency phase misfit TFPM(t, f) plots. Columns show E-W (right), N-S (center), U-D components (left), respectively. Red color in the TFEM and the TFPM images indicates a greater amplitude and a positive phase shift in the STuDenT seismograms with respect to Compsyn seismograms. Blue color represents the opposite case.

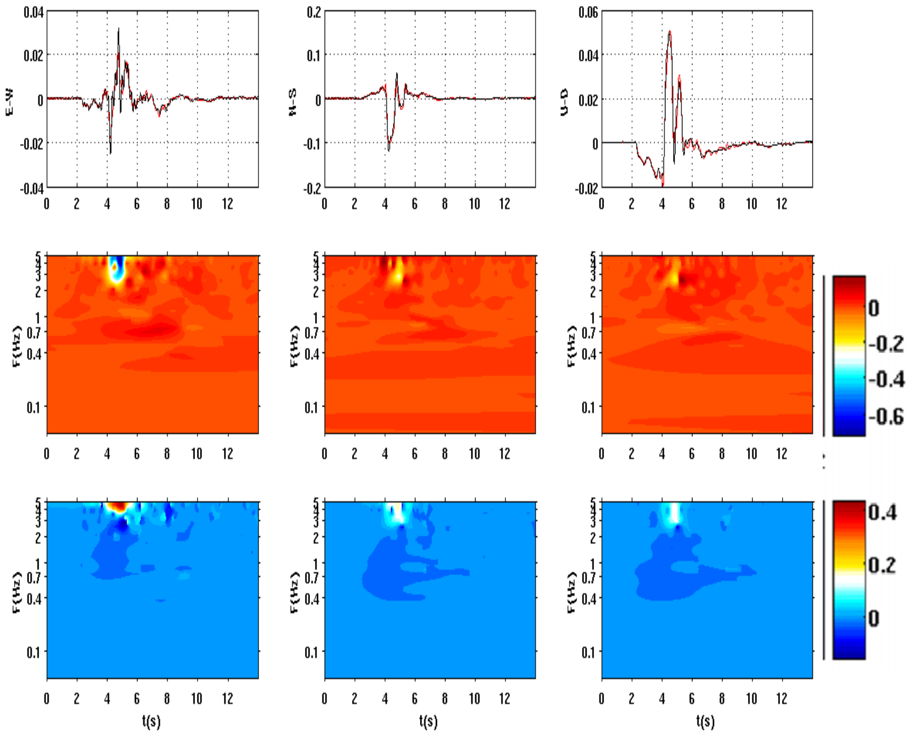

Figure 2-18: Analysis for the station 10. (Top) Comparison between STuDenT (red) and Compsyn (black) synthetic seismograms (Middle) Time-frequency envelope misfit TFEM(t, f) and (Bottom) time-frequency phase misfit TFPM(t, f) plots. Columns show E-W (right), N-S (center), U-D components (left), respectively.

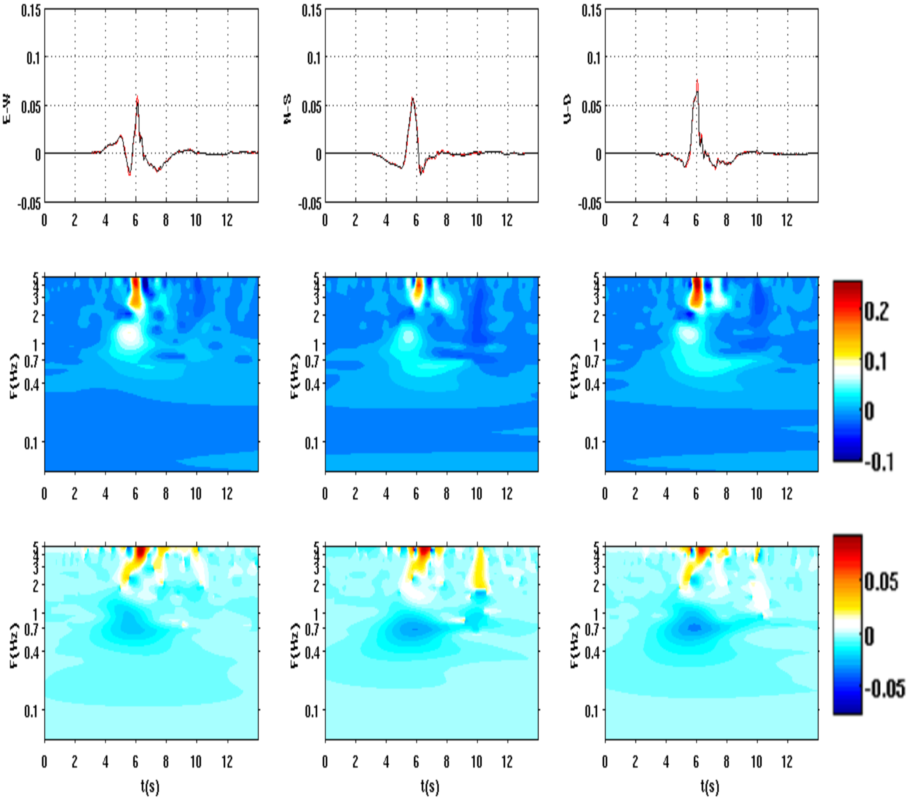

Figure 2-19: Analysis for the station 14. (Top) Comparison between STuDenT (red) and Compsyn (black) synthetic seismograms (Middle) Time-frequency envelope misfit TFEM(t, f) and (Bottom) time-frequency phase misfit TFPM(t, f) plots- Columns show E-W (right), N-S (center), U-D components (left), respectively.

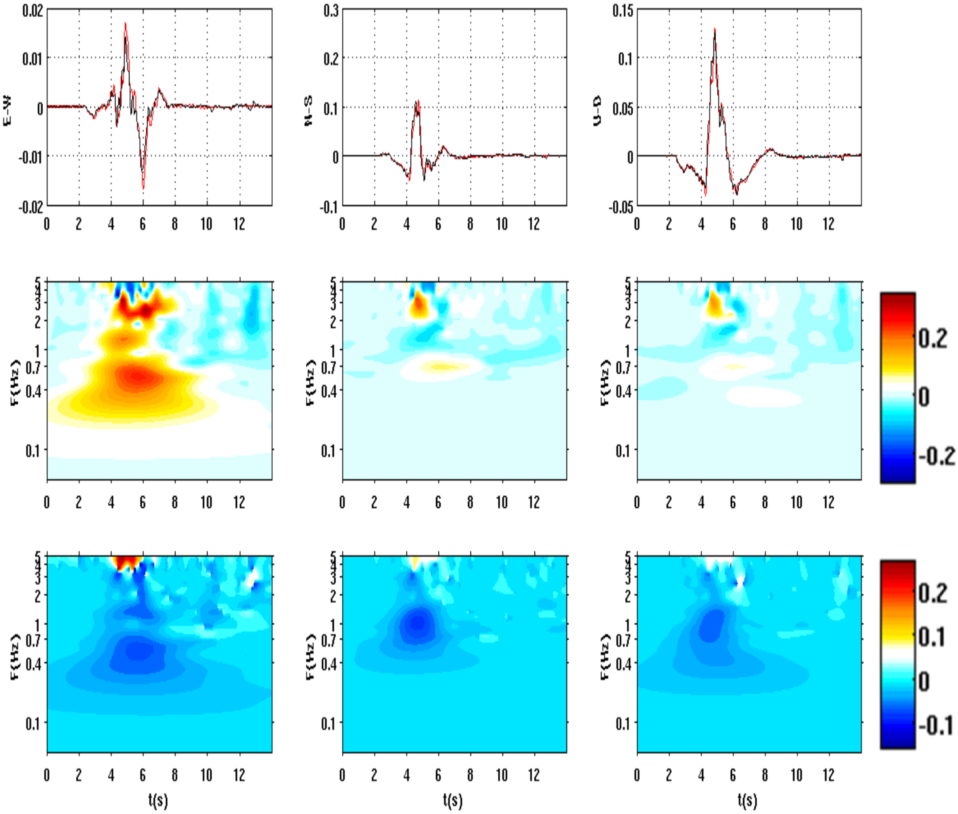

Figure 2-20: Analysis for station the 18. (Top) Comparison between STuDenT (red) and Compsyn (black) synthetic seismograms (Middle) Time-frequency envelope misfit TFEM(t, f) and (Bottom) time-frequency phase misfit TFPM(t, f) plots- Columns show E-W (right), N-S (center), U-D components (left), respectively. Red color in the TFEM and the TFPM images indicates a greater amplitude and a positive phase shift in the STuDenT seismograms with respect to Compsyn seismograms. Blue color represents the opposite case.

2.4.3. Conclusion

In this thesis we developed a new methodology to compute synthetic seismograms using a finite element integration over triangle. We reduced the representation integral to a simple product of triangles area and the average of the function in the three nodes of a grid of points referred to the single triangle. We have constructed a representation theorem in which are well separated the parties relating to the seismic source and the effect of propagation. Generally, the computation of Green's traction is independent on the slip on fault plane, so for a given source-station configuration we can generate a data-base of a Green's traction to be called when it is necessary.

The STuDenT code is computationally fairly fast compared to other codes, because it works in frequency domain; in this way the user can simulate ground motions from many hypothetical rupture and slip models in a small time, also it is very friendly to use.

In comparison with Compsyn, another method to simulate a ground motion, we observed discrepancies in amplitude, time-shifts and different frequency content, in particularly at high frequency. Probably, it is given by different methodology to work on the frequency maximum that we want have maximum resolution and because in the Compsyn there are many parameters that depend on the user and it comports different approximation and possible error in the estimation of Green's traction. The differences in amplitude may be due to a different way to interpolate the slip rupture velocity, and rise time input maps for the two different methodologies.

Chapter 3

Slip parameterization

3.1. Introduction

The original pioneering works on slip parameterization have been proposed during the early 1980s. To this aim, a given fault was usually divided into a number of subfaults (e.g., *Olson and Apsel*, 1982; *Hartzell and Heaton*, 1983). These subfaults are then used to construct a number of forward models which are finally combined to produce an overall kinematic rupture model. In each subfault the slip is constant, everywhere, positive and smooth in all fault plane. The subfault dimensions are generally chosen to accommodate the high-frequency content of the strong motion synthetic records.

Recent improvements in analysis methods, computational resources, and seismological and geological observations, enable us to image earthquake sources in detail. The most detailed images of such sources have been obtained using data recorded near to the earthquake causative fault through inversion techniques. Results revealed the source kinematic parameters of earthquake slip over the fault plane. Concerning the slip in this chapter, we introduce an innovative parameterization of the problem. Particularly, we assume a spatial slip distribution obtained combining overlapping 2D Gaussian functions defined on regular grid on the fault. At any given point, temporal evolution of slip is described with an a priori prescribed slip-velocity function, while rupture velocity and rise time parameters are assumed as free parameters and the result of the inversion is the amplitude of the on the fault plane.

3.2. Overlapping 2D Gaussian functions

The complexity of the distribution on the fault plane is here represented through a superposition of overlapping 2D Gaussian functions.

Let us assume a coordinate system on the fault plane having axes parallel to the strike and dip directions. In this system each point of the fault is represented by its coordinates $\vec{\xi} = (\xi_1, \xi_2)$. For a given set of points $\vec{\xi}_i = (\xi_{1i}, \xi_{2i})$ on the fault we represent a function Φ as a linear combination of 2D Gaussians:

$$\Phi(\vec{\xi}) = \sum_{i=1}^{n} A_i \, e^{-\frac{\left\|\vec{\xi}-\vec{\xi}_i\right\|^2}{\sigma_i^2}} \qquad (3.1)$$

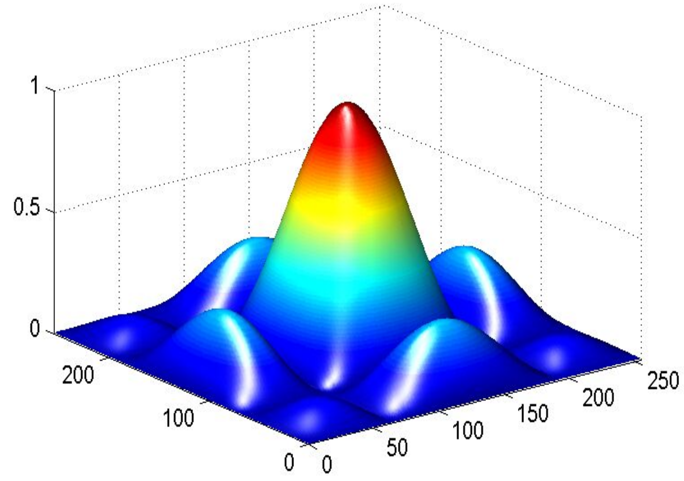

Figure 3-1: An example of overlapping 2D Gaussian function.

where A_i and σ_i are amplitude and width of the i-th Gaussian, respectively.

For any given point on the fault plane, the relative weight of each bidimensional Gaussian function to Φ depends only on the distance between the considered point and the Gaussian center, normalized by the Gaussian width. The contribution of each Gaussian can be considered negligible at distances larger than three standard-deviations. If the Gaussian widths are smaller than both the length and the width of the fault, such a representation is indeed local on the fault plane.

Several advantages occur when using such a representation for the slip function. First, the slip map is naturally smooth since it is continuous, many times differentiable and tapered to zero at the boundaries of the fault plane. Moreover, Gaussian functions have an almost flat amplitude spectrum up to a corner wavenumber that is related to the inverse of the Gaussian width; then, the spectrum decays exponentially beyond it. Finally, this parameterization is expected to relate the slip map to the minimum resolvable wavelength on the fault plane and, through it, to the maximum analyzed frequency in the data, how we will discuss in the next paragraph. Finally, the positivity constrain is naturally insured by requiring positive coefficients in the Gaussian representation. On the other hand, Gaussian functions, being positive defined, are not orthogonal and then the possibility to represent any function through a Gaussian representation needs to be investigated.

When using such a parameterization in the inversion of strong-motion data for retrieving the slip distribution on the fault, it is preferable not to jointly invert for the slip amplitude, the location of the Gaussian centers and the Gaussian widths, because the problem becomes strongly non-linear. In such a latter case, the correlation between the different parameters needs to be overcome by limiting the number of asperities on the fault to a very few (*Vallée and Bouchon, 2004*). The aim here is rather to preserve the linearity of the problem with respect to the slip at the cost of increasing the number of free-parameters on the fault plane. We indeed fix both the positions of the centers, which are chosen to be equally spaced on the fault plane and the width, which is the same for all the Gaussian functions.

3.2.1. The overlapping parameter

Let us define $\Delta\xi$ as the distance between two close centers and σ the Gaussian width: the only distance which matters in the problem is the Euclidean distance normalized by the Gaussian width. We define the amount of overlapping as:

$$\chi = \frac{\sigma}{\Delta\xi} \tag{3.2}$$

As the overlapping goes to infinity ($\Delta\xi \to 0$), the representation becomes the Gaussian filtered version of the dislocation distribution, with cut-off wavelength at σ. For a finite overlapping the representation is the discrete version of the Gaussian filter. In particular, if χ is large, Gaussian functions are very close to each other and the representation is influenced by any single Gaussian function. On the contrary, if the overlapping parameter is small, Gaussian functions could be very distant and asperities may be retrieved only at the scale and at the location of the single Gaussian functions. Hence, we expect that the quality of the solutions degrades with the decreasing of the overlapping.

To understand the role of the overlapping, we briefly analyze the simple case of two overlapping Gaussian functions in one dimension. We assume that they have the same width but different amplitudes:

$$\Psi(\xi) = A_1 e^{-\frac{\xi^2}{2\sigma^2}} + A_2 e^{-\frac{(\xi-\Delta\xi)^2}{2\sigma^2}} \qquad (3.3)$$

where A_1 and A_2 are the amplitudes and $\Delta\xi$ is the position of the center of the second Gaussian function, with respect to the origin where the first one is centered. The Fourier transform in space domain of equation (3.3) is given by

$$\Psi(k) = \sqrt{2\pi}\sigma e^{-\frac{k^2\sigma^2}{2}} (A_1 + A_2 e^{ik\Delta\xi}) \qquad (3.4)$$

where k is the wavenumber, and the resulting squared amplitude spectrum is

$$|\Psi(k)|^2 = 2\pi\sigma^2 e^{-\frac{k^4\sigma^4}{4}} \left[A_1^2 + A_2^2 + 2A_1A_2\cos\left(k\Delta\xi\right)\right] \qquad (3.5)$$

If we define the normalized wavenumber as $\hat{k} = \sigma^{-1}k$, the above expression simplifies to

$$\left|\Psi\left(\hat{k}\right)\right|^2 = 2\pi\sigma^2 e^{-\frac{\hat{k}^4}{4}} \left[A_1^2 + A_2^2 + 2A_1^2A_2^2\cos\left(\chi\hat{k}\right)\right] \qquad (3.6)$$

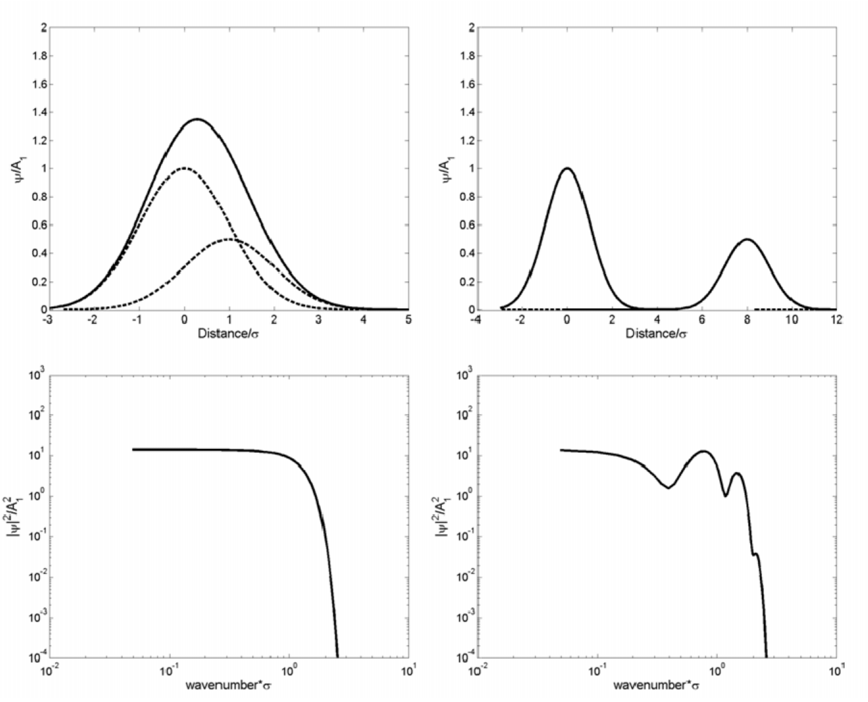

Figure 3-2: Addition of two overlapping Gaussian functions in one dimension. In the top panels we plot two overlapping functions (dashed lines) and their sum (solid line). The ratio between the peak amplitudes is two. In the left figure, the overlapping is large and the sum is still peaked, with a width larger than the width of the initial Gaussian functions. On the right, instead, the overlapping is small and the sum shows two isolated peaks. In the bottom panels, we represent the square amplitude of the Fourier spectra of the sum function, plotted in the above panels. When the overlapping is large the spectrum decays as a standard Gaussian filter, with a cutoff wavenumber comparable with 1/σ. In the right panel, the influence of the distant Gaussian functions results in an oscillating spectrum, for wavenumbers smaller than σ.

The amplitude spectrum is the product of the single amplitude Gaussian spectrum, times a cosine type function, which can introduce some oscillations. In top panels of figure 3-2, we represent the effect of the overlapping on the final sum in the space domain. We analyze two cases: on the left we have a large overlapping ($\chi = 1$), on the right a smaller one ($\chi = 0.125$). We also set the ratio between the two Gaussian function amplitudes $A_1 / A_2 = 2$. We note that, when the overlapping is large, the sum of the Gaussian functions has still a peaked shape and a width slightly larger than σ. On the other hand, when the overlapping is small (top-right panel), the sum reflects the shape of the single Gaussian functions showing two isolated peaks. On the bottom panels, we plot the squared amplitude spectrum of the sum. While in the left figure the spectrum is flat up to a cutoff wavenumber, in the right panel, the spectrum oscillates, indicating that, when the overlapping is small, the wavelengths ranging between Δξ and σ are poorly represented. The influence of the cosine function depends on the ratio A_1 / A_2 and is maximum when $A_1=A_2$. In such a case the spectrum can go to zero and the holes become more pronounced. For this simple case, we can hence derive a minimum condition for the overlapping:

$$\chi > \frac{1}{\pi} \tag{3.7}$$

This property allows to push the zeroes of the cosine function beyond the cutoff wavenumber of the Gaussian function.

We can easily extend this simple analysis to the case of the sum of several 1D Gaussian functions, equally spaced along the x axis. In such a case, additional cosine-type functions are summed-up in the amplitude spectrum, with relation to the interference between the Gaussian functions, whose centers are at 2Δξ , 3Δξ,

…, n $\Delta\xi$. As a consequence, their effect appears in the spectrum at wavelengths of the order of $2\Delta\xi$, $3\Delta\xi$, .., n $\Delta\xi$, but their weight decreases as n increases.

For 2D applications, we note that the Gaussian representation may be factorized in a tensional product of 1D Gaussian functions[13], having the same σ in a strike and dip direction (figure 3-3):

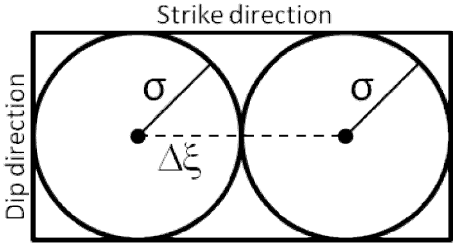

Figure 3-3: Example of 2D Gaussian function.

$$\left|\Psi\left(\hat{k}_s,\hat{k}_d\right)\right|^2 = 2\pi\sigma^2 e^{-\frac{\hat{k}_s^4}{4}} e^{-\frac{k_d^4}{4}}\left[A_1^2 + A_2^2 + 2A_1^2 A_2^2 \cos\left[\chi\left(\hat{k}_s + \hat{k}_d\right)\right]\right] \tag{3.8}$$

where $\hat{k}_s$ and $\hat{k}_d$ are the normalized wavenumbers in strike and dip directions, respectively. Hence, we have the same behavior along the strike and dip axes.

Now we consider the case of four 2D Gaussian functions, having the same σ and the same distance of the centers in two directions

---

[13] **Linear separability property of Fourier transform**: The Fourier transform in higher dimensions is given by

$$f(x,y) \rightarrow F(u,v) = \int_{-\infty}^{+\infty} f(x,y)\exp\left(-i2\pi(ux+vy)\right)dx\,dy$$

If the f(x,y) function is separable f(x,y)=f(x)f(y), the Fourier transform of a separable function is also separable: F(u,v)=F(u)F(v).

(figure 3-4). We can factorize the problem in the two, strike and dip, directions:

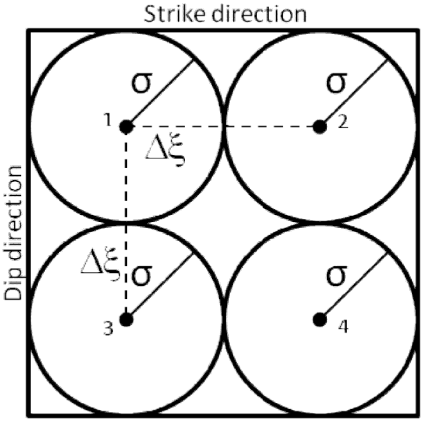

Figure 3-4: Four 2D Gaussian function, having the same σ and the same distance between centers.

$$\left|\Psi\left(\hat{k}_s,\hat{k}_d\right)\right|^2 = \left(A_1^2 + A_2^2 + A_3^2 + A_4^2\right) + \left[2\left(A_1A_2 + A_3A_4\right)\cos\left(\chi\,\hat{k}_s\right)\right] + \left[2\left(A_1A_3 + A_2A_4\right)\cos\left(\chi\,\hat{k}_d\right)\right] + \left[2A_1A_4\cos\left[\chi\left(\hat{k}_s + \hat{k}_d\right)\right]\right] + \left[2A_2A_3\cos\left[\chi\left(\hat{k}_s - \hat{k}_d\right)\right]\right] \tag{3.9}$$

The behavior of the spectra, for the 1-2 and 3-4 Gaussian functions, is the same of the previous case: the first three terms describe the different contribution along strike and dip separately.

The last two terms combine the 1-4 and 3-2 Gaussian functions, in a mixed way.

Since the distance between the centers increases in the 45° direction, the space resolution decreases along this direction. However, a lower resolution at 45° is common to all parameterizations defined on regular grids oriented along the strike and dip directions.

Finally, the effect of fixing the location of centers of the Gaussian functions may introduce an aliasing effect: the “true” slip map, at the resolved wavelength, could be translated of $\pm\Delta\xi/2$, with respect to the inverted one.

3.3. Relationship between the Gaussian width and the minimum resolvable wavelength

We investigate the relationship between the Gaussian width and the minimum resolvable wavelength, studying the spectrum as a function of the width and overlapping, for different slip maps.

3.3.1. The projection of slip map onto Gaussian representation: the method

To the purpose, we project several heterogeneous k-square slip distributions[14] (*Gallovič and Brokesova, 2004)* by different Gaussian representations via an L_2 minimization.

---

[14] **k-square model:** The 2D slip distribution D($\vec{k}$), where $\vec{k}$ = (k_x, k_z), for a rectangular fault of length L and width W is described by its spatial Fourier spectrum:

$$D(k_x, k_y) = \frac{\Delta\bar{u}LW}{\sqrt{1+\left(\left(\frac{k_x L}{\gamma}\right)^2+\left(\frac{k_y W}{\gamma}\right)^2\right)^2}}e^{i\Phi(k_x,k_y)}$$

The problem of obtaining the static slip distribution on a fault plane is resolved using a technique analogous to the time-reverse method that is typically used in the seismic tomography studies (*Tromp et al.*, 2005). In such methods, the gradient of the misfit Λ with respect to the model parameters p_i is analytically derived as

$$\Delta\Lambda = \sum_{i=1}^{num\_par} \frac{\partial\Lambda}{\partial p_i}\Delta p_i \qquad (3.10)$$

and then used in minimization procedure based on conjugate gradient technique (*Press et al., 1992)*.

We define the misfit as the L_2 norm between synthetic, s_{theo}, and observed, s_{obs}, slip, the latter assumed as reference slip map:

$$\Lambda = \frac{1}{2}\iint \left(s_{ref}(x,y) - s_{gau}(x,y)\right)^2 dxdy \qquad (3.11)$$

where s_{gau} is given by:

$$s_{gau}(x,y) = \sum_{i=1}^{num\_par} A_i e^{-\frac{(x-x_i)^2+(y-y_i)^2}{\sigma_i^2}} \qquad (3.12)$$

---

where $\Delta\bar{u}$ denotes the mean slip and γ is an optional parameter allowing to consider generalized corner wave numbers γ/L and γ/W. The phase spectrum Φ is considered random at any wave number, except for circle $\gamma^2=(1/L)^2+(1/W)^2$ for which the phase is chosen to obtain the final slip concentrated in the centre of the fault.

where A_i is the amplitude of i-th Gaussian function centered in (x_i, y_i) and having width σ_i. In this analysis, we fix the position of all Gaussian functions and inverted only for their amplitude, so $p_i= A_i$. Realizing that the misfit Λ is a function of model parameters, we can write the Frèchet differential Λ as:

$$\Delta\Lambda = \iint \left(s_{ref}(x,y) - s_{gau}(x,y)\right)\Delta s_{gau}(x,y)dxdy \tag{3.13}$$

where

$$\Delta s_{gau}(x,y) = -\sum_{i=1}^{num\_par} \Delta A_i \, e^{-\frac{(x-x_i)^2+(y-y_i)^2}{\sigma_i^2}} \tag{3.14}$$

by substituing:

$$\Delta A_i = A_i \Delta \ln A_i \tag{3.15}$$

we introduce the constraint of positivity on the solution to obtain physically positive dislocation on the fault.

The equation (3.13) becomes

$$\Delta\Lambda = \iint \left(s_{ref}(x,y) - s_{gau}(x,y)\right)\sum A_i \Delta \ln A_i \, e^{\frac{(x-x_i)^2+(y-y_i)^2}{\sigma_i^2}} dxdy \tag{3.16}$$

Equation (3.16) can be finally written as

$$\Delta\Lambda = \sum_{i=1}^{num\_par} \iint \left(s_{ref}(x,y) - s_{gau}(x,y)\right) s_{i-\ gau}(x,y)\,dxdy\,\Delta\ln A_i \tag{3.17}$$

where

$$s_{i-\ gau}(x,y) = -A_i e^{-\frac{(x-x_i)^2+(y-y_i)^2}{\sigma_i^{\,2}}} \tag{3.18}$$

In order to obtain a simpler numerical implementation we rewrite the (3.17) as:

$$\Delta\Lambda = \sum_{i=1}^{num\_par} K_i \Delta\ln A_i \tag{3.19}$$

where A_i are the amplitudes of the Gaussian functions and K_i represents the corresponding gradient of the misfit function in the model-space parameter.

3.3.2. The projection of slip map onto Gaussian configuration: an example

To test of the methodology we generate the 'observed' slip map as a superposition of a Gaussian function with pre-established amplitude A_{obs}, and then we use, in the inversion, the same configuration for obtaining the synthetic slip map.

In figure 3-5, we show the 'observed' (a) and 'inverted' (b) maps. The two maps are identical and the normalized variance:

$$\mathrm{var} = \frac{\sum_{n=1}^{num\_par} \left| A_{obs} - A_{theo} \right|^2}{\sum_{n=1}^{num\_par} \left| A_{obs} \right|^2} \approx 10^{-6}$$

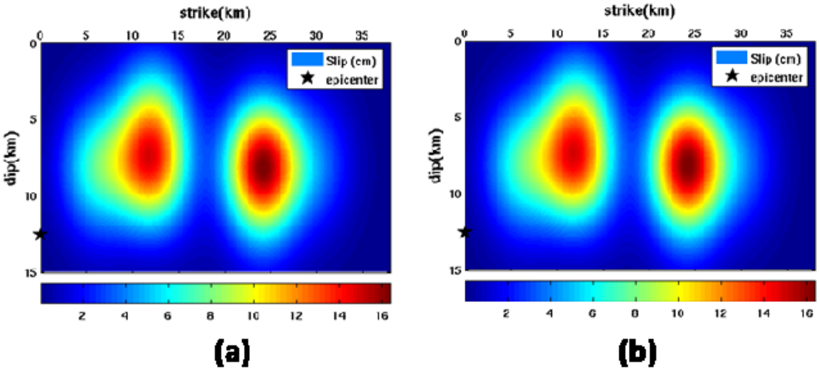

Figure 3-5: The figure (a) represents the 'observed' (a) map while the figure b represents the map obtained by the inversion whit the methodology discussed in the paragraph 3.3.1.

Although the problem is non linear (eq 3.15), our methodology converge at the best solution and we obtained the same input map.

We show a second example. As an input map we used a reference map (figure 3-6) according to the k-square models, and we performed several inversion, in terms of Gaussian amplitudes, for different Gaussian configurations (figure 3-7).

In each configuration the sample spacing along strike (ΔΦ) and dip (Δδ) direction, is the same (Δξ):

$$\Delta\Phi = \Delta\delta = \Delta\xi \qquad (3.20)$$

that corresponds to the condition:

$$\Delta\xi = \frac{L}{N_g^{\Phi} + 1} = \frac{W}{N_g^{\delta} + 1} \qquad (3.21)$$

Where (L, N_g^{Φ}) and (W, N_g^{δ}) are the dimension of the fault and the number of Gaussian along strike and dip directions, respectively.

The total number of Gaussian functions is:

$$N_g = N_g^{\Phi} \cdot N_g^{\delta} \qquad (3.22)$$

Moreover, the σ of the Gaussian function is related to the Δξ:

$$\sigma = \sqrt{\Delta\Phi^2 + \Delta\delta^2} = \sqrt{2}\Delta\xi \qquad (3.23)$$

As a convention, we define the number of Gaussian function configuration (Mod=Mod-01, Mod= Mod-02 etc, figure 3-7):

$$Mod = N_g^{\delta} \qquad (3.24)$$

So if Mod=Mod-01, it results $N_g^{\delta} = 1$ and one Gaussian function along the dip direction, if Mod=Mod-02 we have two Gaussian functions along the dip ect.

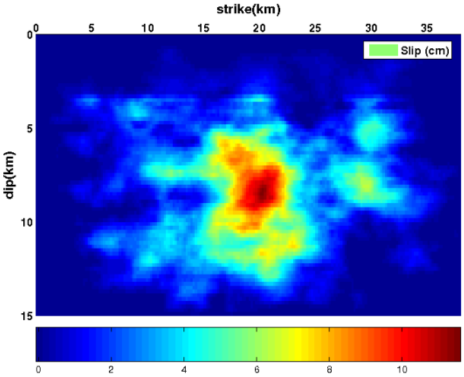

Figure 3-6: Reference map based on k-square model for a fault 35x15 km^2, along strike and dip respectively.

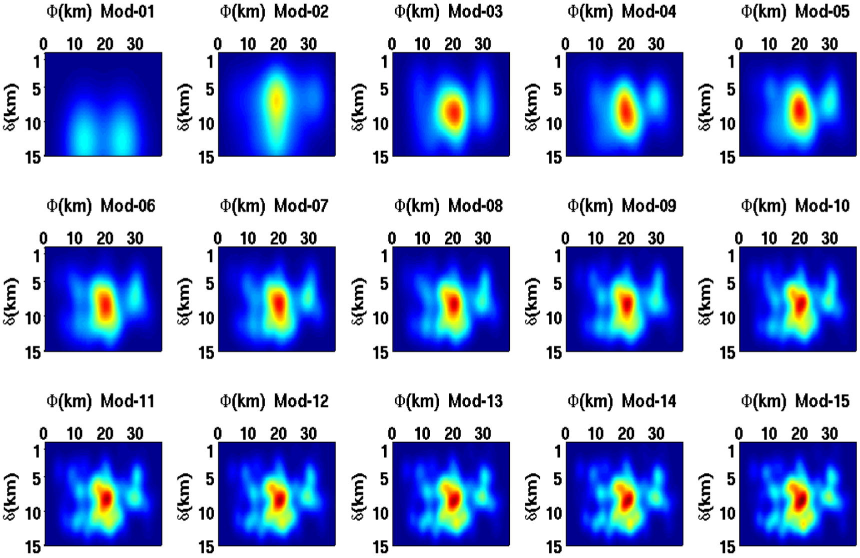

Figure 3-7: The figure shows the results of inversion for 15 different configurations of the Gaussian parameterization (Mod-01 to Mod-15). The configurations differ from each other for the Gaussian number that increases moving from the Mod-01 to the Mod-15. The fit is better for the configurations with larger number of Gaussian functions.

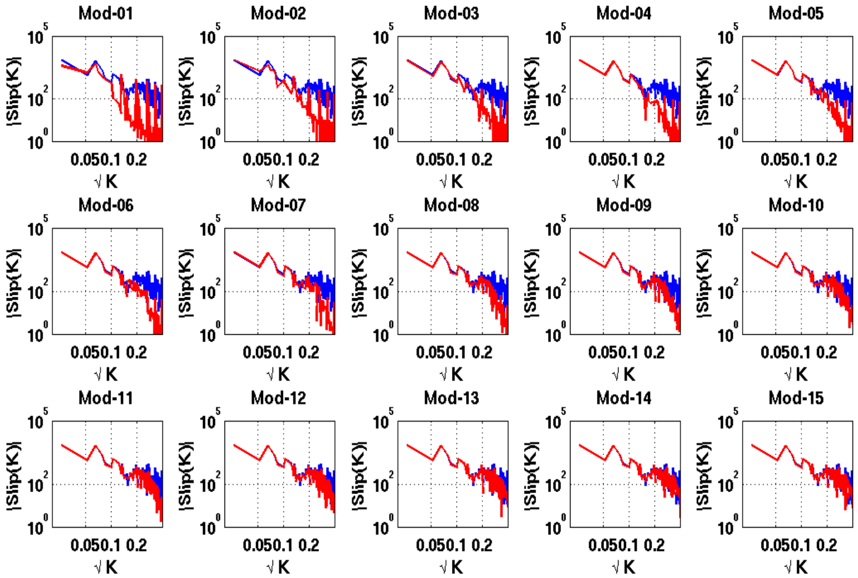

Figure 3-8: Spectra of k-square model are shown in blue, while the spectra of the Gaussian configuration are shown in red.

In figure 3-8, we can see the comparison between the spectra of k-square model (blue line) and the spectra of Gaussian configuration (red). The two trends are similar for low wavenumbers, and they become different at higher wavenumbers.

So we study the misfit

$$misfit = \sum_{i=1}^{\alpha} \frac{\left| \hat{S}_i^{obs} - \hat{S}_i^{theo} \right|}{\left| \hat{S}_i^{obs} \right|} \qquad (3.25)$$

in witch the S in the 2D Fourier Spectra of the slip map. For any value of sigma and overlapping, we select the maximum wavenumber for which the misfit function between the reference map and the correspondent Gaussian representation is smaller than a given tolerance. This maximum wavenumber is greater with increasing of number of Gaussian, N_g, in the configuration.

We repeated this analysis for different k-square models, configurations and overlapping values, which correspond to different values of σ (σ, $\sigma/2$, $\sigma/4$).

The results are show in the figure 3-9, in which we plot the σ value versus λ_{min}, minimum resolvable wavelength on the fault plane. The trend is linear in all three cases.

Now, we attempt to answerthe following question: "if we had a signal with maximum frequency f_{max}, how many Gaussian functions should we use in the inversion procedure?".

We should remember that there is a relationship between f_{max} and λ_{min}, the minimum wavelength, and now we have a relationship between λ_{min} and σ, this last linked to the number of Gaussian functions (figure 3-10).

The best choice is related to the compromise between the resolution on the fault plane and the burden of the inversion in terms of number of Gaussian functions. The Gaussian amplitudes will are parameters of the inversion. For example, if λ_{min}=4.5 km, the green curve wants a σ=0.5 km that corresponds to many Gaussian functions; while for the red curve σ=2 but the overlapping is great so we need many Gaussian functions. The best choice is the green line.

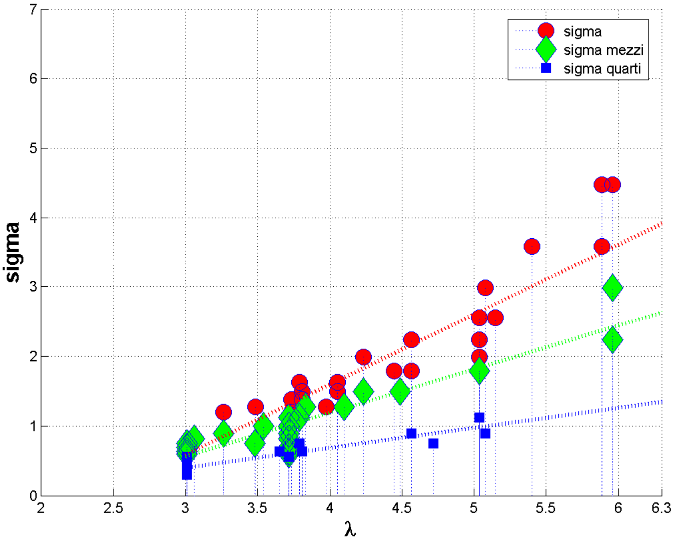

Figure 3-9: Relationship between σ and the minimum resolvable wavelength, in three case: σ (red-line), σ/2 (green-line), σ/4 (blue-line).

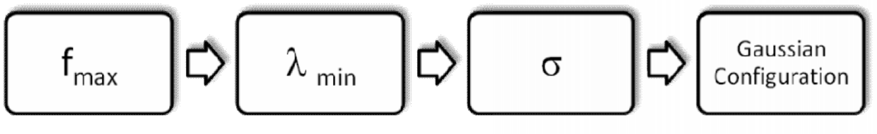

Figure 3-10: Flowchart of the relationship between the maximum signal frequency and the configuration of the Gaussian functions on the fault plane.

Chapter 4

Inversion Strategy: two steps procedure

4.1. Introduction

Inversion of seismic data for obtaining the distribution of the slip on finite fault has become a popular tool for the reconstruction of faulting processes during large earthquakes.

Historically, the first attempt to apply the representation theorem to the inversion for slip on finite faults was made by Trifunac (1974), who used five strong-motion records from the 1971 San Fernando, California, earthquake. The author used a full-space geometry and a simple trial-and-error approach to fit the available data-set.

The first study, in which the problem of the slip determination was considered on the formal basis of the linear inverse theory, was published by *Olson* and *Apsel* (1982). The theory was based on a matrix version of the representation integral and two methods of solution of the inversion problem were presented: the least-square method, which minimizes the squared differences between simulated and observed data, and the constrained least-squares method, which simultaneously includes a set of linear inequalities.

Thanks to contemporary computational tools, most seismologists are facing the finite-fault inversion in its full non-linear formulation, rather than in a linearized form. The global optimization techniques have the ability to escape local minima of the cost function in the parameter space and to converge to the optimal model.

4.2. The misfit function

The choice of the cost function to be used in the inversion procedure is a crucial point. This aspect of the finite-fault inversion problem, and its implications on the resulting source model, were studied by *Hartzell* (1991) who performed a quantitative comparison between L_1 and L_2 norms.

The L_2-norm minimizes the sum of squares of the differences between the real and synthetic data. This norm assumes that the errors in the data have a Gaussian distribution.

The L_1-norm minimizes the sum of the absolute value of the difference between the data and synthetics data. For this norm, the errors in the data have a exponential distribution (*Menke,* 1984). An exponential distribution with the same mean and variance as a Gaussian distribution has a much longer tail, so the probability of having a few outlying points is much higher. In conclusion the L_1

minimisation is able to handle a few bad data points then assigning then lower weights.

Where good data-sets are available, in case of a large earthquake, it is preferable to use the L₂-norm.

$$misfit\,(t) = \sum_{i=1}^{Ns} \sum_{k=1}^{Nc} \sum_{m=1}^{Nt} \left| u_{i,k,m}^{Synth} - u_{i,k,m}^{Obs} \right|^2 \qquad (4.1)$$

In this form, the misfit function includes the contribution of the stations (N_s: number of the stations), of the ground motion components (N_c=3, east, north, vertical), and all samples in the time domain (N_t).

Since in the approach described in the chapter 1 the forward problem is solved in frequency domain, recorded and synthetic seismograms are compared in this domain. Using the Parseval's theorem[15], the final formula for the misfit used in our methodology is:

$$misfit\,(\omega) = \sum_{i=1}^{Ns} \sum_{k=1}^{Nc} \sum_{m=1}^{N\omega} \left| \tilde{u}_{i,k,m}^{Synth} - \tilde{u}_{i,k,m}^{Obs} \right|^2 \qquad (4.2)$$

here N_ω is the number of frequencies.

Generally, the orders of magnitude are:

---

[15] **Parseval's Theorem**: Parseval's theorem is written as: $\int_{-\infty}^{+\infty} |x(t)|^2\, dt = \int_{-\infty}^{+\infty} |X(f)|^2\, df$, where X(f) represents the continuous transform of x(t). This means that the total energy contained in a waveform x(t) summed along time t is equal to the total energy of the waveform's Fourier transform X(f) along its frequency components f.

$$\begin{aligned} N_t &\approx 10^3 \\ N_\omega &\approx 10 \end{aligned} \qquad (4.3)$$

Hence the algorithm is faster in frequency domain than in the time domain.

4.3. The two-steps procedure

The ground motion recorded at a seismic station non linearly depends on the kinematic rupture history, in terms of slip and rupture velocity. However, for fixed rupture velocity, the representation integral is linear with respect to the slip and if the rupture velocity were known, slip could be retrieved by a regularized linear inversion of strong-motion data. Although the rupture velocity is unlikely to be known a-priori, we can still take advantage from the linearity by separating the inverse problem into two nested problems. Let us assume $\mathbf{V}_r$ and $[\mathbf{U}]$ a rupture velocity and slip parameterizations respectively. The forward problem of eq. 1.14 with 2.16, can be simplified to

$$\mathbf{u} = K(\mathbf{V}_r, [\mathbf{U}]) \qquad (4.4)$$

where also $\mathbf{u}$ is the discrete representation of the displacement. The operator K accounts for the product by the Green's tractions and integration on the fault plane. It is non linear because the rupture velocity influences the phase shift related to the delay required by the rupture to go from the hypocenter to each point of the fault. Instead the operator $K(\mathbf{V}_r = \mathbf{V}_r^0;[\mathbf{U}])$ is linear with respect to the slip. As a misfit criterion, we chose to minimize the square L^2 norm

$$\left\| \mathbf{u} - K(\mathbf{V}_r,[\mathbf{U}]) \right\|^2 \qquad (4.5)$$

The inverse problem is solved by a two step procedure aimed at separating the computation of the rupture velocity, which is intrinsically a non linear problem, from the evaluation of the slip distribution, a linear problem, when the rupture velocity is fixed (figure 4-1).

During the first step, we fix a v_r map (for example at constant value), and the linear problem is solve with a Non Negative Least Square algorithm. For the slip map retrieved, we solved the non-linear problem to search the v_r map, using the global search, Neighbourhood algorithm, which minimizes the misfit function. Then we re-fix the v_r map to the distribution obtained on correspondence of a minimum and the procedure is restarted. The procedure stops when the misfit value is below a given threshold.

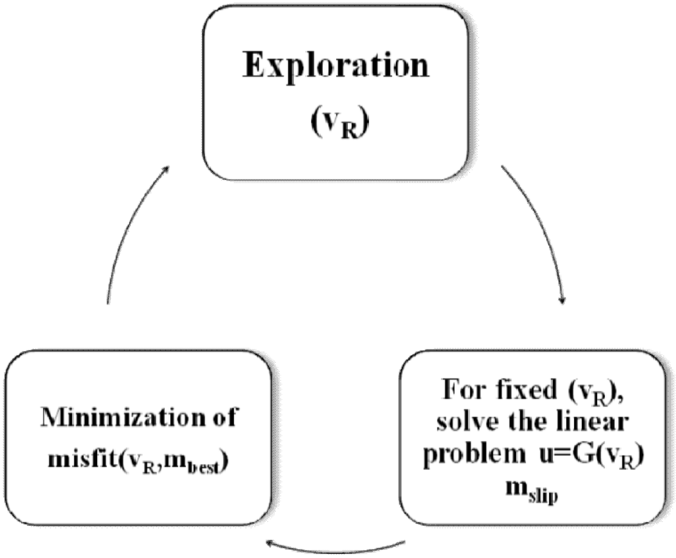

Figure 4-1: Flowchart of the two-steps procedure to inversion.

4.3.1. Non negative least square solution

We use the Lawson-Heaton (*Lawson* and *Heaton*, 1974; 1995) algorithm for non-negative least square solution[16] (NNLS) to determine the amplitudes Gaussian. Such an algorithm automatically constrain the slip to be non-negative.

We can rewrite the representation problem in matrix formulation:

---

[16] **Non negative least square solution**: The NNLS solves the least square problem $\min \|Ax = b\|_2$ with the constraint $x \geq 0$.

$$\mathbf{u}^{\mathbf{synth}} = \mathbf{G}(\mathbf{v}_{\mathbf{r}})\mathbf{m}_{\mathbf{A}} \tag{4.6}$$

where **m** is the vector of Gaussian amplitudes and **G**(v_r) is the operator that accounts for the product by Green's traction and integration on the fault plane, for a fixed v_r. In other words, we want to solve the problem:

$$\min \left\| \mathbf{u}^{\mathbf{obs}} - \mathbf{G}(\mathbf{v}_{\mathbf{r}})\mathbf{m}_{\mathbf{A}} \right\|^2 \tag{4.7}$$

where $\mathbf{u}^{obs}$ is the vector of real data. Since the forward modeling is fast for computing waveform spectra, records and seismograms are compared in the frequency domain, using both real and imaginary parts of the signal's spectra.

4.3.2. The Neighbourhood algorithm

The non-linear step uses the neighbourhood algorithm (*NA*, *Sambridge*, 1999; 2001), a non-linear derivative-free technique employing simple geometrical concepts to guide a direct search in the parameter space. At each stage, the entire parameter space is partitioned into a set of Voronoi cells (nearest neighbour regions, as defined by a suitable norm), one associated with each previously sampled model. A Voronoi cells of a particular model is a polygon whose interior consists of all points in the parameter space which are closer to this particular model than to any other model. Between consecutive iterations, the new sample is recalculated in only the Voronoi cells of the previous models having the smallest misfit, becoming thus less computationally expensive than, for example, the Montecarlo technique[17]. The NA uses only two control parameters (the sample size at each iteration n_s , and the number of cells n_r in which a new samples is searched), as compared to the genetic algorithm [18] and simulated annealing[19].

To summarize the whole inversion technique: at the first iteration, a random set of the models is generated (n_s) and the forward simulation is run for each of these models. At the second iteration, n_s new models are pseudo-randomly generated in n_r Voronoi cells corresponding to the n_r previous best models with the lowest misfit (figure 4-2).

---

[17] **Montecarlo technique**: Monte Carlo methods provide approximate solutions to a variety of mathematical problems by performing statistical sampling experiments. They can be loosely defined as statistical simulation methods, where statistical simulation is defined in quite general terms to be any method that utilizes sequences of random numbers to perform simulation. Thus Monte Carlo methods are a collection of different methods that all basically perform the same process. This process involves performing many simulations using random numbers and probability to get an approximation of the answer to the problem. The defining characteristic of Monte Carlo methods is its use of random numbers in its simulations.

[18] **Genetic algorithm**: Genetic algorithms were formally introduced in the United States in the 1970s by John Holland at University of Michigan. To use a genetic algorithm, you must represent a solution to your problem as a *genome* (or *chromosome*). The genetic algorithm then creates a population of solutions and applies genetic operators such as mutation and crossover to evolve the solutions in order to find the best one(s).

[19] **Simulated annealing**: It is a probabilistic method for finding the global minimum of a coast function that may have several local minima. It works by emulating the physical process whereby a solid is slowly cooled so that when eventually its structure is “frozen”, this happens at a minimum energy configuration.

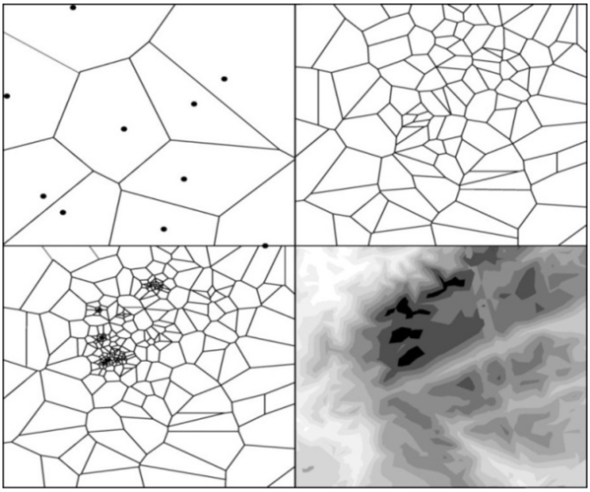

Figure 4-2: The figure shows the result for two parameters problem. The upper-left panel shows 10 samples and the corresponds Voronoi cells; the upper-right panel shows 100 samples. The lower-left panel similar to upper-right panel but with 10000 samples. Here the algorithm concentrates on four distinct region corresponding to the minimum of the misfit. The lower-right panel shows the contours of the misfit function in grey scale.

Chapter 5

Application of inverse technique to the Iwate-Miyagi-Nairiku earthquake

5.1. Case study

The our methodology was applied to the Iwate-Miyagi Nairiku earthquake. It was a M_{JMA}[20]=7.2 (M=6.9, Global CMT[21]) inverse-fault [22]earthquake that occurred in the eastern side of the Ou mountain range, northeast Honshu Island, Japan, on June 14, 2008, at 8:43 Japanese standard time. The aftershock distribution derived by the National Research Institute for the earth Science and Disaster Prevention using mainly Hi-net data, (High sensitivity seismograph network Japan; *Obara et al., 2005*), indicated that the source area of the earthquake extended bilaterally from the hypocenter to the north-northeast (NNE) and to south-southwest (SSE) directions near the border between Iwate and Miyagi prefectures. The hypocenter is located at the 39.027N, 140.78E, at the depth of 8.0 km. The location was obtained by Shiomi et al.

---

[20] **M_{JMA}**: Magnitude provided by Japan Meteorological Agency

[21] **Global CMT**: Global Centroid-Moment-Tensor.

[22] **Inverse fault**: This kind of fault is originated typically by compressive forces and it can be also called a thrust fault. It is a dip-slip fault with rake angle equal to 90° (the hanging wall moves upward).

(2009) using the double-differences method (*Waldhauser and Ellsworth, 2000*).

We assumed a planar fault model that extends 40 km in strike (N207°E) direction and 20 km in the dip (37°) direction (figure 5-1).

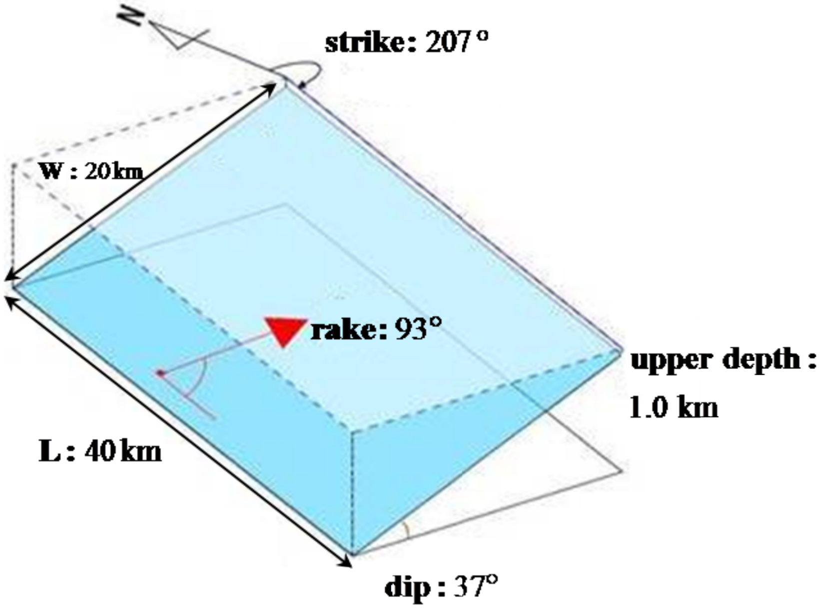

Figure 5-1: Fault-plane geometry and focal mechanism.

The earthquake was recorded by the two nationwide strong-motion networks, K-net[23] and Kik-net[24] (*Kinoshita, 1998*; *Aoi et al., 2004*), which provided a dense distribution of data around the source (*Olson et al., 1988*). We used three-component velocity

---

[23] **K-net:** Kyoshin Net (k-net), http://www.k-net.bosai.go.jp/.

[24] **Kik-net**: http://www.kik.bosai.go.jp/.

records at eleven near-source stations having epicentral distances ranging from 12km to 50 km, as shown in figure 5-2. Stations names and coordinates are listed in table 5-1.

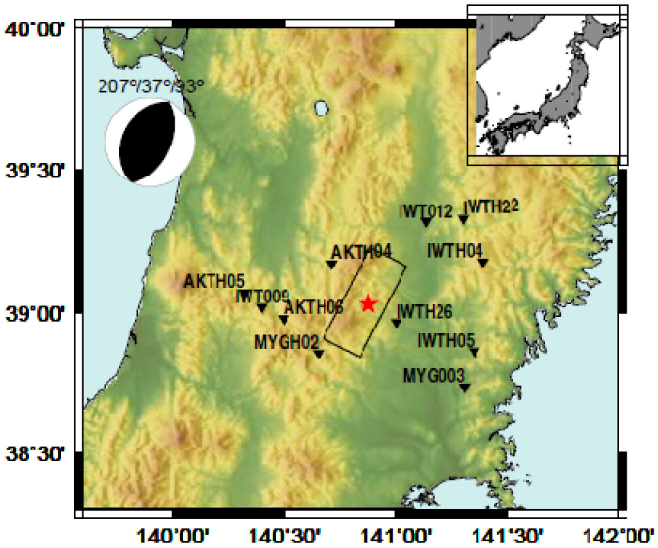

Figure 5-2: Distribution of the strong motion stations (triangles) and fault plane model (rectangle) used for the inversion. The red star indicates the epicenter. The moment tensor solution is shown at upper-left of the figure.

Name	Lat. (°)	Long. (°)	Dist. (km)
AKTH04	39.17	140.72	21.70
AKTH05	39.07	140.32	48.82
AKTH05	38.98	140.50	33.70
IWT009	39.02	141.40	45.31
IWT012	39.32	141.14	39.42
IWTH04	39.18	141.39	47.39
IWTH050	38.86	141.35	44.69
IWTH22	39.33	141.30	49.84
IWTH26	38.97	141.00	12.40
MYG003	38.73	141.31	49.55
MYGH02	38.85	140.65	27.29

Table 5-1: Names, coordinated (latitude and longitude), and distance from epicenter of the stations used in inversion.

We assumed the same vertically layered velocity structure model for each station in order to calculate the Green's tractions (table 4-2).

d (km)	α (km/s)	β (km/s)	ρ (g/cm^3)
0.0	5.5	3.2	2.6
1.9	6.0	3.5	2.7
16.0	6.6	3.8	2.8
38.0	8.0	4.6	2.9

Table 5-2: 1D velocity structure model used to calculate Green's function. d is the depth of the upper interface, α and β are P and S velocities of wave respectively and ρ is density of the medium.

5.2. The synthetic test: Gaussian amplitude inversion.

In order to validate the inverse methodology, we present a synthetic test: we generated and inverted a set of synthetic data associated at a hypothetical earthquake whit all known characteristics.

The hypothetical earthquake has the same characteristics of the Iwate earthquake: fault dimension 40 x20 km^2, strike 207°, dip 37°, rake 93°. We generated a synthetic data-set for all station listed in table 5.1 and from 0.05 to 0.5 Hz, and with three different noise level: noiseless, 10% and 30% of the signal. For the dislocation, we generated the seismograms for two different maps: the first (case A) with one circular anomaly and the second (case B) whit three circular anomaly. We assumed the rupture velocity constant on fault plane (equal to 3 km/s) and we inverted for the Gaussian amplitude (N_g=36).

5.2.1. Case A: one circular anomaly

The slip distribution for case A is shown in figure 5-3, it consists of a uniform final dislocation (slip equal to 2 cm) with one circular anomaly with radius 5 km and slip equal to 30 cm.

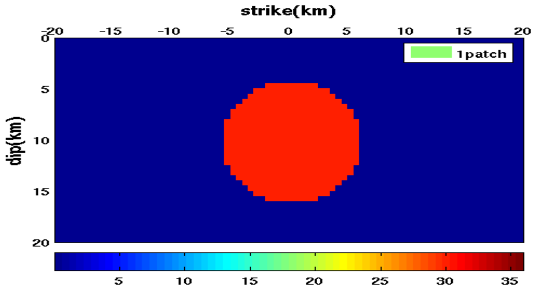

Figure 5-3: Slip distribution with one patch used for the synthetic seismograms generation.

In figures 5-4, 5-5, 5-6 are shown the slip map inverted form the three studied cases: no noise, 10 and 30 % respectively. The comparison between “real” and theoretical data are shown in the figure 5-7, 5-8, 5-9. In table 5-3 we summarize the results of the inversion in terms of best value misfit and slip max.

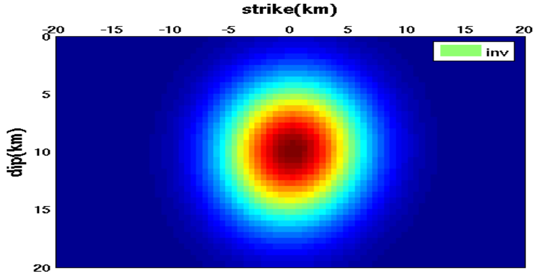

Figure 5-4: Slip maps inverted in the no noise case.

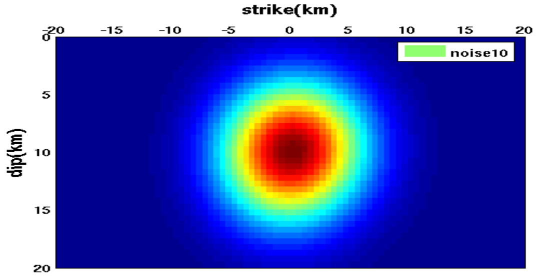

Figure 5-5: Slip map inverted with "real" data contaminated with 10 % of noise.

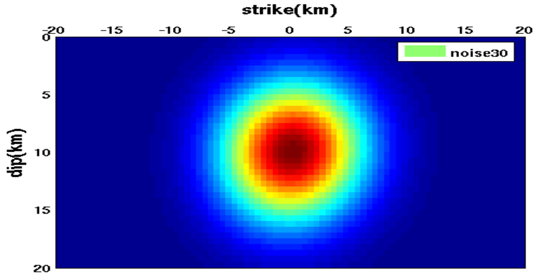

Figure 5-6: Slip map inverted with "real" data contaminated with 30 % of noise.

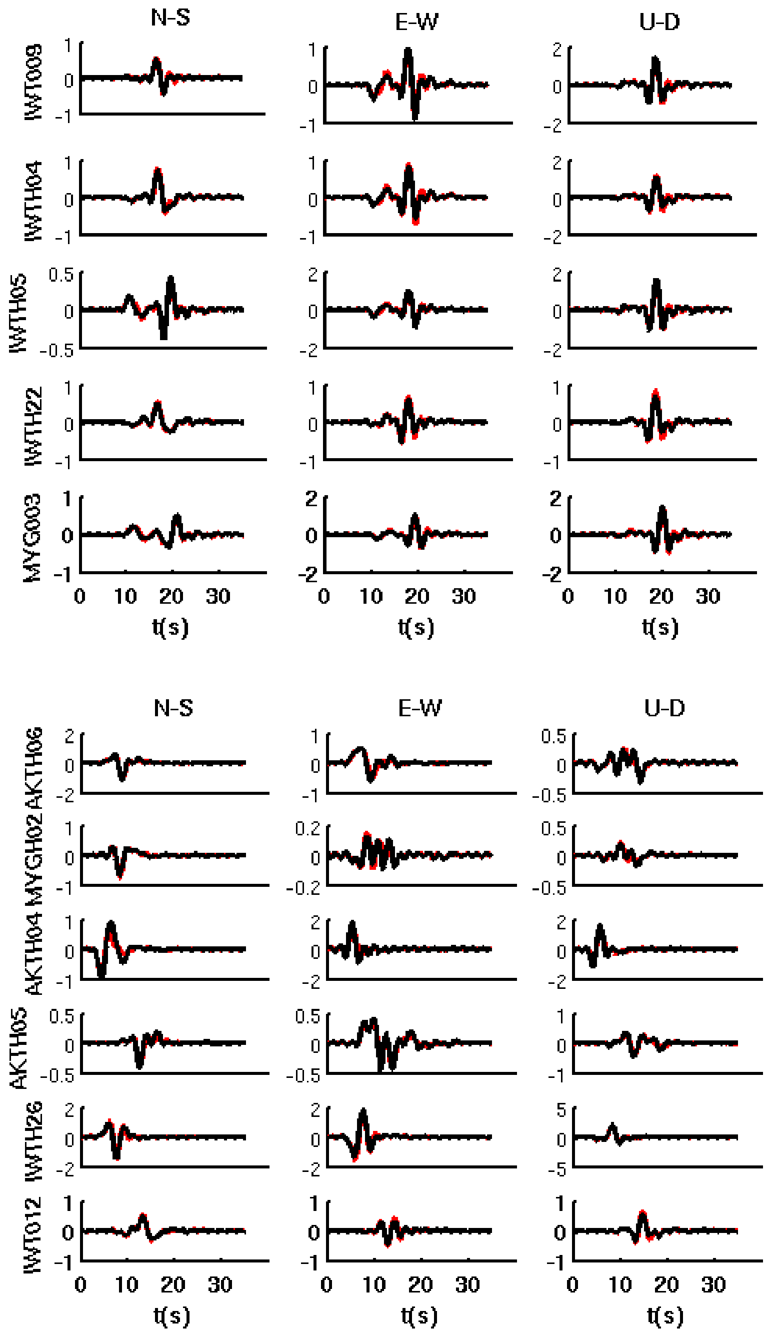

Figure 5-7: Comparison between “real” with no noise (black) and synthetic (red) data.

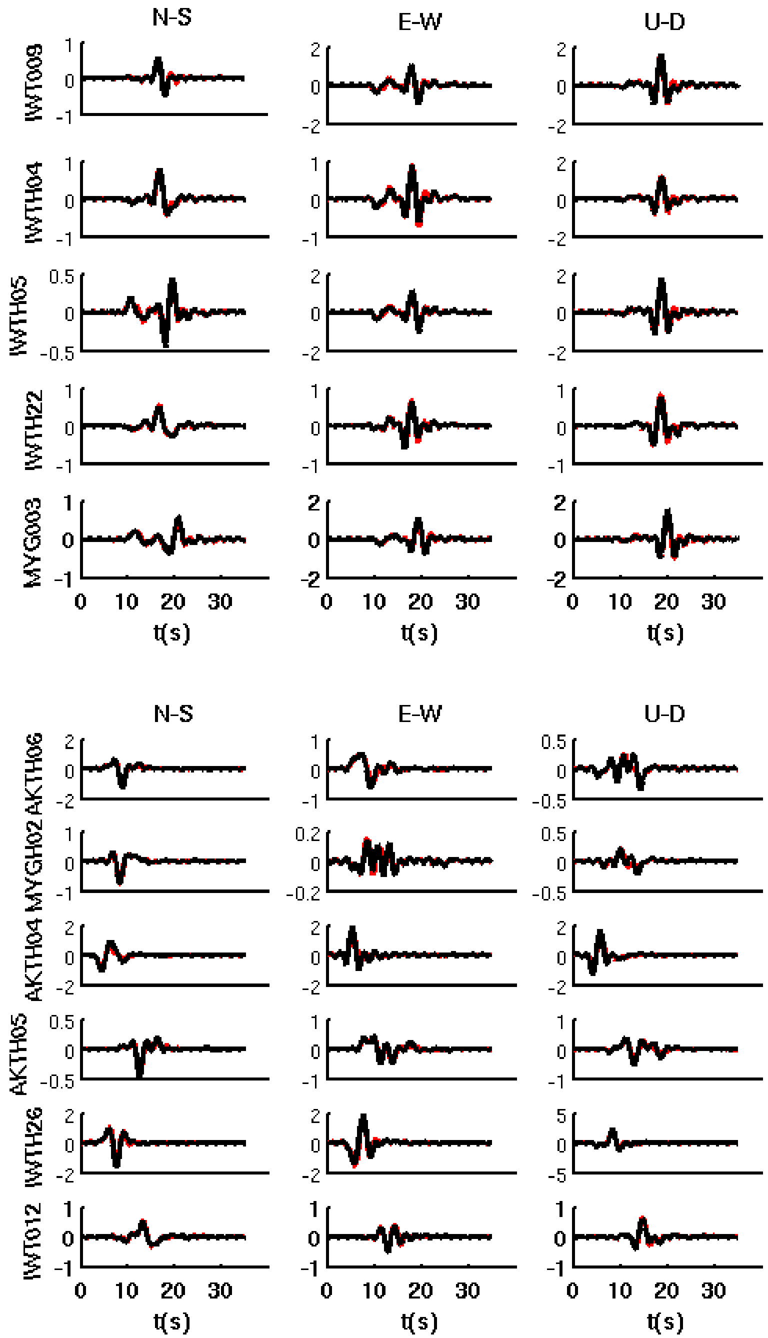

Figure 5-8: Comparison between “real” with 10 % noise (black) and synthetic (red) data.

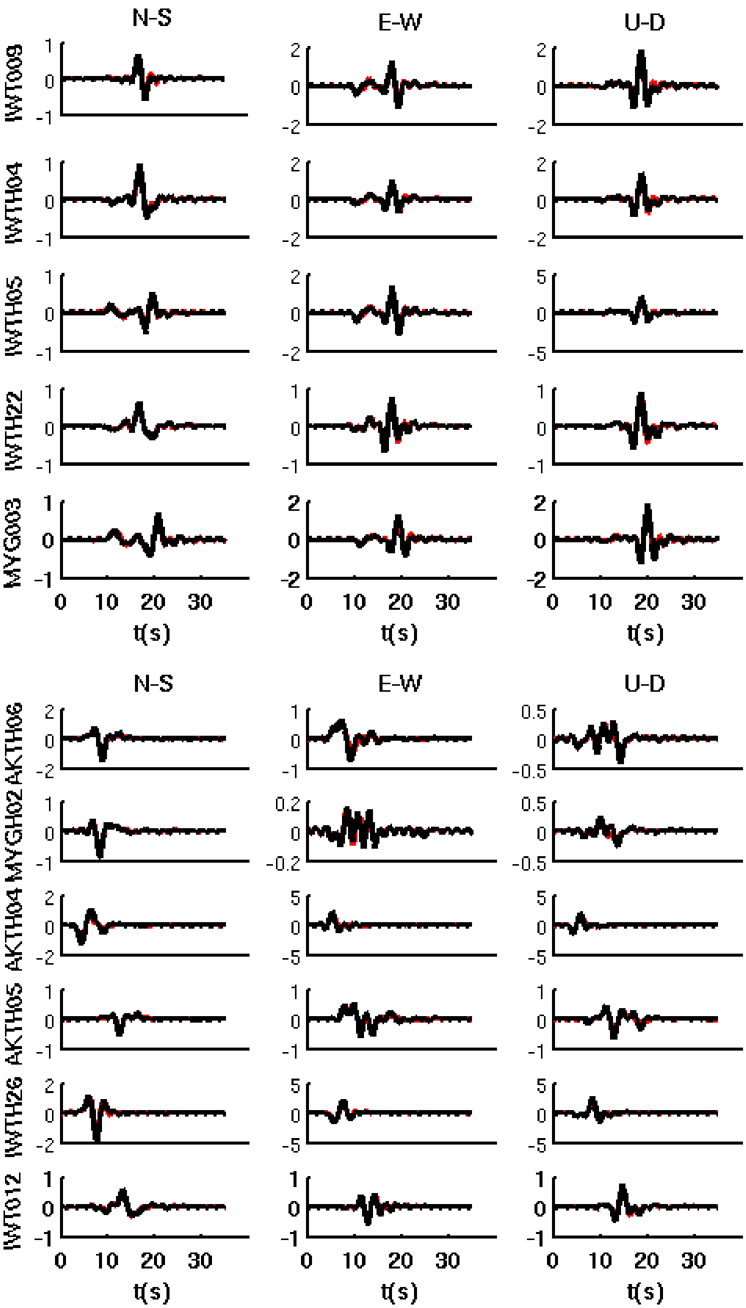

Figure 5-9: Comparison between "real" with 30 % noise (black) and synthetic (red) data.

Noise (%)	Best misfit (cm)	Slip max (cm)
none	8.22	35.9
10	8.24	35.98
30	8.31	36.10

Table 5-3: Summary of the results of the inversion – Case A.

In all three cases, the largest slip patch is well resolved in terms of position and dimension. The maximum slip value is overestimated of 0.9 cm for the case with no noise data and of 1.1 cm in the case of noise equal to 30%. Generally the results of inversion are sufficiently accurate.

In order to analyze in detail a comparison between “real” and inverted data we show the time frequency envelope misfit (TFEM) and the time frequency phase misfit (TFPM) spectrogram (figures 5-10, 5-11, 5-12) for the station MYGH02.

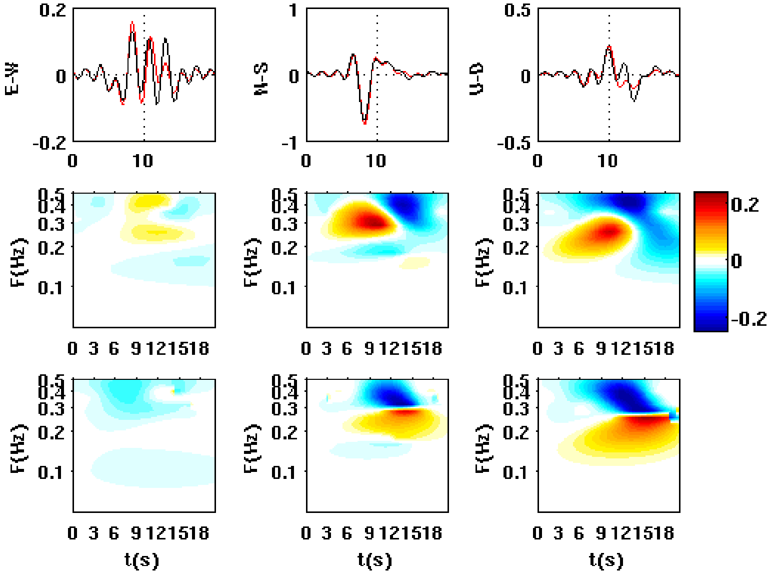

Figure 5-10: Spectrogram for the station MYGH02, whit no –noise "real" data. Red color in the TFEM and the TFPM images indicates a greater amplitude and a positive phase shift. Blue color represents the opposite case.

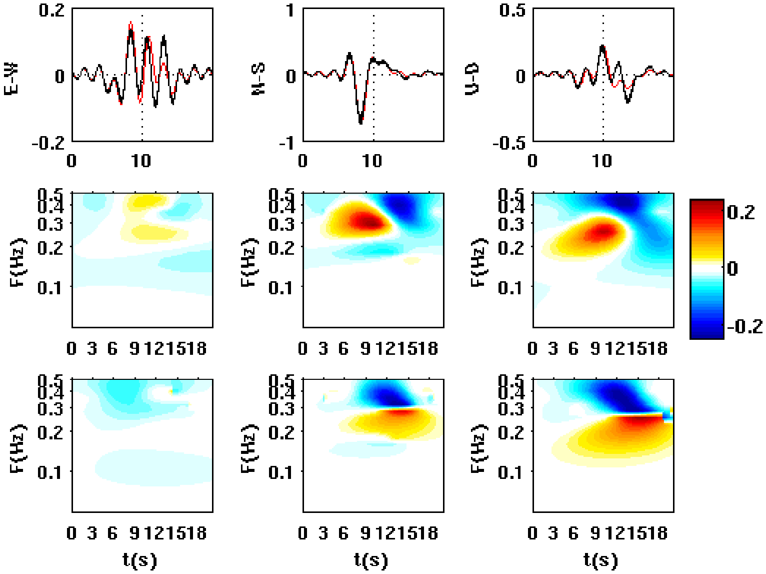

Figure 5-11: Spectrogram for the station MYGH02, whit 10% of noise.

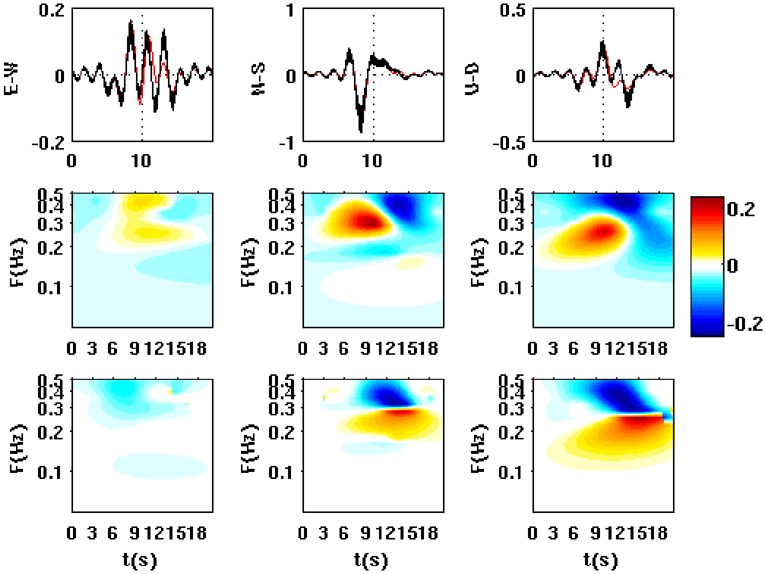

Figure 5-12: Spectrogram for the station MYGH02, whit 30% of noise.

The phase shift is the same for the three cases; as for the amplitude, some differences are evident. In all time duration the variation are the same in the three cases but in frequency at low frequency (from 0.05 to 0.2 Hz) a change can be noticed, and in generally the amplitude is underestimated.

5.2.2. Case B: three circular anomaly

The slip distribution for the case B is shown in figure 5-13. It consists of a uniform final dislocation (slip equal to 2 cm) with three circular anomalies: the orange, azure and blue have 50 cm, 30cm, 5 cm slip maximum and radius 7cm, 5cm, 3cm respectively.

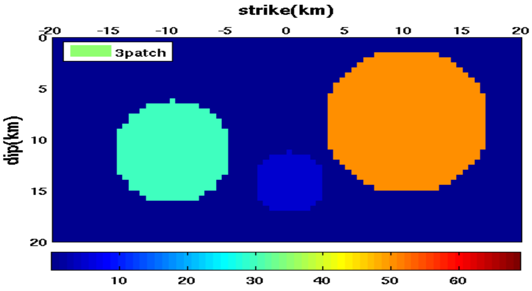

Figure 5-13: Slip distribution with three patch use for the synthetic seismograms generation.

In figures 5-14, 5-15, 5-16 are shown the slip map inverted form the three case of study. The comparison between "real" and theoretical data are shown in figures 5-17, 5-18, 5-19. In table 5-4 we summarize the results of the inversion in terms of best value misfit and slip max.

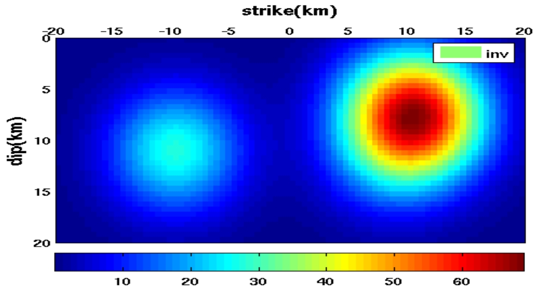

Figure 5-14: Slip map inverted in the no noise case.

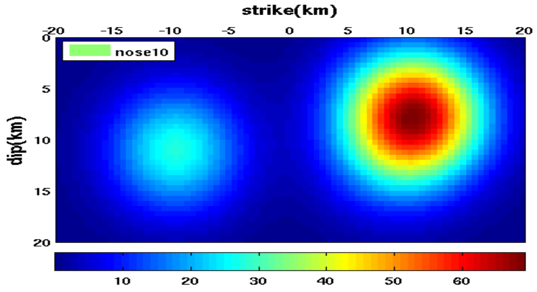

Figure 5-15: Slip map inverted with "real" data contaminated with 10 % of noise.

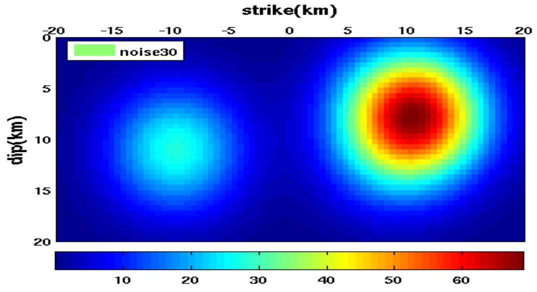

Figure 5-16: Slip map inverted with "real" data contaminated with 30 % of noise.

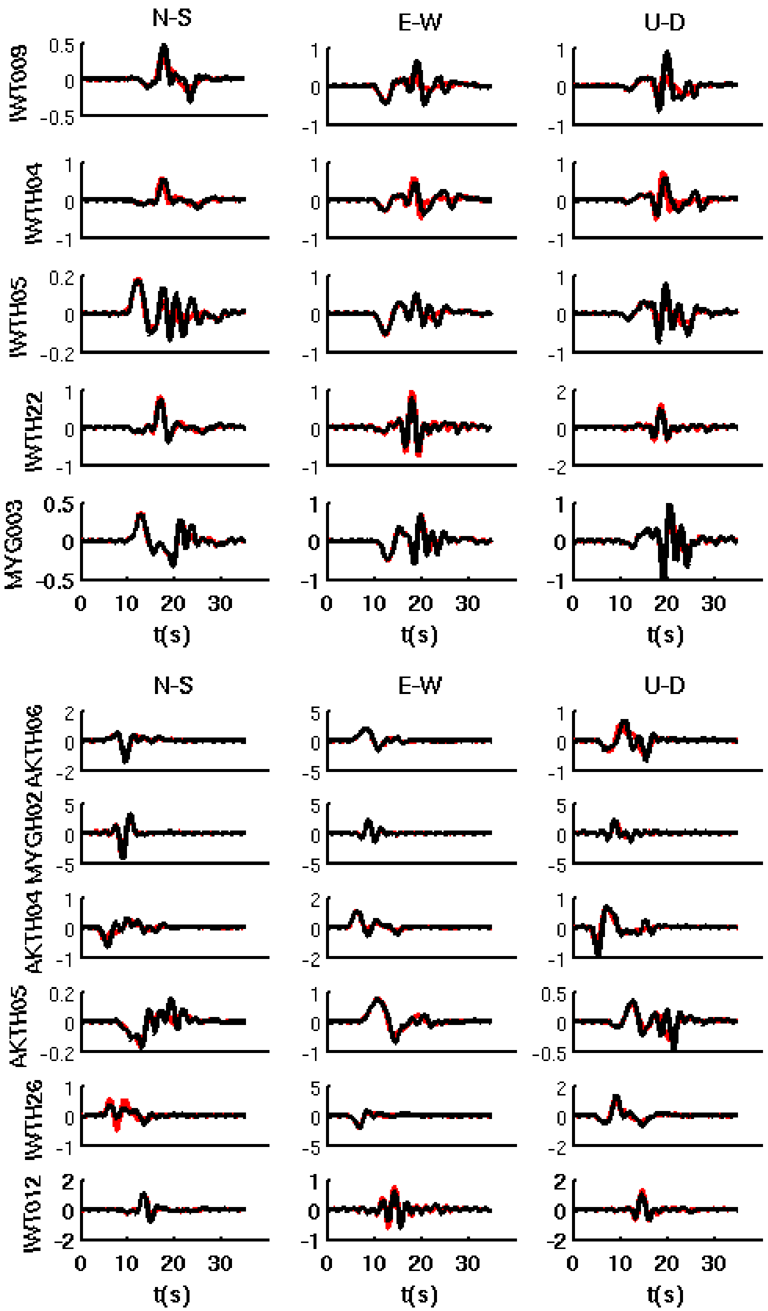

Figure 5-17: Comparison between “real” with no noise (black) and synthetic (red) data.

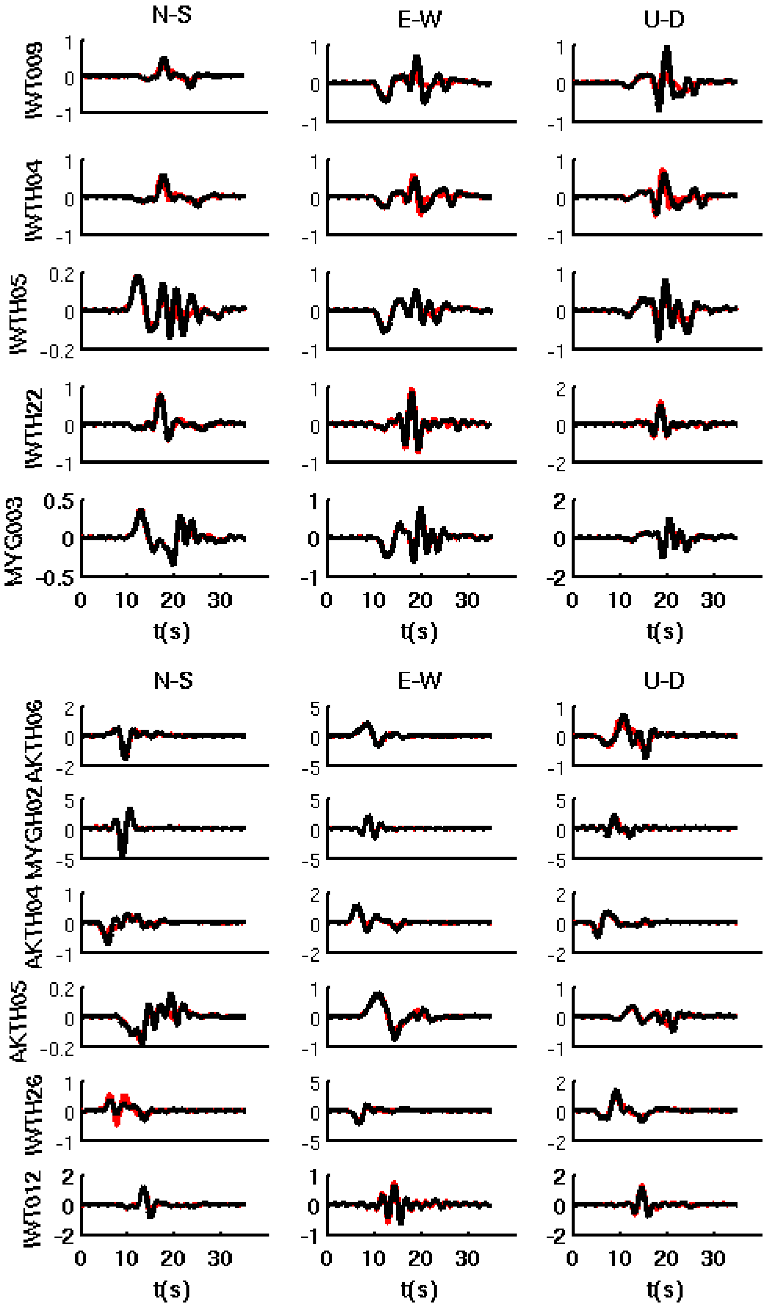

Figure 5-18: Comparison between “real” with 10 % noise (black) and synthetic (red) data.

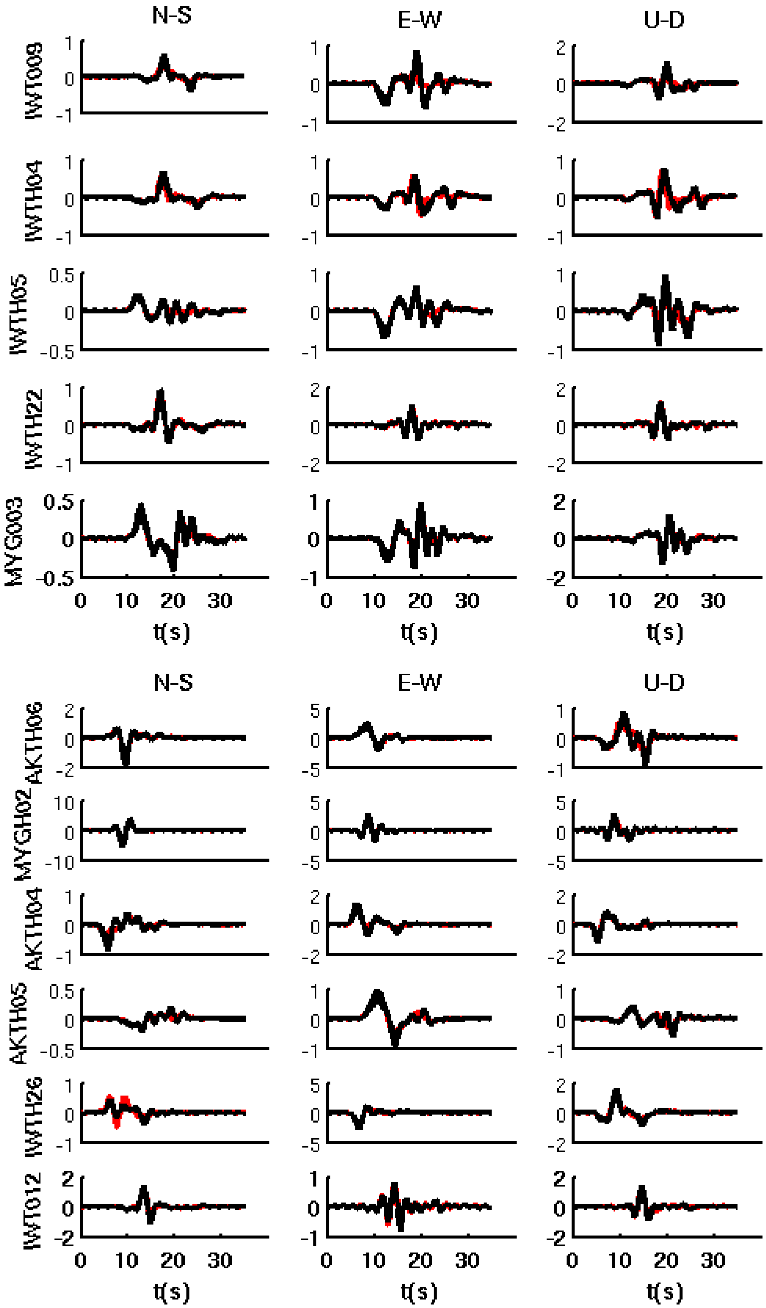

Figure 5-19: Comparison between "real" with 30 % noise (black) and synthetic (red) data.

Noise (%)	Best misfit (cm)	Slip max (cm)
none	13.01	69.19
10	13.04	69.16
30	13.14	69.09

Table 5-4: Summary of the results of the inversion - Case B.

In all three cases, the two largest slip patches are well resolved in terms of position and dimension, while the smallest patch is not identified. Therefore, the maximum slip value is overestimated of around 10 cm for the three cases. Generally the results of inversion are sufficiently accurate.

Even for the case B, we show the TFEM and the TFPM, spectrogram for the station MYGH02.

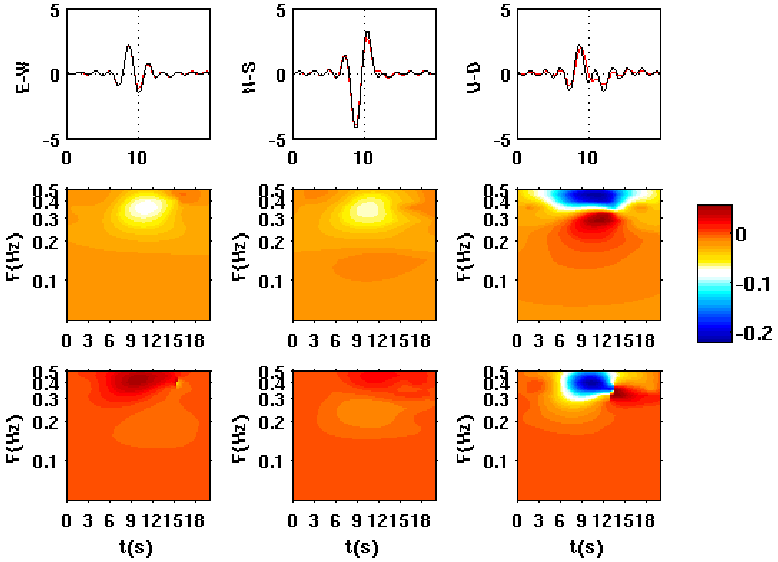

Figure 5-20: TFEM and the TFPM for the station MYGH02, in the no-noise real "data".

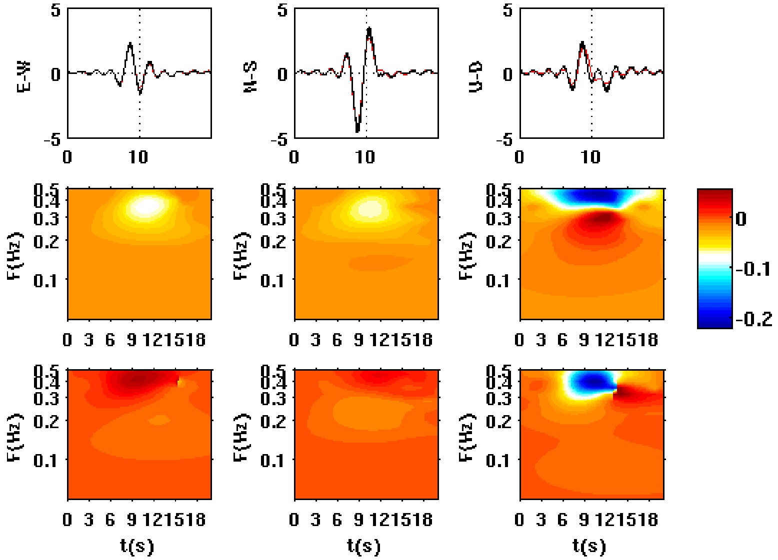

Figure 5-21: TFEM and the TFPM for the station MYGH02, with 10% of noise in the “real” data.

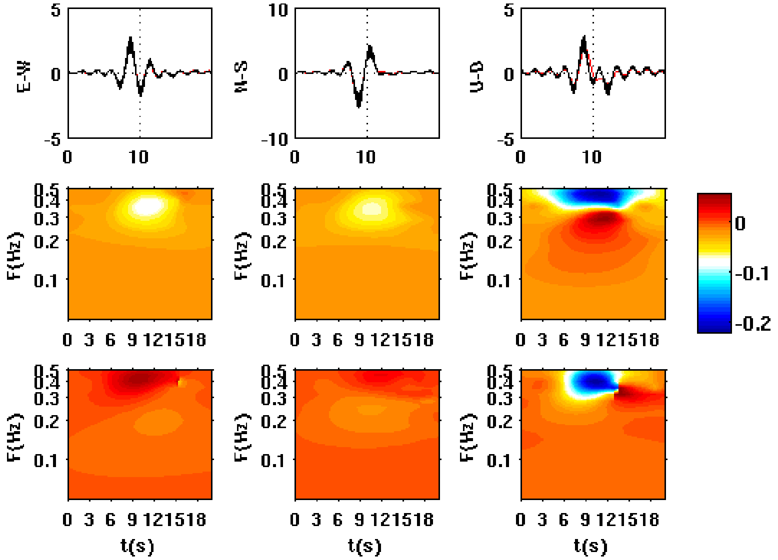

Figure 5-22: TFEM and the TFPM for the station MYGH02, with 30% of noise in the “real” data.

There are differences in phase an amplitude in the three cases, and the U-D component is underestimated.

5.3. The synthetic test: two steps procedure.

In order to validate the two steps procedure, we generated a set of free-noise synthetic data with the slip map in figure 5-13, and a rupture velocity map variable on a fault plane and mean value 1.98 km/s. Figure 5-23 shows the slip and rupture time map.

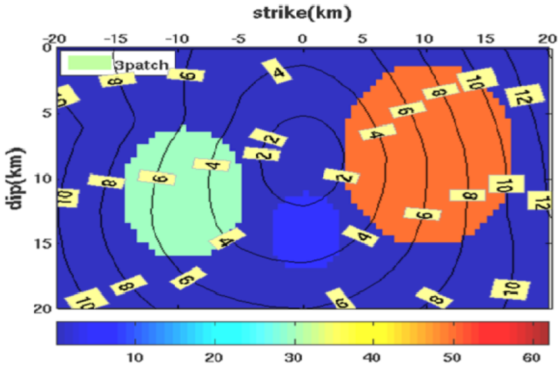

Figure 5-23: Slip and rupture time map.

We inverted the eleven seismograms, and used 36 gaussian functions; for the rupture velocity we use 4x4 control point grid, and we limit the variation range between 1.5 km/s and 3.5 km/s.

In figure 5-24 we show a comparison between forward (red) and inverted (black) velocigrams, while in figure 5-25 we show the TFEM and the TFPM, spectrogram for the station MYGH02.

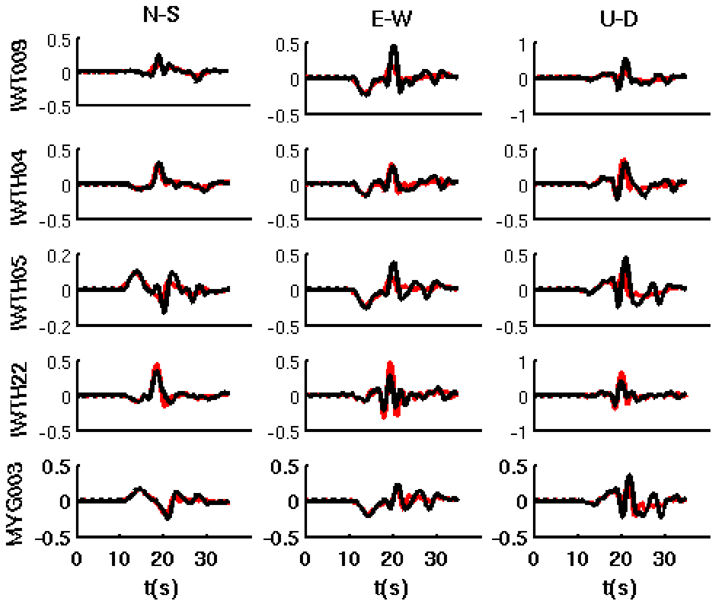

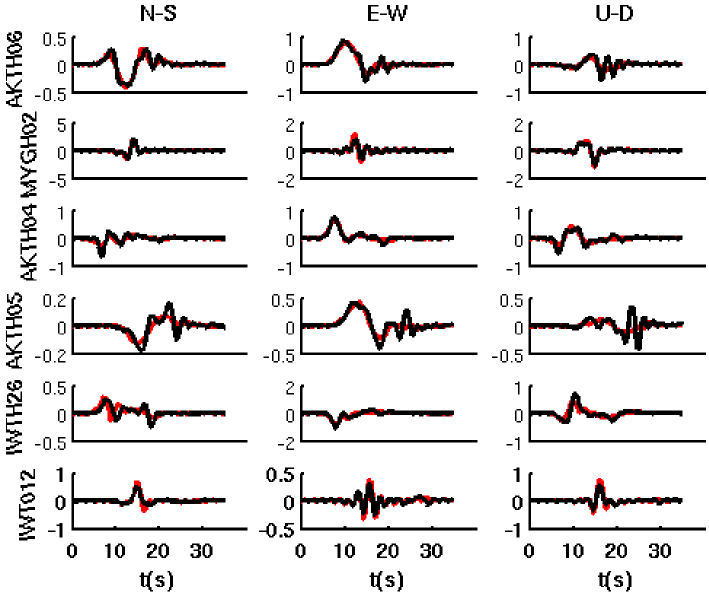

Figure 5-24: Comparison between “real” (black) and synthetic (red) data.

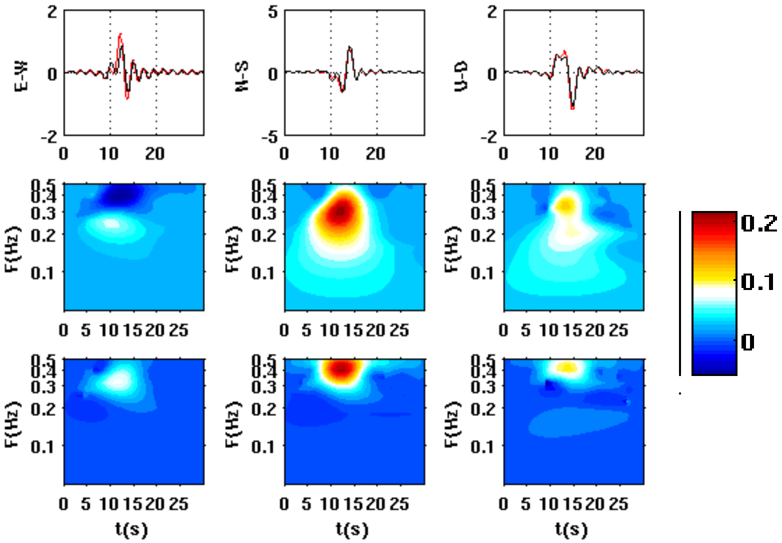

Figure 5-25: TFEM and the TFPM for the station MYGH02. Red color in the TFEM and the TFPM images indicates a greater amplitude and a positive phase shift in the "inverted" seismograms with respect to "real" seismograms. Blue color represents the opposite case.

The slip and rupture map inverted are show in figure 5-26.

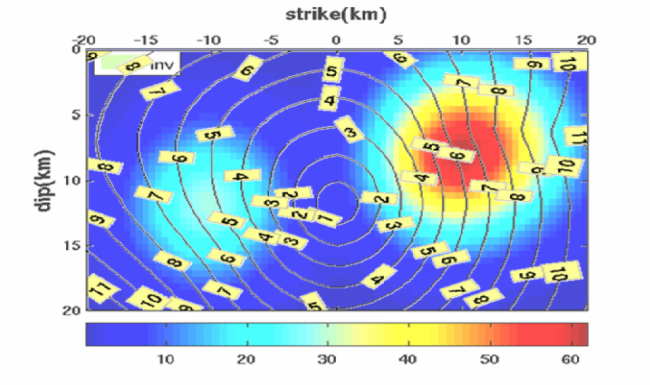

Figure 5-26: Slip and rupture time: results of the inversion.

In this test for the inversion , we are able to resolved the patch with larger slip, but we can not obtain the slip with slip equal to 5 cm. The rupture velocity estimated is 2.3 km/s; it is greater than 1.98 km/s so the inverted seismograms have a positive value for TFPM (red in the color scale in figure 5-26).

5.4. The synthetic test: Conclusion

We performed two synthetic tests: one considering rupture velocity constant and inverting only the slip and another with slip and rupture velocity as parameters of the inversion. The first aims at testing the linear step and the second at validating the complete procedure. The results are good in terms of map and rupture time. So we have built a procedure that works and can be apply to the real.

5.5. Real data inversion

After the synthetic test, we applied the methodology at the real data-set of the Iwate -Miyagi Nairiku earthquake, with the aim of obtaining the slip distribution on the fault plane and the map of rupture velocity map.

5.5.1. Source and fault parameterization

For the selected frequency range [0.05-0.3] Hz, the maximum resolvable wavelength on the fault plane is 5-10 km, leading to a Gaussian width of 4-5 km. We used a regular distribution of Gaussian functions along the strike and along the dip (the total number is: N_g=36). The sample spacing in strike (ξ_1) and in dip (ξ_2) direction is 500m (81 sample along strike and 41 along dip).

An addition condition is required (*Emolo, 2001*):

$$t_{\max} < \tau_r \tag{5.1}$$

in which t_{max} is the maximum propagation time in the subfault and τ_r the rise time. Since the subfault is a triangle, t_{max} is the propagation time along a diagonal:

$$t_{\max} = \frac{\sqrt{d\xi_1^2 + d\xi_2^2}}{\mathbf{v}_r} \tag{5.2}$$

Considering a rupture velocity v_r = 2.0 km/s, and $d\xi_1$ =$d\xi_2$ = 500m, t_{max}=0.35s we can use a rise time τ_r= 1s, around the 10% (*Heaton, 1990*) of the total rupture time.

We used a rectangle slip velocity source time function (eq. 1-12).

For the rupture velocity we used 4x4 control point grid, and we limited the variation range between 1.5 km/s and 3.5 km/s.

The total length of the synthetic data is 81.92s , the frequency step is 0.0122 Hz, and 25 frequencies are used in the inversion.

The accelerograms are band-pass filtered between 0.05 Hz and 0.3 Hz then are integrated to obtained the velocity. The synthetic and real displacements are obtained from the synthetic and the real velocities by integration in the frequency domain (*Cotton et al., 1995*).

5.5.2. The results of inversion: slip map and rupture time map

We computed a total of $25*10^4$ iterations in the inversion. Figure 5-27 shows the smallest misfit per iteration throughout the inversion, demonstrating a relatively slow convergence due to the strong nonlinearity of the problem, for the first 10^4 iterations and then an asymptotic trend around the minimum.

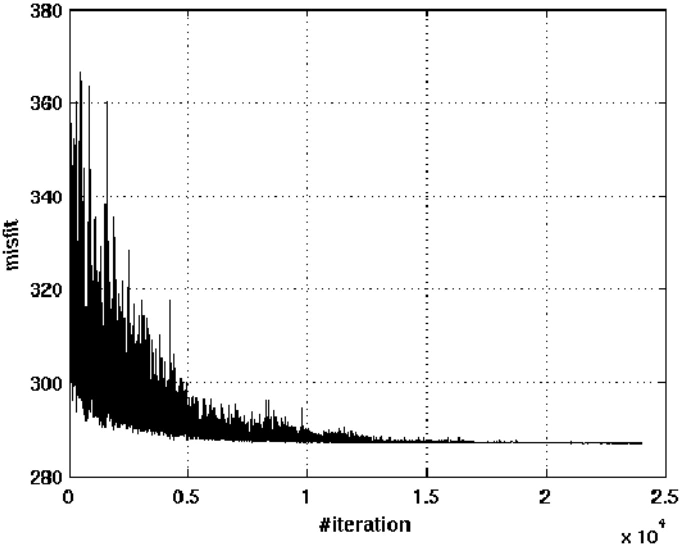

Figure 5-27: Smallest misfit per iteration between synthetics and observations as a function of number of iterations.

The result of inversion, for the best model, is shown in figures 5-24 and 5-26.

The slip distribution on the fault plane (figure 5-28) shows three high slip zones: a major slip patch extends from the hypocenter to the southern sallow part of the fault plane (around 5 km and 10 km with respect to hypocenter); a relatively small slip patch extends in the southern deep part. Finally there is another large slips patch extending in the northern shallow part that gives a contribution to the amplitudes of the stations in the north direction. Moreover the slip map shows a bilateral propagation and high slip zones are located in the shallow part of the fault (around 12 km). The maximum slip value is 6m. The total moment of the best model 2.6 10^{26} dyne·cm, and the moment magnitude M_w 6.9

are in good agreement with other estimates (*Suzuki et al., 2010, Takada et al., 2009*).

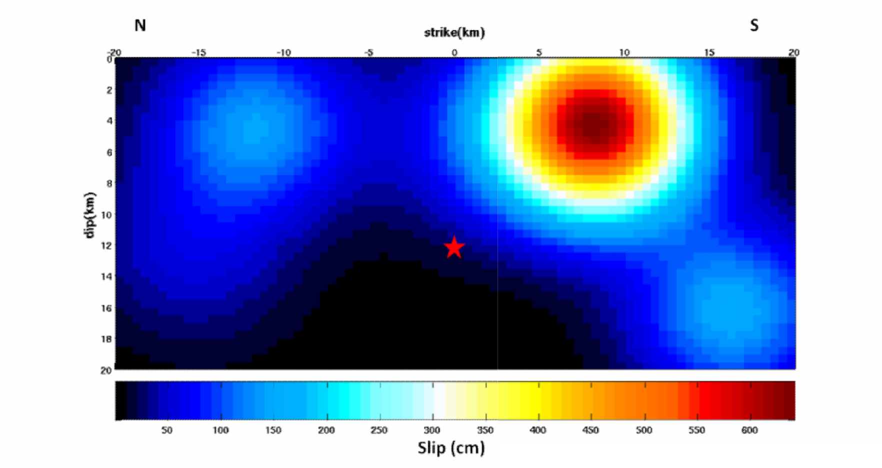

Figure 5-28: Retrieved slip map with two-step procedure inversion. Three high slip zones are present. The red star indicates the hypocenter.

Suzuki .et al. (2010) found one major slip patch extending from 5 to 10 km (figure 5-29), according with our results.

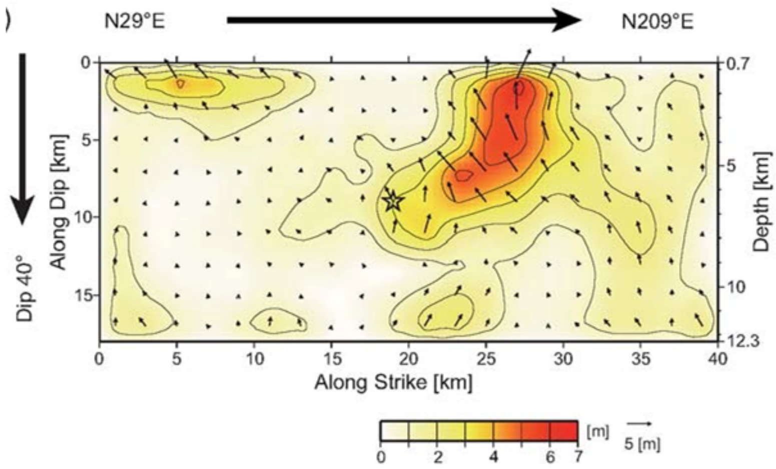

Figure 5-29 : Slip map, as obtained by Suzuki (2010).

Regarding rupture times (figure 5-30), we can observe that rupture accelerates southward but there is a symmetry in up-dip direction. Rupture front reaches the boundary in 10 seconds, whit an estimate average rupture velocity of 1.98 km/s (0.6 v_s), according with Suzuki (2010).

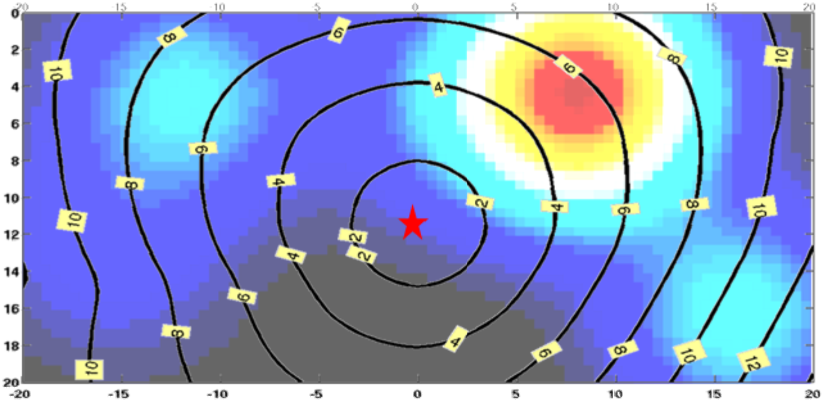

Figure 5-30: Rupture time in correspondence of the slip map.

5.6. The results of inversion: synthetic and real data comparison

A comparison of the observed and synthetic ground velocities (cm/s) is given in figure 5-31, for the all three components N-S (North-South), E-W (East- West) and U-D (Up- Down). Each seismogram, synthetic (red line) and real (blue line), is plot with its amplitude scale.

Generally the fits are very good, for two of the three components. Stations in southward position have a better fit than the stations in north position. In the inversion, we use a L_2 norm that privileges the waveform with large amplitude. The waveforms for the stations in the South, feel the contribution of the largest patch of the slip, so they have larger amplitude than the stations in the North position. For example, the amplitudes range for the station IW012 is [-3, 3]cm/s, while the range for the MYGH02 is [-7, -9]cm/s.

At the station IWTH26, the amplitudes range is even larger ([-13, 15]cm/s), indicating an up-dip directivity effect of the rupture.

In figure 5-31, we show the variance reduction defined as:

$$\mathrm{var} = 1 - \frac{\sum \left[u^{synth} - u^{obs} \right]^2}{\sum \left[u^{obs} \right]^2}$$

Where u^{synth} and u^{obs} are the synthetic and real data, respectively. The variance reduction was performed for each stations and components. The variance reduction is great for the component that has a good fit (in the case of U-D component of IWTH05, E-W component of IWT009), while it is small for the component with bad comparison (in case of U-d component of IWT012).

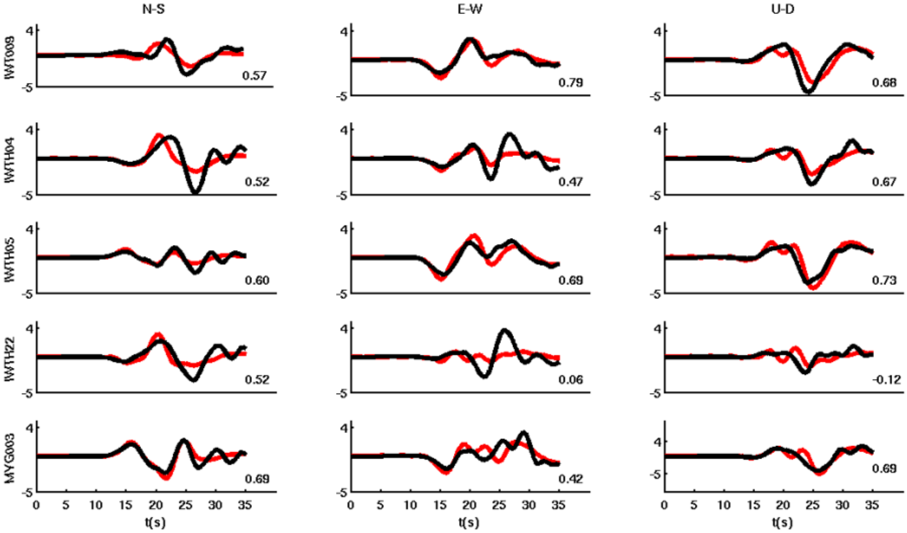

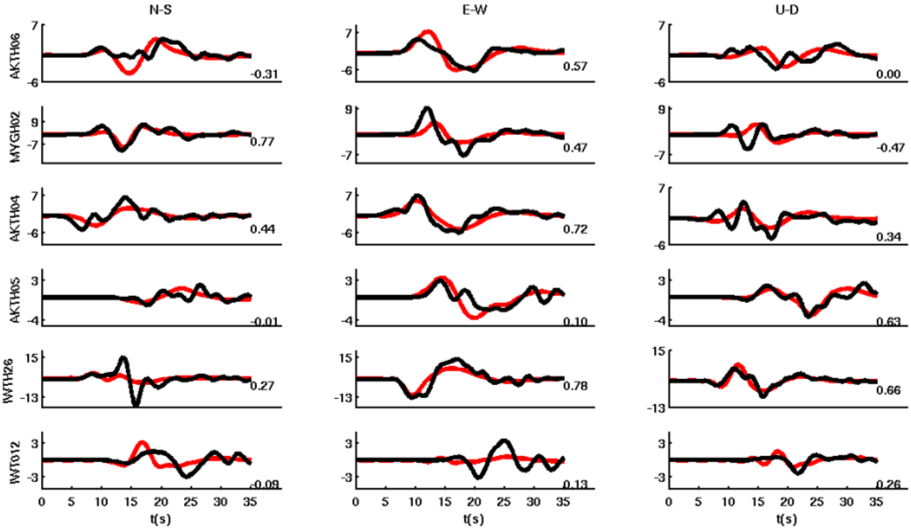

Figure 5-31: Comparison of observed (black) and synthetic (red) data. The seismograms are velocigrams (cm/s). Each pair of data and theoretical seismograms is plotted with its amplitude scale, and with the variance reduction shown to the right of each pair. Station names are indicated on the left.

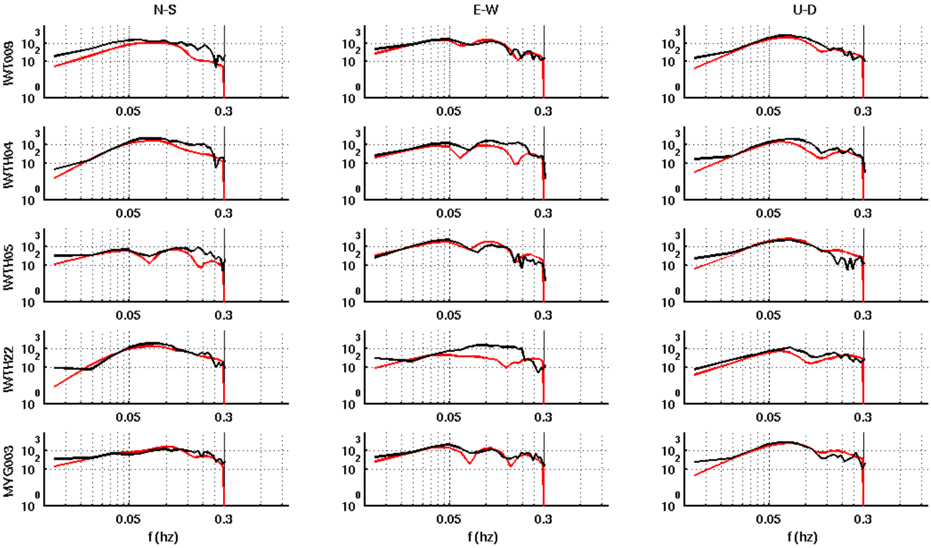

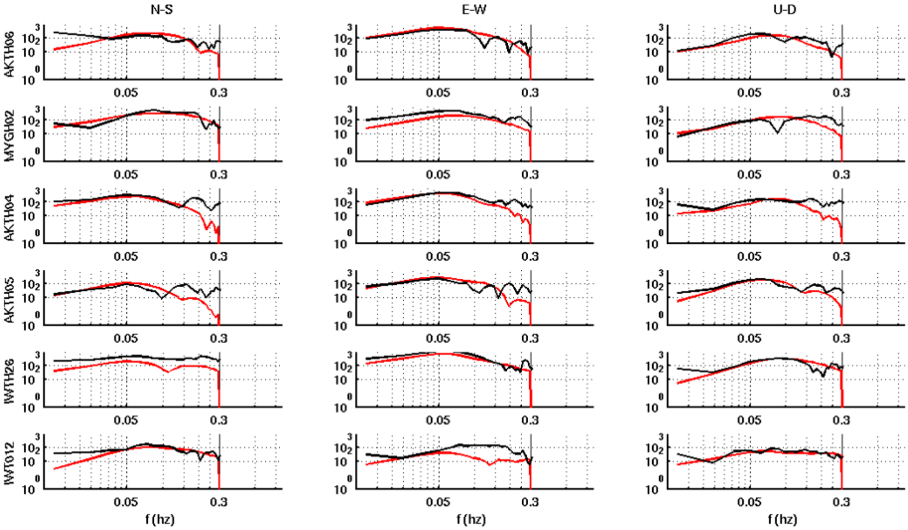

Figure 5-32: Spectra amplitude comparison of the observed (black) and synthetic (red) data. Station names are indicated on the left.

Chapter 6

Quality of solution: Analysis of Error and Resolution

6.1. Introduction

The main drawback of the global methodology, for non linear inversion problem, is the difficulty of assessing error and resolution to the results of the inversion. Actually this problem has not been solved yet, and many authors afforded it in different ways: for example *Emolo and Zollo* (*2005*) estimated the uncertainty on the source parameters through the analysis of the cross-correlation of the misfit function in the neighborhood of the best-fit rupture model; *Peyrat and Olsen* (*2004*) computed the standard deviation from nineteen models with smallest misfit.

In this thesis we sugget a quantitative value for data covariance matrix; our methodology splits the problem in a linear and a non linear part, and we use different approaches for the two problems.

6.2. Data covariance matrix

The goal of inverse theory in Geophysics is to have quantitative information about the Earth from indirect observation of the phenomenon. Since the observations are finite in number and subject to uncertainty, this information is intrinsically probabilistic. This requires the estimation of the uncertainties in the data recorded and in the modelling with the forward theory.

We assume that all uncertainties can be described by multidimensional Gaussian probability densities (*Tarantola*, 1987):

$$p(\mathbf{m}) \propto \exp\left[(G\mathbf{m} - \mathbf{d}_{\mathbf{obs}})^T \sigma_d^{-1} (G\mathbf{m} - \mathbf{d}_{\mathbf{obs}})\right] \qquad (6.1)$$

in which **m** is the vector of parameters, **d** the observed displacement at given set of receivers and g (kernel of inversion) is the non linearity operator that include Green's traction, distribution of Gaussian functions, and the slip velocity source time function. In our case **m** = ($\mathbf{m}_A$, $\mathbf{m}_v$), where $\mathbf{m}_A$ is amplitude of Gaussian functions and $\mathbf{m}_v$ is rupture velocity. Finally, σ_d is data covariance matrix. Our assumption is compatible with the use a L_2 norm in the inversion.

The data covariance matrix σ_d defines the uncertainties, both observed and synthetic data. It is possible to show (*Tarantola, 1987*) that, assuming Gaussian uncertainties, σ_d consists of the sum of the covariance matrix associated with the single uncertainties:

$$\sigma_d = (C_{\mathrm{mod}} + C_{obs}) \qquad (6.2)$$

where C_{obs} (Real data covariance matrix) incorporates the ambient and instrumental noise, and C_{mod} (Synthetic data covariance matrix) is the covariance due to the theoretical error (error in velocity model, discretization error, etc.).

6.2.1. Real data covariance matrix

Uncertainties in real data come from the enviroment and instrumental noise, which makes the observations dirty. It is reasonable to assume that noise contributions on the different data ate uncorrelated. As an example, we considered the seismograms for the station IWTH22. We processed the data in a standard way: we removed the mean value and the trend, we applied a band pass filter, and we integrated the signals twice. Than we applied the standard Discrete Fourier transform. We performed it for the first 14 seconds before the P wave arrival, and for all the duration (figure 6-1). We estimated then the ratio between noise (N) and signal (S), as a function of the frequency.

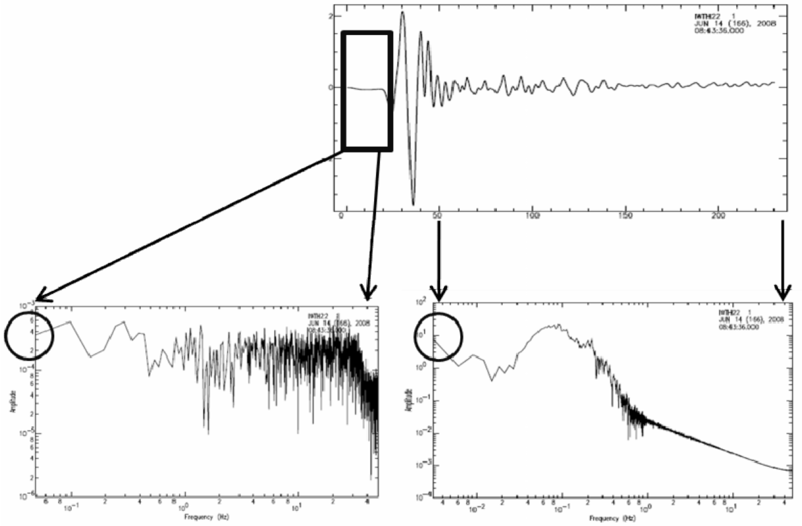

Figure 6-1: Top of figure shows the processed signal for the station IWTH22. In the bottom, we shown the discrete Fourier transform for the noise (left) and complete signal (right).

We founded that in the band of interest (low frequencies), the maximum value is:

$$C_{obs} \to \frac{N}{S} \approx 0.1\% \qquad (6.3)$$

hence the quality of real data is very good, and the noise does not significantly contributes to the uncertainties. We can ignore its contribution so that: $C_{obs} \approx 0$

6.2.2. Synthetic data covariance matrix

We quantify the synthetic data covariance matrix using a measure of the variance reduction between the theoretic, obtained in correspondence of the best model, and recorded seismograms, which are not affected by error ($C_{obs} \approx 0$). The variance reduction (var_red) is computed for all the data (d), for each frequency, and station component.

The variance reduction estimated is:

$$\sigma_d \approx Var\_red = 75\% \qquad (6.4)$$

Finally, we have a estimate of C_{mod}:

$$C_{\mathrm{mod}} \to \frac{\sigma_d}{d} \approx 0.51 \qquad (6.5)$$

6.3. Errors analysis

The covariance of the model parameters (amplitude of Gaussian functions, and rupture velocity) depends on the covariance of the data and the way in which errors are mapped from data to model space. The mapping is a function of the kernel of the inversion (G), and changes depending on the linearity or non-linearity of the problem. In our methodology we split the problem in a linear and a non linear part, so we can use two different approaches for the two problems.

Furthermore, we assumed that the data are uncorrelated, so they have equal variance σ_d^2.

6.3.1. Linear problem

The classic least squares theory suggests that the covariance matrix of the model parameters, is related to the data covariance matrix by (*Menke, 1989*):

$$[\mathrm{cov}\,\mathrm{m}_{\mathrm{A}}] = \sigma_d [G^T G]^{-1} \qquad (6.6)$$

The NNLS algorithm searches the solution only for positive parameters, and if it founds a negative value, this is set to zero. The number of parameters effectively resolved is less than the number of Gaussian functions used in the inversion. In this case, we deleted the column of G, that corresponds to zero value of the amplitude of the Gaussian functions.

6.3.2. Non linear problem

The NA algorithm searches for minimum of the misfit function. This minimum is, generally, very sharp in the vicinity of the estimated solution, and we can approximate the misfit forma to a parabola. Since the curvature of a function is a measure of the sharpness of its minimum, we expect that the variance of the solution is related to the curvature of the misfit function at its minimum, given by the second derivative (*Menke, 1989*):

$$\left[\mathrm{cov}\, m_{\mathrm{v}}\right] = \sigma_d^2 \left[\frac{1}{2} \frac{\partial^2 misfit}{\partial m^2_{\mathrm{v}}} \right]^{-1}_{m_{\mathrm{v}} = m_{\mathrm{v}}^{best}} \qquad (6.7)$$

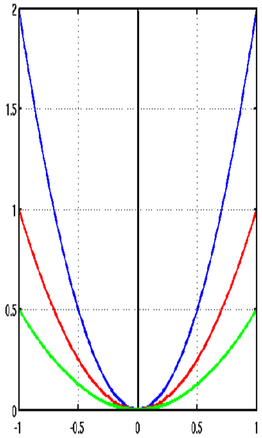

Figure 6-2: An example of different parabola: if the parameter is well resolved, the curvature is small (blue line), while the curvature is large (green line) for a bad resolved parameter.

6.4. Results

In figure 6-3, we represented the relative error σ_A / A, expressed in percentage, associated with three largest slip patches.

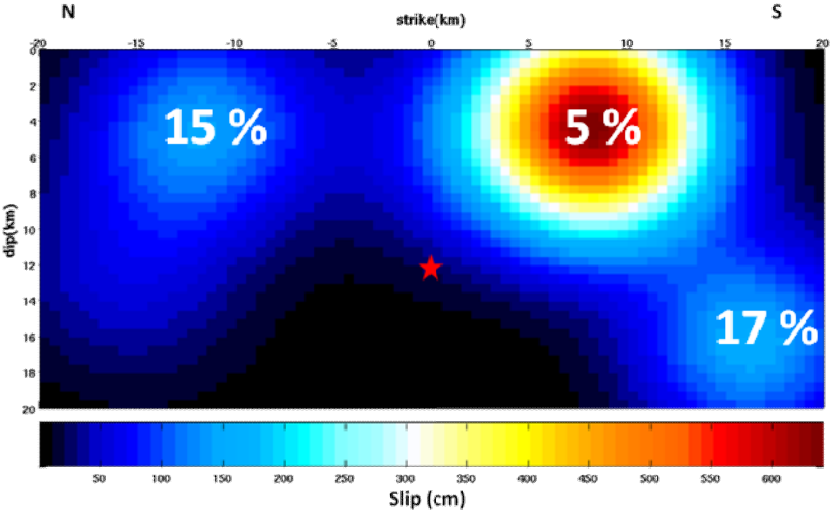

Figure 6-3: Relative error expressed in percentage for the three largest asperities.

As we can see the smallest (5%) relative errors is associated at the main asperity, and the greatest (17%) value at the smaller asperity in the dipped part of the fault. In the other areas of the fault, we do not have a good resolution, and we are not confident of the results.

Now, we consider a rupture velocity and compute equation 6-7 by perturbing the value of the parameter around the best-final value once set the other parameter at their final best value. We focus the attention on two parameters, in control node A (at 8km in strike direction and 4km dip direction) and B (at 14km in strike and 16km in dip direction):

$$\begin{aligned} \sigma_v^{A} &\rightarrow \ 5.77 \ \text{km/s} \\ \sigma_v^{B} &\rightarrow \ 0.13 \ \text{km/s} \end{aligned} \qquad (6.8)$$

The rupture velocities and the associated error are:

$$\begin{aligned} v^{A} &= (3.14 \pm 5.77)\text{km/s} \\ v^{B} &= (1.86 \pm 0.13)\text{km/s} \end{aligned}$$

We are not confident of the error in node A, in fact it is in a part of the fault in which there is not resolution for the slip, while the node B is in a zone of the fault in which there is a largest asperity.

We also computed the marginal probability distribution function (pdf), for this two parameters (rupture velocity in node A and B):

$$pdf(v_r) = \frac{\exp\left[-\frac{misfit^2(v_r)}{2\sigma_d^{\,2}}\right]}{\int \exp\left[-\frac{misfit^2(v_r)}{2\sigma_d^{\,2}}\right] dv_r} \qquad (6.9)$$

and show the result in figure 6-4.

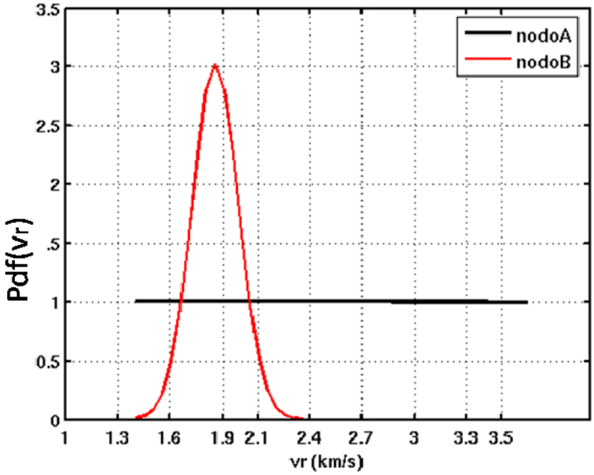

Figure 6-4: The red line is pdf for node B, while the pdf for node A is colored black.

The pdf of node B is picked around the best value, while the pdf of node A is white; this means that all value of rupture velocity are possible for this node.

Conclusion

The aim of this thesis is the definition of a strategy for a robust inversion of strong motion data, starting from a kinematic description of the rupture.

We recalled the fundamental concepts of elastodynamics with the aim of search the relationship between the rupture on a fault plane and the strong motion recorded at the stations on the Earth surface. This relationship is the representation theorem which links the kinematic rupture process on a fault and the propagation terms, called Green's traction. We rewrite the Burridge and Knopoff theorem and obtained a formula, in frequency domain, in which the terms of slip velocity source time function, rupture and Green's tractions are well separated.

One of the main objectives of this thesis is the development and validation of the numerical code STuDenT (*Simulation of daTa with a Delaunay Triangulation*) for computing the representation integral. STuDenT is a numerical code for the simulation of synthetic seismograms, based on the discretization of the fault by a finite element approximation. In particular we adopted a decomposition of the fault plane into triangular subfaults and worked in a reference domain in which all triangles are right. The representation theorem is reduced in a product between triangles areas and the mean value of the function in the three nodes of triangles. This is the kernel for the inversion procedure with the aim of obtaining the final slip and the rupture velocity distribution on the fault plane.

The second goal of this thesis is the study of a new parameterization of the slip, based on 2D overlapping Gaussian functions. Several advantages occur when using such a representation for the slip function. First, the slip map is naturally smooth since it is continuous, many times differentiable and tapered to zero at the boundaries of the fault plane. Moreover, Gaussian functions have an almost flat amplitude spectrum up to a corner wavenumber that is related to the inverse of the Gaussian width; then, the spectrum decays exponentially beyond it. Moreover, this parameterization is expected to relate the slip map to the minimum resolvable wavelength on the fault plane and, through it, to the maximum analyzed frequency in the data. Finally, the positivity constrain is naturally insured by requiring positive coefficients in the Gaussian representation.

In conclusion, we have an efficient tool for the simulate wave propagation inside the Earth and the rules to correlate the frequencies in the data to the characteristic on the fault.

As a final effort of this work, we provided a simple technique for retrieval of the kinematic history on the fault. In particular, we splitted the problem in two steps aimed at separating the computation of the rupture velocity, which is intrinsically a non linear problem, from the evaluation of the slip distribution, a linear problem, when the rupture velocity is fixed. We performed two different synthetic tests in order to validate the procedure. Finally, we applied our procedure to the real case of Mw 6.9 Iwate Nairiku Miyagi Japan earthquake. We inverted eleven three components records, filtered in the band 0.05 - 0.3 Hz. The maximum resolvable wavelength on fault plane is 5-10 km, leading to a Gaussian width of 4-5 km. We used a regular distribution of Gaussian functions along the strike and along the dip (the total number is: N_g=36) and for the rupture velocity we used 4x4 control points grid. The retrieved slip distribution inverted shows three high slip zones: a major slip patch extends from the hypocenter to the southern shallow part of the fault plane, a relatively small slip patch extends in the southern deep part. Finally there is another large slip patch extending in the northern part. Moreover the rupture shows a bilateral propagation and high slip zones are located in the shallow part of the fault The maximum slip value is 6m. The total moment of the best model is 2.6 10^{26} dyne·cm, and the moment magnitude M_w 6.9. Regarding rupture times, the rupture accelerates southward but there is a symmetry in up-dip direction. The average rupture velocity 1.98 km/s (0.6 v_s), according with Suzuki (2010).

In the last chapter we gave a quantitative estimation of errors associates with the parameters. Using our methodology that splits the problem in a linear and a non linear part, we are able to use two different approaches to search for the errors. For the Gaussian amplitudes we use the classical linear theory and we obtained an error of 5% for the amplitude of the largest patch slip, while for the smallest slip patch we founded an error of 17%. As for the values of rupture velocities, we approximated the misfit functon to a parabola. Since the curvature of a function is a measure of the sharpness of its minimum, we have that the variance of the solution is related to the curvature of the misfit function at its minimum. We founded large errors for the control node located in part of the fault in which the slip is very low, while we are confident of the values in the high slip patch.

Appendix A: Time-Frequency misfit criteria

The simple visual comparison of two seismograms, real synthetic data, cannot provide a proper quantification and characterization of difference between the signals, and it is clear that some characteristic of the signal may be more evident and understandable in the time domain, some in the frequency domain. So, the most complete and informative characterization of a signal can be obtained by its decomposition in the time-frequency domain, that is, by its Time-Frequency Representation (TFR).

The misfit criteria (*Kristekova et al.*, 2006) are based on the time-frequency representation of the seismograms obtained as the continuous wavelet transform with the analyzing Morelet wavelet.

The continuous wavelet transform (CWT) of the signal s(t) is defined by

$$CWT_{(a,b)}\{s(t)\}=\frac{1}{\sqrt{a}}\int_{-\infty}^{+\infty}s(t)\psi^*\left(\frac{t-b}{a}\right)dt \qquad (\text{A. }1)$$

where t is time, a is the scale parameter, b is the translational parameter, and Ψ is the analyzing wavelet. The scale parameter a is inversely proportional to the frequency:

$$f = \frac{\omega_0}{2\pi a} \quad (A.2)$$

The Morelet wavelet is given by:

$$\psi(t) = \pi^{-1/4} \exp(i\omega_0 t) \exp\left(-t^2/2\right) \quad (A.3)$$

The TFR of the signal s(t) can be defined as

$$W(t, f) = CWT_{(a,b)}\{s(t)\};\ a = \omega_0/2\pi f,\ b = t \quad (A.4)$$

Let $W_{REF}(t, f)$ be the TFR of the reference signal $S_{REF}(t)$, W(t, f) the TFR of the signal s(t), and N_T and N_F the numbers of the time and frequency samples in the time-frequency (TF), plane respectively.

So we can define the **time-frequency envelope misfit** (TFEM):

$$TFEM(t, f) = \frac{|W(t, f)| - |W_{REF}(t, f)|}{\max_{t,f}\left(|W_{REF}(t, f)|\right)} \quad (A.5)$$

and the **time-frequency phase misfit** (TFPM) as

$$TFPM(t, f) = \frac{|W_{REF}(t, f)|}{\pi} \frac{Arg[W(t, f)] - Arg[W_{REF}(t, f)]}{\max_{t,f}\left(|W_{REF}(t, f)|\right)} \quad (A.6)$$

TFEM (t, f) characterizes the difference between the envelopes of the signals, as a function of the time and frequency. In the same way, the TFPM (t, f) characterizes the difference between the phases of the signals, as a function of the time and frequency. Both differences are normalized with respect to the maximum absolute TFR value of the reference signal.

Bibliography

Aki K. and Richards P.G. (2002). *Quantitative seismology*, second edition, University Science Books Sausalito, California.

Aoi, S., Kunugi T., and Fujiwara H. (2004). *Strong-motion seismograph network operated by NIED: K-NET and KiK-net*, J. Jpn. Assoc. Earthq. Eng. 4, 65-74.

Beroza, G. C. and P. Spudich (1988*). Linearized inversion for fault rupture behavior: Application to the 1984 Morgan Hill, California, earthquake*, J. Geophys. Res., 93,6275-6296.

Boore D.M. and Joyner W.B. (1997). *Site amplifications for generic rock sites*, Bull. Seism. Soc. Am., 87; no. 2; 327-341.

Bouchon M., *A Simple Method to Calculate Green's Function for Elastic Layered Media*, Bull. Seism. Soc. Am. 71, 959-971.

Bouchon, M., N. Toksoz, H. Karabulut, M.P. Bouin, M. Dietrich, M. Akter, M. Edie (2000). *Seismic imaging of the 1999 Izmit (Turkey) rupture inferred from the nearfaultrecordings*, Geophys. Res. Lett., 27, 3013-3016.

Burjanek J. and Zahrdnik J. (2006). *A new kinematic source inversion scheme, First European Conference on Earthquake Engineering and Seismology*, 3-8 September, Geneva, Switzerland, ID 1878.

Burridge R.L. and Knopoff R.L. (1964). *Body force equivalents for seismic dislocations*, Bull. Seism. Soc. Am., 54, 1857-1888.

Cotton F. and Campillo M. (1995). *Frequency domain inversion of strong motion: application to the 1992 Landers earthquake*, J. Geophys. Res. 100, 3961-3975.

Emolo A. (2002), Modelli di frattura dei terremoti crostali di media e forte magnitudo dall'inversione non lineare di registrazioni a corto periodo, Ph. D. Thesis, Univ. Napoli "Federico II".

Emolo A. , Zollo A. (2005). *Kinematic source parameters for the 1989 Loma Prieta earthquake from non-linear inversion accelerograms*, Bull. Seism. Soc. Am., 95(3), 981-994.

Fukuyama E., Irikura K. (1986). *Rupture process of the 1983 Japan Sea (Akita-Oki) earthquake using a waveform inversion method*, Bull. Seism. Soc. Am. 76, 1623-1640.

Fukuyama, E. and T. Mikumo (1993). *Dynamic rupture analysis: Inversion for the source process of the 1990 Izu-Oshima, Japan, earthquake (M 6.5)*, J. Geophys. Res., 98, 6529-6542.

Gallovič F., Brokesova J. (2004). *On strong ground motion with* k^{-2} *slip distribution*, Journal of Seism. 211-221.

Guatteri, M., P. M. Mai, G. C. Beroza, and J. Boatwright (2003). *Strong ground-motion prediction from stochastic-dynamic source models*, Bull. Seism. Soc. Am., 93, 301-313.

Hanks T.C, Kanamori H. (1979). A moment magnitude scale, J. Geophys. Res.

Hartzell S.H., and Heaton T. H. (1983). *Inversion of strong ground motion and teleseismic waveform data for the fault rupture history of the 1979 Imperial Valley, California, earthquake*, Bull. Seism. Soc. Am. 73, 1553-1583.Hartzell and Heaton, 1983.

Hartzell S.H., Gordon G. S., Mendoza C. (1991). *Comparison of L_1 and L_2 norms in a telesismic waveform inversion for the slip history of the Loma Prieta, California, earthquake*, Bull. Seism. Soc. Am. 81, 1518-1536.

Haskell, N. A. (1969). *Elastic displacements in the near-field of a propagating fault*, Bull. Seism. Soc. Am. 59, 865-908.

Heaton, T. H. (1990). *Evidence for and implications of self-healing pulses of slip in earthquake rupture*, Phys. Earth Planet, Int. 64, 1-20.

Hisada Y., (2000). *A theoretical omega-square model considering the spatial variation on slip and rupture velocity*, Bull. Seism. Soc. Am., 90, 387-400.

Hisada Y., (2001). *A theoretical omega-square model considering the spatial variation on slip and rupture velocity. II. Case for a two-dimensional source model*, Bull. Seism. Soc. Am., 91, 651-666.

Jeffreys H., Jeffreys B.S. (1972). *Methods of Mathematical Physics, 3rd ed.*, Cambridge: Cambridge University Press

Kinoshita S. (1998). *Kyoshin net (K-NET)*, Seism. Res. Lett. 69, 309-332.

Komatitsch, D., Vilotte J. P, Vai R., Castillo-Covarrubias J.M. and F.J. Sanchez-Sesma, *The spectral-element method for elastic wave equations: application to 2D and 3D problems*, Int. J. Num. Meth. Eng., 45, 1139-1164, 1998.

Kristekova M., Kristek J., Moczo P., Day S. M., *Misfit Criteria for Quantitative Comparison of seismograms*, Bull. Seism. Society of America, 96, 5, 1836-1850, October 2006.

Lay T., Wallace T. C. (1995). *Modern Global Seismology*. Academic Press.

Lawson C. L. and Hanson, B. J. (1974). *Solving Least Squares Problems*, Prentice-Hall (Englewood Cliffs, NJ).

Lawson C. L. and Hanson R. J. (1995). *Solving Least Square Solution Problems.* Classics in Applied Mathematics SIAM, Philadelphia.

Liu P.C., and Archuleta R. (2004). *A new nonlinear finite fault inversion with 3D Green's functions: Application to 1989 Loma Prieta, California, earthquake*, J. Geophys. Res. 109, B02318.

Monelli D., and Mai P. M. (2008). *Bayesian inference of kinematic earthquake rupture parameters through fitting of strong motion data*, Geophys.J. Int. 173, no. 1, 220–232.

Menke W. (1989). *Geophysical data analysis: discrete inverse theory*, Academic Press, San Diego.

Obara K., Kasahara K., Hori S., and Okada Y. (2005). *A densely distributed high-sensitivity seismograph network in Japan: Hi-net by National Research Institute for Earth Science and Disaster Prevention*, Rev. Sci. Instrum. 76, 021301, doi 10.1063/1.1854197.

Olson A. H. and Apsel R. J. (1982). *Finite faults and inverse theory with application to the 1979 Imperial Valley earthquake*, Bull. Seism. Soc. Am. 72, 1969-2001.

Peyrat S., Olsen K.B. (2004). *Nonlinear dynamic rupture inversion of the 2000 Western Tottori, Japan, earthquake*, Geophys. Res. Lett., 31, L05604

Podvin P. and Lecomte I. (1991). *Finite difference computation of traveltimes in very contrasted velocity model: a massively parallel approach and its associated tool*, Geophys. J. Int. 105,271-274.

Rosakis A.J. (2002). *Intersonic Shear cracks and Fault Ruptures*, Advances in Physics, 51, 1189-1257.

Sambridge M. (1999). *Geophysical inversion with a Neighbourhood algorithm I: searching a parameter space*, Geophys. J. Int. 138, 479-494 .

Sambridge M. (2001). *Geophysical inversion with a Neighbourhood algorithm II: appraising the ensemble*, Geophys. J. Int. 138, 727-746.

Shiomi K., Sekine S. , Takeda T., Asano Y., and Obara K. (2009). *Seismic activity in and around the source region of the 2008 Iwate–Miyagi Nairiku inland earthquake*, Rep. Coord. Comm. Earthq. Predict. 81, 142-144 (in Japanese).

Spudich, P., and Archuleta, R. (1987). *Techniques for earthquake ground motion calculation with applications to source parameterization of finite faults*, in Bolt, B.A. ed., SEISMIC STRONG MOTION SYNTHETICS: Orlando, Florida, Academic Press, 205-265.

Suzuki, S. Aoi, and H. Sekiguchi (2010). *Rupture Process of the 2008 Iwate-Miyagi Nairiku, Japan, Earthquake Derived from Near-Source Strong-Motion Records*, Bull. Seism. Soc. of Am., 100(1): 256 - 266.

Takeo, M. (1987).*An inversion method to analyze the rupture process of earthquakes using near-field seismograms*, Bull. Seism. Soc. Am., 77, 490-513.

Tarantola A., *Inverse problem Theory*, Elsevier, New York, 1987

Trifunac M.D. (1974). *A three-dimensional dislocation model for San Fernando, California, earthquake of February 9, 1971*, Bull. Seism. Soc. Am. 64, 149-172.

Tromp J., Tape C., and Liu Q. (2005). *Seismic tomography, adjoint methods, time reversal and banana-doughnut kernels*, Geoph J. Int., 160, 196-216.

Vallée and Bouchon (2004). *Imaging coseismic rupture in far field slip patches*, Geophys. J. Int. 156, 615-630.

Yagi, Y. and M. Kikuchi (2000). *Source rupture process of the Kocaeli, Turkey, earthquake of August 17, 1999, obtained by joint inversion of near-field data and teleseismic data*, Geophys. Res. Lett., 27, 1969-1972.

Yoshida, S. and K. Koketsu (1990). *Simultaneous inversion of waveform and geodetic data for the rupture process of the 1984 Naganoken-Seibu, Japan, earthquake*, Geophys.J. Int., *103, 355-362.*

Wald, D. J. and T. H. Heaton (1994). *Spatial and temporal distribution of slip for the 1992 Landers, California, earthquake*, Bull. Seism. Soc. Am., 84, 668-691.

Waldhauser F. and Ellsworth W. L. (2000). *A double-difference earthquake location algorithm: Method and application to the Northern Hayward fault*, Bull. Seism. Soc. Am. 90, 1353-1368.

Index

A

Aki 28; 150
Anti-directivity direction 36
Aoi 103; 150
Apsel 72; 93; 154
Archuleta 35

B

Boore 46; 150
Bouchon 16; 44; 75; 150; 156
Brokesova 82; 151
Burridge 16; 27; 151

C

Compsyn 46
Conjugate gradient techniques 83
Continuous wavelet transform 147
Cotton 29; 126; 151
Courant number 35
Coutant 16; 44
CWT 147

D

Data covariance matrix 134
Delaunay triangulation 34
Density 20
Dip angle (δ), of a fault 42
Directivity direction 36
Directivity effect 36
Discrete Wavenumber / Finite Element 46
Discrete wave-number integration technique 44
Doppler effect 36

E

Eikonal equation 45
Ellsworth 156
Emolo 125; 151
Empirical Green's function 27
Exponential distribution 94

F

Fault, surface 28
Fourier transform 28
Fukuyama 27; 29; 151

G

Gallovič 82; 151
Gaussian configuration 87
Genetic algorithm 100
Global CMT 102
Green's tractions 28
Guatteri 29; 151

H

Hanks 48; 152
Hartzell 72; 94; 152
Heaton 72; 98; 152

Hisada 29; 152

I

Inverse-fault 102

J

Jeffreys 21; 153
Joyner 46; 150

K

Kik-net 103
Kinematic source model 25
Kinoshita 103; 153
K-net 103
Knopoff 16; 27; 151
Komatitsch 36; 153
Kristekova 53; 147; 153
Kronecker delta function 21
k-square model 82
Kukuyama 29

L

L_1 norm 94
L_2 norm 94
Lamé constants 21
Lawson 98; 153
Lay 37; 153
Lecomte 45
Lisheng 46
Liu 35

M

M_0 48
Marginal probability distribution function 141
Maximum propagation time 125
Menke 94; 138; 154
Moment Magnitude 48
Montecarlo technique 100
Morelet wavelet 148
M_W 48

N

NA 99
Neighbourhood algorithm . 99
NNLS 98
Non-negative least square solution 98
Normal strain 21
Number of gaussian configuration, Mod 87
Nyquist frequency 36

O

Obara 102; 154
Olson 72; 93; 103; 154
Overlapping Gaussian functions 73
Overlapping paramter 76

P

Parseval, theorem 95
Peyrat 133; 154
Podvin 45; 154
Positivity constrain 84
Press 83

Q

Q_P 47
Q_S 47

R

Rake angle (λ), of a fault 42

Real data covariance matrix 134
Representation integral 27; 33
Richards 28; 150
Rise time 25
Rosakis 29; 154
Rupture time 29
Rupture velocity 29

S

Sambridge 99; 154; 155
Second law of dynamic 20
Seismic Moment 48
Shape functions 38
Shear modulus 48
Shear strain 21
Shiomi 102; 155
Simulated annealing 100
Sinc function 30
Slip velocity source time function 29
Spudich 33; 46; 155
Strain tensor 21
Stress tensor 20
Strike angle (Φ), of a fault .. 42
STuDenT 41
Suzuki 128; 155
svSTF 29
svSTFb 30
svSTFt 30
Synthetic data covariance matrix 135

T

Tarantola 134; 155
TF 148
TFEM 148
TFPM 148
TFR 147
Thrust fault 102
Time-frequency envelope misfit 148
Time-frequency phase misfit 148
Time-frequency representation 147
Traction 23
Trifunac 93; 155
Tromp 83; 156

V

Vallée 75; 156
Vector of parameters 134
Voronoi cell 99

W

Waldhauser 103; 156

Index of figures

FIGURE 1-1: SCHEME OF THE SEISMIC WAVE PROPAGATION AND RECORD AT THE SEISMOMETERS. THE TRIANGLES REPRESENT SEISMIC STATIONS, WHICH RECORD THE GROUND MOTION GENERATED BY AN EXTENDED FAULT (YELLOW RECTANGLE). ________ 19
FIGURE 1-2: SKETCH OF THE ELASTIC DISPLACEMENT CORRESPONDING TO A BODY FORCE F, AND TRACTION T IN A MEDIUM WITH GREEN'S FUNCTION G. ________ 23
FIGURE 1-3: AN ELASTIC BODY WITH VOLUME V AND EXTERNAL SURFACE S. THE FAULT PLANE HAS TWO SIDE, LABELED WITH Σ+ AND Σ-, AND N IS THE NORMAL TO THE FAULT FROM Σ+ TO Σ-. ________ 24
FIGURE 1-4: SYSTEM COORDINATE ON FAULT SURFACE. ________ 26
FIGURE 1-5: MODEL GEOMETRY AND PARAMETERS. ________ 28
FIGURE 2-1: DELAUNAY TRIANGULATION OF THE HYPOTHETICAL FAULT PLANE. ________ 34
FIGURE 2-2: .EXAMPLE OF THE TRANSFORMATION FROM THE PHYSICAL DOMAIN (LEFT) TO THE REFEREE (RIGHT) DOMAIN, IN WHICH ALL TRIANGLES ARE RIGHT. ________ 39
FIGURE 2-3: FLOWCHART OF STUDENT CODE. ________ 41
FIGURE 2-4: DEFINITION OF CONVENTIONAL PARAMETERS USED TO INDICATE FAULT ORIENTATION AND SLIP DIRECTION. ________ 42
FIGURE 2-5: VELOCITY-DENSITY MODEL FOR EXTENDED-FAULT FORWARD-MODELING SIMULATION. ________ 47
FIGURE 2-6: 3D-VIEW OF THE RUPTURE PLANE WITH AN INHOMOGENEOUS SLIP DISTRIBUTION, COLORED-CODED ACCORDING TO THE AMOUNT OF THE SLIP (IN M). THE BLACK STAR DENOTES THE HYPOCENTER. ________ 49
FIGURE 2-7: SOURCE-RECEIVER GEOMETRY FOR A STRIKE-SLIP FAULT CASE. THE RED STAR SHOWS THE EPICENTER AT X=0, Y=0 IN A RIGHT-HANDED COORDINATES SYSTEM WITH POSITIVE X POINTING EAST, POSITIVE Y POINTING NORTH.

The red line indicates the vertical projection of the updip-edge of an extend fault plane at depth. _____ 50

Figure 2-8: Comparison between STuDenT and Compsyn for all ten station, and for the three component (N-S: North-South; E-W: East-West; U-D: Up-Down). The seismograms generated by STuDenT are in red, while the seismograms generated by Compsyn are in black. Each pair of theoretical seismograms is plotted with its amplitude scale (m/s). _____ 51

Figure 2-9: Comparison, in frequency domain, between STuDenT (red) and Compsyn (black) for all ten stations, and for the three component (N-S: North-South; E-W: East-West; U-D: Up-Down). _____ 52

Figure 2-10: Analysis for station 01. (Top) Comparison between STuDenT (red) and Compsyn (black) synthetic seismograms (Middle) Time-frequency envelope misfit TFEM(t, f) and (Bottom) time-frequency phase misfit TFPM(t, f) plots. Columns show E-W (right), N-S (center), U-D components (left), respectively. Red color in the TFEM and the TFPM images indicates a greater amplitude and a positive phase shift in the STuDenT seismograms with respect to Compsyn seismograms. Blue color represents the opposite case. _____ 55

Figure 2-11: Analysis for station 04. (Top) Comparison between STuDenT (red) and Compsyn (black) synthetic seismograms (Middle) Time-frequency envelope misfit TFEM(t, f) and (Bottom) time-frequency phase misfit TFPM(t, f) plots. The color scale have the same interpretation of figure 2-10. _ 56

Figure 2-12: Analysis for station 10. (Top) Comparison between STuDenT (red) and Compsyn (black) synthetic seismograms (Middle) Time-frequency envelope misfit TFEM(t, f) and (Bottom) time-frequency phase misfit TFPM(t, f) plots. For the color scale interpretation see the figure 2-10. _____ 57

Figure 2-13: 3D-view of the rupture plane with an inhomogeneous slip distribution, colored-coded according to the amount of the slip (in m). The black star denotes the hypocenter. ____ 59

Figure 2-14: Source-receiver geometry. for a dip-slip fault case. The red star shows the epicenter at X=0, Y=0 in a right-handed coordinates system with positive X pointing East, positive Y pointing North. The red line indicates the vertical projection of the updip-edge of an extend fault plane at depth. ____ 59

Figure 2-15: Comparison between STuDenT and Compsyn for all 20 stations, and for the three component (N-S: North-South; E-W: East-West; U-D: Up-Down). The seismograms generated by STuDenT are in red, while the seismograms generated by Compsyn are in black. Each pair theoretical seismograms are plotted with its amplitude scale (m/s). ____ 62

Figure 2-16: Comparison, in frequency domain, between STuDenT (red) and Compsyn (black) for all 20 stations, and for the three component (N-S: North-South; E-W: East-West; U-D: Up-Down). ____ 64

Figure 2-17: Analysis for the station 01. (Top) Comparison between STuDenT (red) and Compsyn (black) synthetic seismograms (Middle) Time-frequency envelope misfit TFEM(t, f) and (Bottom) time-frequency phase misfit TFPM(t, f) plots. Columns show E-W (right), N-S (center), U-D components (left), respectively. Red color in the TFEM and the TFPM images indicates a greater amplitude and a positive phase shift in the STuDenT seismograms with respect to Compsyn seismograms. Blue color represents the opposite case. ____ 66

Figure 2-18: Analysis for the station 10. (Top) Comparison between STuDenT (red) and Compsyn (black) synthetic seismograms (Middle) Time-frequency envelope misfit TFEM(t, f) and (Bottom) time-frequency phase misfit TFPM(t, f) plots. Columns show E-W (right), N-S (center), U-D components (left), respectively. 67

Figure 2-19: Analysis for the station 14. (Top) Comparison between STuDenT (red) and Compsyn (black) synthetic seismograms (Middle) Time-frequency envelope misfit TFEM(t, f) and (Bottom) time-frequency phase misfit TFPM(t, f) plots- Columns show E-W (right), N-S (center), U-D components (left), respectively. 68

Figure 2-20: Analysis for station the 18. (Top) Comparison between STuDenT (red) and Compsyn (black) synthetic seismograms (Middle) Time-frequency envelope misfit TFEM(t, f) and (Bottom) time-frequency phase misfit TFPM(t, f) plots- Columns show E-W (right), N-S (center), U-D components (left), respectively. Red color in the TFEM and the TFPM images indicates a greater amplitude and a positive phase shift in the STuDenT seismograms with respect to Compsyn seismograms. Blue color represents the opposite case. 69

Figure 3-1: An example of overlapping 2D Gaussian function. 74

Figure 3-2: Addition of two overlapping Gaussian functions in one dimension. In the top panels we plot two overlapping functions (dashed lines) and their sum (solid line). The ratio between the peak amplitudes is two. In the left figure, the overlapping is large and the sum is still peaked, with a width larger than the width of the initial Gaussian functions. On the right, instead, the overlapping is small and the sum shows two isolated peaks. In the bottom panels, we represent the square amplitude of the Fourier spectra of the sum function, plotted in the above panels. When the overlapping is large the spectrum decays as a standard Gaussian filter, with a

CUTOFF WAVENUMBER COMPARABLE WITH 1/Σ. IN THE RIGHT PANEL, THE INFLUENCE OF THE DISTANT GAUSSIAN FUNCTIONS RESULTS IN AN OSCILLATING SPECTRUM, FOR WAVENUMBERS SMALLER THAN Σ. 78

FIGURE 3-3: EXAMPLE OF 2D GAUSSIAN FUNCTION. 80

FIGURE 3-4: FOUR 2D GAUSSIAN FUNCTION, HAVING THE SAME Σ AND THE SAME DISTANCE BETWEEN CENTERS. 81

FIGURE 3-5: THE FIGURE (A) REPRESENTS THE 'OBSERVED' (A) MAP WHILE THE FIGURE B REPRESENTS THE MAP OBTAINED BY THE INVERSION WHIT THE METHODOLOGY DISCUSSED IN THE PARAGRAPH 3.3.1. 86

FIGURE 3-6: REFERENCE MAP BASED ON K-SQUARE MODEL FOR A FAULT 35X15 KM^2, ALONG STRIKE AND DIP RESPECTIVELY. 88

FIGURE 3-7: THE FIGURE SHOWS THE RESULTS OF INVERSION FOR 15 DIFFERENT CONFIGURATIONS OF THE GAUSSIAN PARAMETERIZATION (MOD-01 TO MOD-15). THE CONFIGURATIONS DIFFER FROM EACH OTHER FOR THE GAUSSIAN NUMBER THAT INCREASES MOVING FROM THE MOD-01 TO THE MOD-15. THE FIT IS BETTER FOR THE CONFIGURATIONS WITH LARGER NUMBER OF GAUSSIAN FUNCTIONS. 88

FIGURE 3-8: SPECTRA OF K-SQUARE MODEL ARE SHOWN IN BLUE, WHILE THE SPECTRA OF THE GAUSSIAN CONFIGURATION ARE SHOWN IN RED. 89

FIGURE 3-9: RELATIONSHIP BETWEEN Σ AND THE MINIMUM RESOLVABLE WAVELENGTH, IN THREE CASE: Σ (RED-LINE), Σ/2 (GREEN-LINE), Σ/4 (BLUE-LINE). 91

FIGURE 3-10: FLOWCHART OF THE RELATIONSHIP BETWEEN THE MAXIMUM SIGNAL FREQUENCY AND THE CONFIGURATION OF THE GAUSSIAN FUNCTIONS ON THE FAULT PLANE. 91

FIGURE 4-1: FLOWCHART OF THE TWO-STEPS PROCEDURE TO INVERSION. 97

FIGURE 4-2: THE FIGURE SHOWS THE RESULT FOR TWO PARAMETERS PROBLEM. THE UPPER-LEFT PANEL SHOWS 10 SAMPLES AND THE CORRESPONDS VORONOI CELLS; THE UPPER-RIGHT PANEL SHOWS 100 SAMPLES. THE LOWER-LEFT PANEL

SIMILAR TO UPPER-RIGHT PANEL BUT WITH 10000 SAMPLES. HERE THE ALGORITHM CONCENTRATES ON FOUR DISTINCT REGION CORRESPONDING TO THE MINIMUM OF THE MISFIT. THE LOWER-RIGHT PANEL SHOWS THE CONTOURS OF THE MISFIT FUNCTION IN GREY SCALE. 100
FIGURE 5-1: FAULT-PLANE GEOMETRY AND FOCAL MECHANISM. 102
FIGURE 5-2: DISTRIBUTION OF THE STRONG MOTION STATIONS (TRIANGLES) AND FAULT PLANE MODEL (RECTANGLE) USED FOR THE INVERSION. THE RED STAR INDICATES THE EPICENTER. THE MOMENT TENSOR SOLUTION IS SHOWN AT UPPER-LEFT OF THE FIGURE. 103
FIGURE 5-3: SLIP DISTRIBUTION WITH ONE PATCH USED FOR THE SYNTHETIC SEISMOGRAMS GENERATION. 105
FIGURE 5-4: SLIP MAPS INVERTED IN THE NO NOISE CASE. 106
FIGURE 5-5: SLIP MAP INVERTED WITH "REAL" DATA CONTAMINATED WITH 10 % OF NOISE. 106
FIGURE 5-6: SLIP MAP INVERTED WITH "REAL" DATA CONTAMINATED WITH 30 % OF NOISE. 106
FIGURE 5-7: COMPARISON BETWEEN “REAL” WITH NO NOISE (BLACK) AND SYNTHETIC (RED) DATA. 107
FIGURE 5-8: COMPARISON BETWEEN “REAL” WITH 10 % NOISE (BLACK) AND SYNTHETIC (RED) DATA. 108
FIGURE 5-9: COMPARISON BETWEEN “REAL” WITH 30 % NOISE (BLACK) AND SYNTHETIC (RED) DATA. 109
FIGURE 5-10: SPECTROGRAM FOR THE STATION MYGH02, WHIT NO –NOISE “REAL” DATA. RED COLOR IN THE TFEM AND THE TFPM IMAGES INDICATES A GREATER AMPLITUDE AND A POSITIVE PHASE SHIFT. BLUE COLOR REPRESENTS THE OPPOSITE CASE. 111
FIGURE 5-11: SPECTROGRAM FOR THE STATION MYGH02, WHIT 10% OF NOISE. 112
FIGURE 5-12: SPECTROGRAM FOR THE STATION MYGH02, WHIT 30% OF NOISE. 112
FIGURE 5-13: SLIP DISTRIBUTION WITH THREE PATCH USE FOR THE SYNTHETIC SEISMOGRAMS GENERATION. 113
FIGURE 5-14: SLIP MAP INVERTED IN THE NO NOISE CASE. 114

Figure 5-15: Slip map inverted with "real" data contaminated with 10 % of noise. 114

Figure 5-16: Slip map inverted with "real" data contaminated with 30 % of noise. 114

Figure 5-17: Comparison between “real” with no noise (black) and synthetic (red) data. 115

Figure 5-18: Comparison between “real” with 10 % noise (black) and synthetic (red) data. 116

Figure 5-19: Comparison between “real” with 30 % noise (black) and synthetic (red) data. 117

Figure 5-20: TFEM and the TFPM for the station MYGH02, in the no-noise real “data”. 118

Figure 5-21: TFEM and the TFPM for the station MYGH02, with 10% of noise in the “real” data. 119

Figure 5-22: TFEM and the TFPM for the station MYGH02, with 30% of noise in the “real” data. 119

Figure 5-23: Slip and rupture time map. 120

Figure 5-24: Comparison between “real” (black) and synthetic (red) data. 122

Figure 5-25: TFEM and the TFPM for the station MYGH02. Red color in the TFEM and the TFPM images indicates a greater amplitude and a positive phase shift in the “inverted” seismograms with respect to “real” seismograms. Blue color represents the opposite case. 123

Figure 5-26: Slip and rupture time: results of the inversion. 123

Figure 5-27: Smallest misfit per iteration between synthetics and observations as a function of number of iterations. 127

Figure 5-28: Retrieved slip map with two-step procedure inversion. Three high slip zones are present. The red star indicates the hypocenter. 128

Figure 5-29 : Slip map, as obtained by Suzuki (2010). 129

Figure 5-30: Rupture time in correspondence of the slip map. 129

FIGURE 5-31: COMPARISON OF OBSERVED (BLACK) AND SYNTHETIC (RED) DATA. THE SEISMOGRAMS ARE VELOCIGRAMS (CM/S). EACH PAIR OF DATA AND THEORETICAL SEISMOGRAMS IS PLOTTED WITH ITS AMPLITUDE SCALE, AND WITH THE VARIANCE REDUCTION24F SHOWN TO THE RIGHT OF EACH PAIR. STATION NAMES ARE INDICATED ON THE LEFT. ____ 132

FIGURE 5-32: SPECTRA AMPLITUDE COMPARISON OF THE OBSERVED (BLACK) AND SYNTHETIC (RED) DATA. STATION NAMES ARE INDICATED ON THE LEFT. ____ 133

FIGURE 6-1: TOP OF FIGURE SHOWS THE PROCESSED SIGNAL FOR THE STATION IWTH22. IN THE BOTTOM, WE SHOWN THE DISCRETE FOURIER TRANSFORM FOR THE NOISE (LEFT) AND COMPLETE SIGNAL (RIGHT). ____ 136

FIGURE 6-2: AN EXAMPLE OF DIFFERENT PARABOLA: IF THE PARAMETER IS WELL RESOLVED, THE CURVATURE IS SMALL (BLUE LINE), WHILE THE CURVATURE IS LARGE (GREEN LINE) FOR A BAD RESOLVED PARAMETER. ____ 139

FIGURE 6-3: RELATIVE ERROR EXPRESSED IN PERCENTAGE FOR THE THREE LARGEST ASPERITIES. ____ 140

FIGURE 6-4: THE RED LINE IS PDF FOR NODE B, WHILE THE PDF FOR NODE A IS COLORED BLACK. ____ 142

Index of the tables

TABLE 5-1: NAMES, COORDINATED (LATITUDE AND LONGITUDE), AND DISTANCE FROM EPICENTER OF THE STATIONS USED IN INVERSION. 103
TABLE 5-2: 1D VELOCITY STRUCTURE MODEL USED TO CALCULATE GREEN'S FUNCTION. D IS THE DEPTH OF THE UPPER INTERFACE, α AND β ARE P AND S VELOCITIES OF WAVE RESPECTIVELY AND ρ IS DENSITY OF THE MEDIUM. 104
TABLE 5-3: SUMMARY OF THE RESULTS OF THE INVERSION – CASE A. 110
TABLE 5-4: SUMMARY OF THE RESULTS OF THE INVERSION - CASE B. 118

Symbols

Symbols	**Name**	**Units**
α	P-wave velocity	km/s
β	S-wave velocity	km/s
c_{ijkl}	Moduli tensor of elastic deformation	
C_{mod}	Synthetic data covariance matrix	
C_{obs}	Real data covariance matrix	
CWT	Continuous wavelet transform	
δ_{ij}	Kronecker delta function	
δ	Dip angle	°
$\Delta\delta$	Sample spacing along dip direction	km
$\Delta\Phi$	Sample spacing along dip direction	km
f_{max}	Resolving frequency of the finite element grid	s^1
f_N	Nyquist frequency	s^{-1}
k	Wavenumber	Km^{-1}

L	Length of fault plane	Km
λ	Lamè constant	
λ	Rake angle	°
λ_{min}	Minimum wavelength resolvable on the fault plane	Km
μ	Lamè constant	
$\mathbf{m}$	Vector of parameters	
$\mathbf{m}_A$	Vector of Gaussian amplitude parameters	cm
$\mathbf{m}_V$	Vector of rupture velocity parameters	km/s
M_0	Seismic moment	N·m or dyne·cm
Mod	Number of Gaussian functions configuration	
M_w	Moment magnitude	
M_{JMA}	Magnitude of Japan Meteorological Agency	
N	Noise	
Na	Neighbourhood Algorithm	
N_g	Number of Gaussian functions in the configuration	
N_g^{δ}	Number of Gaussian	

	functions along dip direction	
N_g^{Φ}	Number of Gaussian functions along strike direction	
n_r	Number of cells in which a new samples is searched	
N_t	Number of samples in time domain	
N_ω	Number of samples in frequency domain	
n_s	Sample space at each iteration	
NNE	North-northeast direction	
Φ	Strike angle	°
pdf	Probability distribution function	
P-wave	Primary wave	
Q_P	P-wave quality factor	
Q_S	S-wave quality factor	
R_T	Rupture time	s
ρ	Density	g/cm^3
S	Signal	
S-wave	Secondary wave	
SSE	South-southwest direction	

svSTF	Slip velocity source time function	
svSTFr	STF for a rectangle function	
svSTFt	STF for a triangle function	
σ_d	Data covariance matrix	
Σ	Surface of fault plane	km^2
TFEM	Time-frequency envelope misfit	
TFPM	Time-frequency phase misfit	
TFR	Time-frequency representation	
t_{max}	Maximum propagation time in a triangle	s
τ_r	Rise time	s
u^{synth}	Synthetic data	km/s
u^{obs}	Real data	km/s
v_R	Rupture velocity	km/s
W	Width of fault plane	km
χ	Overlapping parameter	
ω	Angular frequency	s^{-1}

Page intentionally blank.